

ABSTRACT

PIERCE, CHANDLER AUSTIN. Investigating Tectonic and Oceanographic Influences on Sediment Deposition throughout the Northern Andaman Sea (Under the direction of Dr. Paul Liu).

Annually, large Southeast Asian rivers deliver four billion tons of sediment to the oceans from the Tibetan Plateau, accounting for approximately 30% of global riverine sediment discharge. Of these sediments, an estimated 600 million tons travels through the Ayeyarwady (Irrawaddy), Thanlwin (Salween), and Sittaung (Sittang) Rivers. Considered to be the last remaining free-flowing, large rivers in Asia outside of the Arctic, this trio of rivers discharges directly into the active back-arc basin that is the Northern Andaman Sea. Limited oceanographic surveys in the past have indicated that circulation patterns and alternating monsoonal systems drive riverine sediment offshore, across the Martaban Canyon. However, specific questions surrounding the processes that influence sediment deposition in the Northern Andaman Sea remain unresolved. Therefore, in December of 2017, a two-week research cruise was conducted to investigate better the fate and flux of sediment discharged by the Ayeyarwady River and its significant tributaries. A combination of CHIRP high-resolution seismic data, Kasten and Box cores, and Interferometric Synthetic Aperture Radar (InSAR) were collected and processed post-cruise in support of these efforts.

The CHIRP high-resolution seismic data were processed using EdgeTech Discover software and analyzed to determine the historical evolution of the subaqueous delta by applying basic sequence stratigraphy principles. Collaborators processed the sediment cores at the Virginia Institute of Marine Science (VIMS), and ^{210}Pb and ^{137}Cs were measured to derive the Holocene sediment accumulation rate per location. The InSAR data were collected over the January 2016 –2020-time frame and displayed vertical deformation of the sub-aerial delta, thereby providing insight into how the delta is responding to active tectonism.

The findings suggest: 1) A compound clinoform prograding rapidly into a distal depocenter in the Martaban Depression. 2) The presence of a highly reflective transgressive surface, representing the boundary between Holocene and relict sediment. 3) A 10-m-thick shore-attached clinoform that is separated into two stacked, fore-stepping sigmoids, representing the early and late highstand system tract. 4) Seasonal variations in tidal amplitude allow nearshore sediment to escape to the foresets, where energy sustaining the turbid water area diminishes, resulting in a zone of rapid sediment accumulation as foreset beds. 5) High-resolution seismic imagery collected by the CHIRP towfish reveals distinctive bookshelf faulting in the Martaban Depression, indicative of extensional tectonics within the back-arc basin. 6) Shoreline stasis over the last two centuries has resulted in cannibalization of the major distributary mouths. A time-series analysis of InSAR data suggests that the delta is shifting eastwards, into the Gulf of Martaban. Along the delta's eastern shoreline, near the Bogale Promontory, uplift/aggradation is occurring at a rate of about 1.5 cm a^{-1} .

© Copyright 2020 by Austin Pierce

All Rights Reserved

Investigating Tectonic and Oceanographic Influences on Sediment Deposition throughout the
Northern Andaman Sea

by
Austin Chandler Pierce

A thesis submitted to the Graduate Faculty of
North Carolina State University
in partial fulfillment of the
requirements for the degree of
Master of Science

Marine, Earth, and Atmospheric Sciences

Raleigh, North Carolina
2020

APPROVED BY:

Dr. Paul Liu
Committee Chair

Dr. Karl Wegmann

Dr. Helena Mitsova

Dr. Elana Leithold

DEDICATION

I dedicate this thesis to my wonderful wife, Leslie Pierce, and the constant support she has provided me throughout this venture. I also would like to mention my parents, Joel and Sheryl Pierce, for instilling in me the resilience and perseverance necessary to weather the demanding trials I have experienced in graduate school.

BIOGRAPHY

Austin C. Pierce was born in Charlotte, North Carolina, on February 10, 1991. The author obtained his Bachelor of Sciences in Geology from North Carolina State University in 2017. In December 2017, he attended a two-week research cruise in the Northern Andaman Sea before he began his Masters of Sciences degree. In the spring of 2018, he began his coursework towards a Masters of Sciences at North Carolina State University while working as a research assistant in the Sea Level Change and Ocean Margin Evolution Lab, under the direction of Dr. Paul Liu. During this time, he attended and presented at several international conferences including: ICAMG 9 in Shanghai, China, the International Marine Sciences conference in Yangon, Myanmar, AGU and Ocean Science Meeting.

ACKNOWLEDGMENTS

The author is grateful to Professor J. Paul Liu for his dedication and guidance relating to this work and the multitude of opportunities he provided. He thanks Drs. Karl Wegmann, Elana Leithold, and Helena Mitsova for their constructive reviews. The author would also like to thank Drs. Steve Kuehl and Courtney Harris of Virginia Institute of Marine Science, Dr. Day Wa Aung of University of Yangon, and Dr. Yin Yin Aye of Mawlamyine University for their help and expertise on the source material throughout this process.

TABLE OF CONTENTS

LIST OF TABLES	vii
LIST OF FIGURES	viii
Chapter 1 : Introduction	1
1.1 Research Motivation	5
Chapter 2 : Background	7
2.1 Myanmar	7
2.2 Ayeyarwady Delta	7
2.3 Andaman Sea and Gulf of Martaban	10
2.4 Coastal hydrodynamic setting and monsoonal climate.....	11
2.5 Geological setting	14
2.5a Sunda Subduction Margin.....	16
2.5b Sumatra Fault Zone.....	17
2.5c Back Arc Spreading Center.....	18
2.5d Sagaing Fault	19
Chapter 3 : Methods and Materials	21
3.1 Chirp Sub-bottom Profiler and Seismic data	21
3.2 Sediment coring and sampling.....	23
3.3 InSAR Data to measure uplift and subsidence	24
3.4 InSAR data processing Workflow	25
Chapter 4 : Results	31
4.1 Sequence Stratigraphy and Transgressive Surfaces.....	31
4.2 Sediment Distribution and Thickness	34
4.2.1 Gulf of Martaban and Mouths of the Ayeyarwady	34
4.2.2 Martaban Depression	44
4.2.3 Bay of Bengal	47
4.3 Bookshelf Faulting and Martaban Canyon	50
4.4 InSAR Subsidence and Uplift Mapping	53
Chapter 5 : Discussion	55
5.1 Oceanographic controls on sediment thickness and distribution.....	55
5.2 A tale of two clinoforms	62
5.3 Delta shift and possible tectonic influence	67
5.4 Comparison to Major World River Deltas.....	76
Chapter 6 : Conclusions	79
FUTURE STUDIES.....	82

REFERENCES 83
APPENDIX..... 92

LIST OF TABLES

Table 1. Summary of the Modern Ayeyarwady and Thanlwin subaqueous delta characteristics based on geophysical profiles. (Liu et al., 2020).....	60
Table 2. Kasten Core location and water depth	93
Table 3. Focal mechanisms of major earthquakes in the Northern Andaman Sea since 1976.....	94

LIST OF FIGURES

Figure 1.1. Map of Southeast Asia illustrating the annual sediment discharge for each of the major rivers (Liu et al., 2009).	1
Figure 1.2. (A) MERIT 90m DEM of Myanmar and the locations of the three major rivers in the region (Ayeyarwady, Sittaung, and Thanlwin)(B): MERIT DEM 90 m of the Ayeyarwady Delta. Stars represent the mouths of the primary distributaries, from left to right: Pyamalaw, Ayeyarwady, To-Thakutpin.	3
Figure 1.3. Coastline gained and lost since 1925. Modified from Hedley et al., (2010).....	4
Figure 2.1. (A) River network of Myanmar. Green stars represent the three major distributaries in the delta. Yellow stars represent other major rivers in the region. The area of the Ayeyarwady delta is highlighted by a semi-transparent blue. (B) Close up of the major distributaries in the delta.....	9
Figure 2.2. Sediment distribution across the subaqueous delta and tidal range in the Northern Andaman Sea. (Rao et al., 2005)	10
Figure 2.3. Direction of suspended sediment transport due to the seasonal reversing monsoons. (A) The direction of sediment movement during the dominant SW monsoon, in which the current orientation is towards the SE. (B) The direction of suspended sediment during the NE monsoon, where a small portion of the suspended sediment escapes into the Bay of Bengal and the general current orientation is towards the NE (Rao et al., 2005).....	12
Figure 2.4. (A) False-color composite (B) processed image of A showing sediment concentration (C) Maximum extent of turbidity front during the spring tide (6m) (D) minimum during neap tide (2.9m) (E) westward plume transporting sediments	

- to the Bay of Bengal (F) MODIS satellite image during Ebb tide (G) MODIS satellite image during flood tide. White dashed line represents the maximum seaward extent of the turbid zone (modified from Ramaswamy et al., 2004)..... 13
- Figure 2.5. Geometry of the micro plate and the conditions required for formation. Oblique subduction under the overriding plate allows for along strike shear stress at the base; over time, this can break off the front edge of the over-riding plate and gradually develop into the micro plate. Diagram by (McCaffrey et al., 2008)..... 15
- Figure 2.6. Bathymetric map of the study area showing the location of major geologic features. Black arrows indicate spreading direction. AR = Alcock Rise; ASSC = Andaman Sea Spreading Center; BMP = Burma Micro Plate; SF = Sagaing Fault; SMP = Sunda Micro Plate; SR = Sewell Rise; SFZ = Sumatra Fault Zone. Black dashed line represents transition from Sumatran Micro Plate to Burma Micro Plate 16
- Figure 2.7. Northern Terminus of the SFZ showing the SFZ transforming into the Andaman Spreading Centers. Abbreviations: Sumatra Fault Zone (SFZ), West Andaman Fault (WAF), Andaman Spreading Center (ASSC), Sewell Rise (SR), Alcock Rise (AR). Figure modified from Natawidjaja et al., 2018..... 18
- Figure 2.8. Geological map of the Andaman Sea. Sagaing Fault (SF) outlined in black. Rectangle highlights location where the SF connects to the ASSC. A series of pull apart basins separates the northern SF, the ASSC, and the south Sagaing Fault. Dark blue rectangle indicates location of Figure 9. Modified from (Morley et al., 2016). 20
- Figure 3.1. Paul Liu on the deck of the Sea Princess preparing the CHIRP unit for deployment (12/2017)..... 23

- Figure 3.2. Transects from the December 2017 cruise of the Andaman Sea. The square symbols (ex: C6, C7) depict the locations of core sampling while the lines represent the geophysical transects collected by the 512i Chirp Unit. 24
- Figure 3.3. InSAR phase methodology as suggested by SNAP user guide 27
- Figure 3.4. A scatter plot of the displacement data produced from SAR imagery. The data compares annual displacement against coherence of the respective pixels. The yellow illustrates the area where the concentration of pixel coherence and yearly displacement is highest. The interval for the deformation map were determined by this plot (-0.06: 0.025). 29
- Figure 3.5 NDVI values for January 2016. Normalized Difference Vegetation Index (NDVI) measures “greenness” related to the amount of chlorophyll. So, areas of high NDVI should also be the greenest in the corresponding RGB image, with the exception of smaller waterways that also have high NDVI values. The validity of pixels in Sentinel 1 imagery depends on an NDVI value of < 0.7 (Hajj et al., 2018). The Ayeyarwady delta displays low enough NDVI values during the dry season to produce reliable Sentinel 1 results. The blue star indicates the protected mangrove sanctuary. 30
- Figure 4.1. Seismic Profile of Line 3(A) and Line 4(B). The prominent acoustic reflector (TS) appears at ~ 30 m water depth in both transects. ~8 m of well stratified, parallel Holocene layers have accumulated overtop the TS and infilled the relict channel structures. At the SW end of Line 4, the Holocene sediment begins to pinch out, indicating that this might be the southeastern-most extent of which Ayeyarwady derived sediment accumulate. 33

- Figure 4.2. Fence diagram of seismic profiles collected in the Gulf of Martaban. The red dashed line indicates the extent of Holocene sediment; the white dashed line indicates the maximum extent of the Turbid zone. Purple = Holocene; Green = relict. 36
- Figure 4.3. A simple Holocene sediment distribution map of the Northern Andaman Sea. 37
- Figure 4.4 Seismic Profile of Line 28 in the Gulf of Martaban. Holocene sediment thickness of < 10 m overlays a highly reflective transgressive surface. Sediment beneath the TS likely consists of med-coarse grained structure less sand. Acoustic blurring in the profile is a product biogenic gas derived from Pleistocene mangrove peat deposits 38
- Figure 4.5. Seismic profile of Line 9 located adjacent to the river mouth. This profile reveals the proximal facies of a shore attached clinoform, and the west-most segment of the deeper, compound clinoform. The HST (T1, T2) is separated into two segments, an early Highstand (T1) and a middle Highstand (T2). An MFS separates the HST from the TS. Seaward of the foreset, sediment gradually thins out until normal faults, and relict relief becomes the dominant feature. 39
- Figure 4.6. Seismic profile of line 10. A continuation of the shore attached clinoform from figure 21. A 10 m thick foreset and no bottomset. An MFS separates the TS from the deltaic deposits. In several locations, the TS has been eroded and replaced by a mix of relict sands and new muds..... 40
- Figure 4.7. Seismic Profile of Line 11 Shore attached clinoform revealing 10 m thick foreset. Due to the erosive nature near the mouths of the Ayeyarwady, bottomset accumulation is negligible. Seaward of 20 m water depth sediment composition is

a mix of relict sands and new muds. Kasten cores retrieved in this area yielded a Holocene sediment accumulation rate of $\sim 0.3 \text{ cm a}^{-1}$ (Kuehl et al., 2019). Similar to the other profiles of the shore attached clinof orm, the HST is divided into two fore stepping units, i.e., T1; T2, and separated by a sub-surface. An MFS separates the HST from the transgressive surface and appears to be truncated at the point at which the foreset stops..... 41

Figure 4.8. Seismic Profile of Line 12. Shore attached clinof orm lacking significant structure.

A 10 m thick foreset, gently dipping. The foreset exists between the 5 – 30 m water depths. At the -35m water depth, the Holocene sediment pinches out. A Kasten core (KC-22) was attempted; however, no sediment was able to be retrieved, likely due to the sandy composition of the subsurface (Kuehl et al., 2019). 42

Figure 4.9. Seismic Profile of Line 20: Hardened corals and a mixture of relict sands and modern mud dominate this area directly off the ‘mouths’ 43

Figure 4.10. Fence diagram of seismic profiles collected in the Martaban Depression and adjacent to the mouths of the Ayeyarwady. The red dashed line indicates the extent of Holocene sediment. Purple = Holocene; Green = relict. 44

Figure 4.11. Seismic Profile of Line 2 that shows the topset and foreset of a recently prograding sigmoid. This profile is part of the sizable distal depocenter nearing the Martaban Depression. This profile reveals > 50 m of mud accumulation in the foreset and the highest accumulation rates within the study area. Boxes represent the location of Kasten Cores (full index of the location of each Kasten Cores is found in Appendix A). 45

- Figure 4.12. Seismic Profile of Line 7 near the transition from the Gulf of Martaban to the Martaban Depression. Accumulation in the foreset ranges from 10-40m with sediment gradually pinching out towards the 132 m water depth. Seaward of the profile, there was no evidence of any sediment accumulation. 46
- Figure 4.13. Fence diagram of seismic profiles collected in the Bay of Bengal. The red dashed line indicates the extent of Holocene sediment. Purple = Holocene; Green = relict. 47
- Figure 4.14. Seismic Profile of Line 19 near the Rakhine coastline where mud thickness > 20 m. Accumulation rates become negligible in proximity to the mouths of the Ayeyarwady. 48
- Figure 4.15 Seismic Profile of Line 15, 16, 18 at the most Northern end of our survey in the Bay of Bengal, on the Western Rakhine Coastline. Sediment accumulation stays fairly consistent at ~25 m throughout each transect and gives no evidence to suggest that the sediment does not continue across the trench, into the Bay of Bengal. 49
- Figure 4.16. Close-up of the bookshelf faulting in Line 27 50
- Figure 4.17. Seismic Profile of Line 27 located in the Martaban Depression. This profile reveals a thick foreset bed of the clinoform with no bottomset, indicative of the erosive nature of the Andaman. Beneath HST is the TS that represents the base of the postglacial transgressive surface. Underneath the TS are the pre-Holocene units and relict sands. Holocene sediment appears to gradually thin at (-90 m) water depth, until it pinches out completely, where the predominant features are back-arc basin bookshelf faults..... 51

- Figure 4.18. Seismic profile of Line 24 in the Martaban Canyon head. There is no evidence of Holocene sediment accumulation on the floor of the canyon nor along the banks. . 52
- Figure 4.19. S1A InSAR displacement results averaged over 4 years (2016-2020) to provide an annual rate of displacement. A Boolean operator was used to exclude pixels with a coherence of less than 0.15. Warm colors represent uplift/aggradation and cool colors represent subsidence. The main distributaries of the Ayeyarwady River are identified. 54
- Figure 4.20. (A) Histogram statistics of the deformation dataset. From the figure, the majority of pixels fell between the -0.06 : 0.025 bins. (B) Percent of land deformation. The majority of the delta, 65%, is subsiding. Meanwhile only 10 % of the delta is currently at equilibrium and the remaining 25% experiences uplift or aggradation annually..... 54
- Figure 5.1. Highly turbid area with a patch of less turbid water. L1 = Line 1; KC-01 – Kasten Core 1. Sediment accumulation rates were calculated from excess ^{210}Pb geochronologies (Kuehl et al., 2019)..... 56
- Figure 5.2. SSC profile across the Ayeyarwady shelf. As SSC decreases, so too does turbid water energy (Modified from Ramaswamy et al., 2004). 57
- Figure 5.3. Sediment accumulation rate isopach. This reveals that the maximum footprint of the turbidity front reaches the ~ 40 m isobath, and the water becomes less turbid seaward of the 40 m isobath as the material begins to rapidly fall out of suspension. Accumulation rates reported by Kuehl et al., 2019. 58
- Figure 5.4. Isopach map of layer thickness based off seismic profiles reported in Table 1. 58

Figure 5.5. Conceptual model of the fate of Ayeyarwady derived river sediment to the Northern Andaman Sea. The dash circles represent the proximal depocenter near the river mouth, and the red circles represent the distal depocenter. Modified from Liu et al., (2009)..... 62

Figure 5.6. Western Pacific post-glacial sea-level curve (Liu et al., (2005)..... 64

Figure 5.7. Historical progradation of the Ayeyarwady delta. Lines 9-12 = Figures 21-24 (Modified from Giosan et al., 2018). 65

Figure 5.8. Cartoon of the Ayeyarwady Subaqueous delta. 66

Figure 5.9. Example of Arc Volcanism in the Northern Andaman Sea (Fujiwara et al., 2001)... 68

Figure 5.10. Location and focal mechanism of significant earthquakes ($M_w > 5$) near Myanmar since 1976. Earthquake data from Dziewonski et al., 1981; Ekström et al., 2012. The black dashed line outlines the Ayeyarwady delta. The blue dashed line represents the conceptual boundary between dilation and compression due to focal mechanisms..... 70

Figure 5.11. Geological features of the Andaman Sea. Abbreviations: AE: Australian-Eurasian motion; AB: Australian-Burma motion; AT: Australian-Trench motion (convergence across subduction zone); BE: Burma-Eurasian Motion; AR: Alcock Rise. The red dotted circle represents the area of reduced accommodation space. The blue dotted circle represents an area of increased accommodation space (Based on Srisuriyon et al., 2014; Morley et al., 2016)..... 71

Figure 5.12. SAR Deformation Map (Jan. 2016 – 2020). The warm colors represent uplift and the cool colors represent subsidence. Data was reclassified with a moving kriging window to identify patterns better. Symbols: : Thrust fault; rupture 1980

(15.72N, 94.76E); : Oblique dip slip; rupture 1978 (16.64N, 95.94E); Black dashed lines represent the boundary of compression..... 74

Figure 5.13. Shoreline change 1974-2018. (B) Accretion and Erosion map of the Ayeyarwady delta (C) Statistics of shoreline change per year. (D) Average shoreline change per year (1974-2018). Highlighted are the three primary distributaries that are responsible for discharging > 70% of freshwater and sediment from the Delta to the Andaman Sea (Chen et al., 2020). 75

Chapter 1: Introduction

Rivers are the primary transport conduit for terrestrial sediment to the global ocean. On average, four billion tons of sediment flows from the Himalayas and the Tibetan Plateau to the Pacific and Indian oceans annually. The Himalayas are among the youngest and most active mountain ranges on the planet. Steep relief and fast rates of tectonic activity coupled with the seasonal melting of 15,000 glaciers and an intense monsoon season results in the Himalayas containing the headwaters to seven of the world's major river systems (Liu et al., 2009). From the Tibetan Plateau, these seven rivers (Ganges-Brahmaputra, Ayeyarwady, Thanlwin, Mekong, Red, Pearl, and Yangtze) account for 30% of the world's total global fluvial sediment flux to the sea (Figure 1.1; Liu et al., 2009).

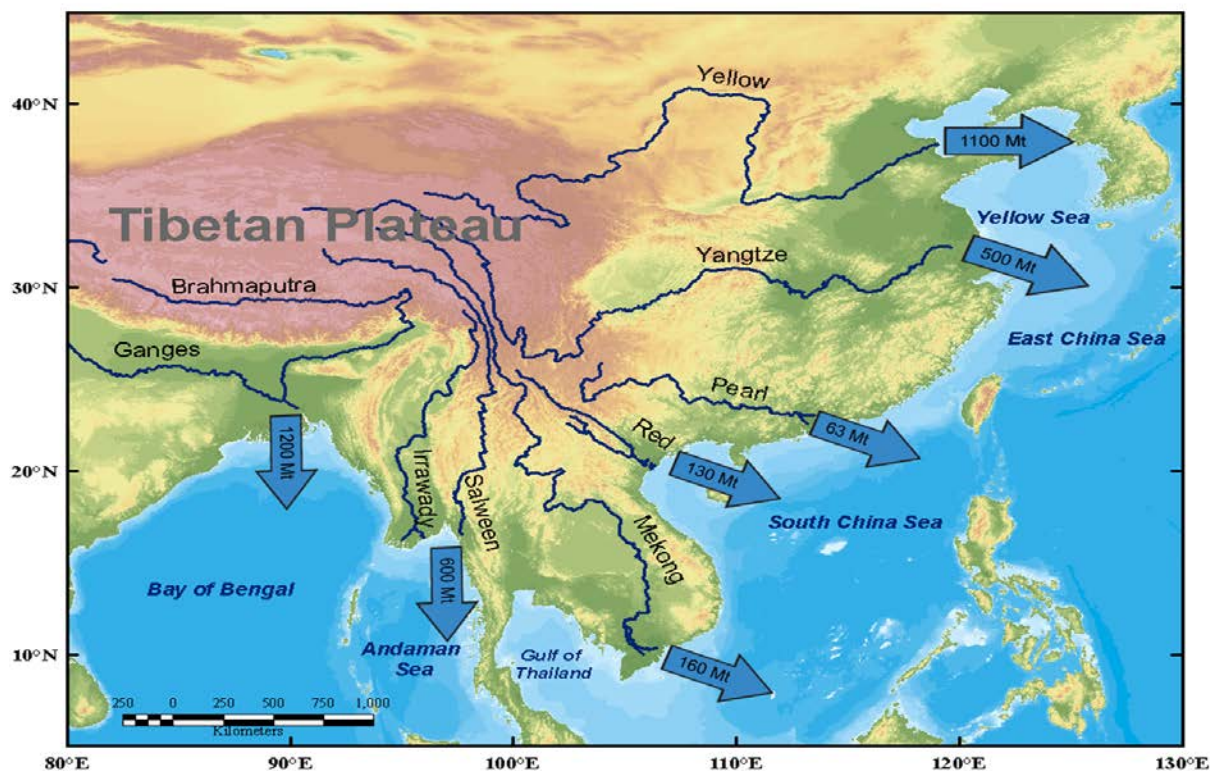


Figure 1.1. Map of Southeast Asia illustrating the annual sediment discharge for each of the major rivers (Liu et al., 2009).

The Ayeyarwady and Thanlwin rivers flow south and empty into the northern Andaman Sea. Still geologically young, the modern delta developed in the Middle Holocene, ~7,000 years ago, as a response to a post-glacial slowdown of sea-level rise (Stanley et al., 1994, 1997; Meade et al., 1996; Hedley et al., 2010). Throughout the Ayeyarwady delta's evolution, an average of 600 MT a⁻¹ of sediment has traveled from the Himalayas to the Indian Ocean through the three major rivers: the Ayeyarwady, Thanlwin, and Sittaung (Figure 1.2; Robinson et al., 2007). With no restriction on sediment flux, the Ayeyarwady Delta quickly evolved and prograded 270 km since the Holocene maximum transgression, or 40 m a⁻¹ (Hedley et al., 2010). However, evidence from recent geophysical surveys has revealed shoreline stasis for the past 150 years (Figure 1.3; Hedley et al., 2010), and even retreat (Anthony, et al., 2019).

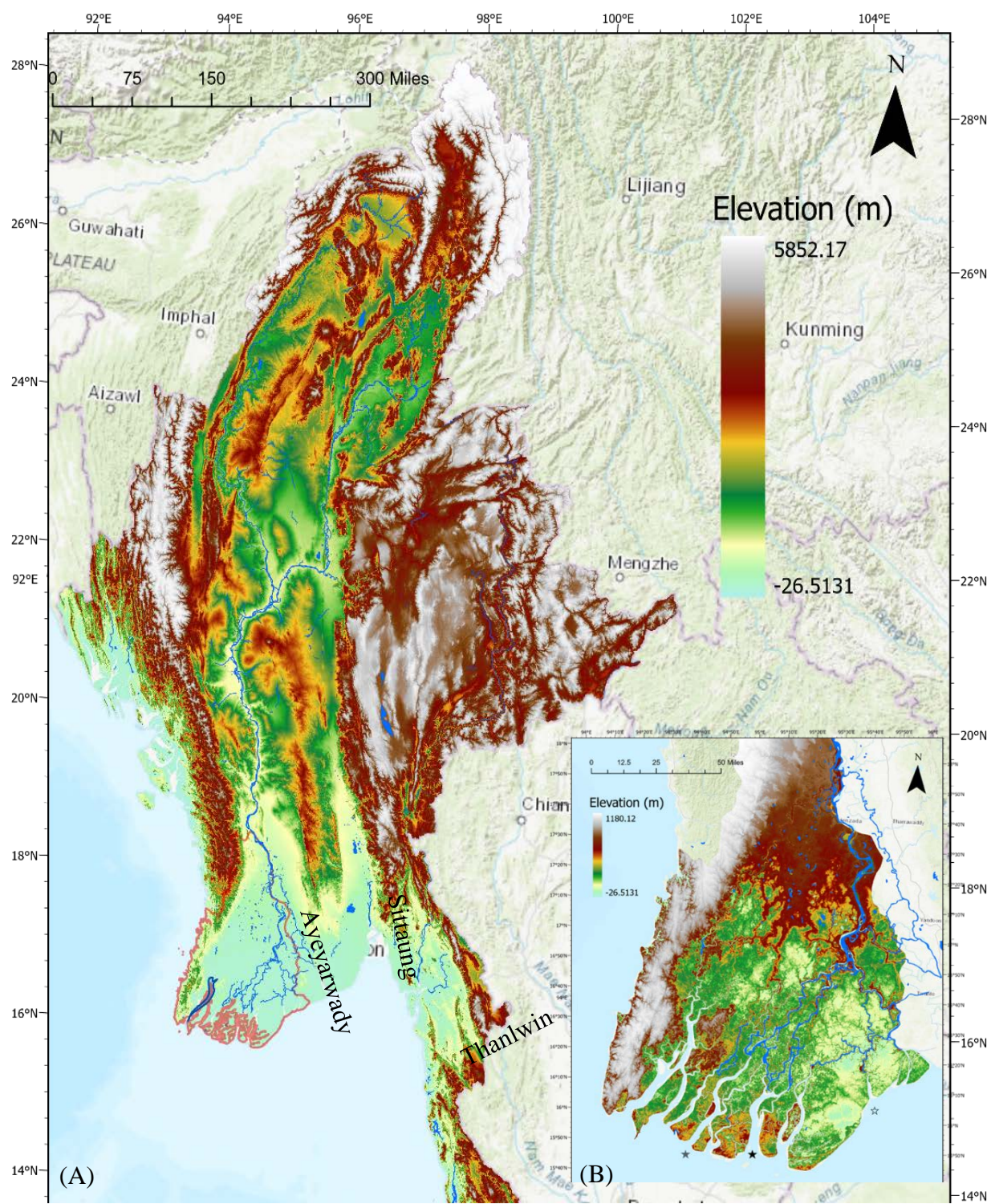


Figure 1.2. (A)MERIT 90m DEM of Myanmar and the locations of the three major rivers in the region (Ayeyarwady, Sittaung, and Thanlwin) (B): MERIT DEM 90 m of the Ayeyarwady Delta. Stars represent the mouths of the primary distributaries, from left to right: Pyamalaw, Ayeyarwady, and To-Thakutpin.

Presently, the Ayeyarwady and Thanlwin are the last free-flowing Asian rivers to remain undammed, outside of the Arctic (Grill et al., 2019). However, proposals to dam portions of these rivers for agricultural and hydroelectric purposes are underway (Schmitt et al., 2017). In doing so, sediment feeding the subaerial and subaqueous delta will likely be reduced, knocking the delta out the “equilibrium state” it is currently in (Hedley et al., 2010). The Ayeyarwady Delta is classified as a delta in peril, due in part to the imminent threat of damming, as well as the rising local sea level occurring at twice the rate of aggradation (Syvitski et al., 2009; Kuehl, et al., 2019). Therefore, the time is right to investigate why the delta entered its current state of equilibrium and what the future might hold for the Ayeyarwady Delta.

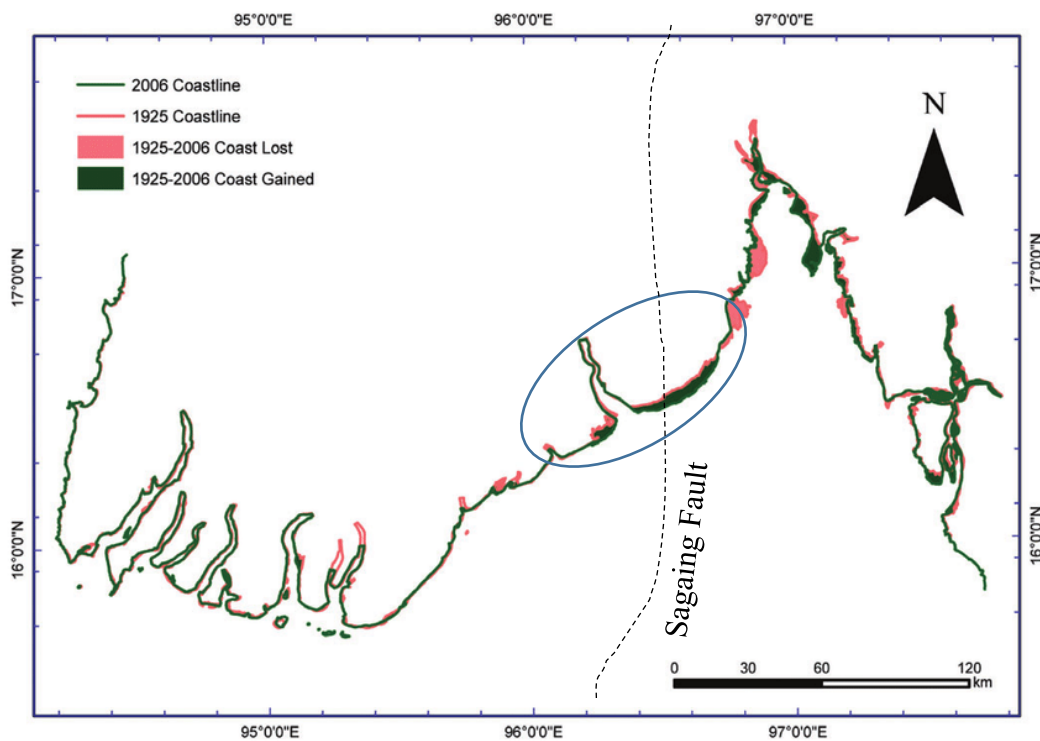


Figure 1.3. Coastline gained and lost since 1925. Modified from Hedley et al., (2010).

1.1 Research Motivation

Approximately 54 million people live in Myanmar, the majority of which reside in the Ayeyarwady Delta region and the principal city of Yangon. At present, the city is 2 m above sea level, making the area already prone to severe inundation and flooding from storm systems. For example, the Category-5 Cyclone Nargis made landfall in 2008 and was recorded as the worst natural disaster to hit Myanmar. The cyclone decimated the Burmese country, killing ~140,000 people, raised 95% of the buildings to the ground, and resulted in an estimated \$10B in damages. According to Fritz et al. (2009), land 50 km inland was inundated during the associated 1.9 to 5.6 m storm surge (Besset et al., 2017). Deltas naturally provide a morphosedimentary resilience to events like these through complex channel-pattern geometries and changes in sedimentation; however, modifications to the natural delta, like deforestation, excess groundwater extraction, and damming, can quickly remove any protection that a delta offers and lead to coastline retreat and increased erosion (Syvitski et al., 2009; Besset et al., 2017).

Globally, major river deltas are sinking relative to the local sea level due in part to a reduction in sediment getting to the flood plains and the effects of anthropogenic activities making the delta increasingly more vulnerable (Syvitski et al., 2009). 85% of significant world deltas, like the Ayeyarwady and the Ganges-Brahmaputra, experienced severe flooding due in part to increased human activities. Moreover, delta surface areas prone to inundation are expected to increase by over 50% according to the current, 21st-century sea-level rise projection (Syvitski et al., 2009; Brakenridge et al., 2017). Therefore, understanding why the delta has maintained a period of homeostasis for the last 150 years is essential to estimate how the delta will evolve in the near future due to the rapidly changing climate. This research aims to understand better the late Holocene history of the subaqueous Ayeyarwady Delta, and how fine-

grained riverine sediments are transported and deposited in the Andaman Sea through the use of high-resolution geophysical imagery.

The specific objectives of this thesis are:

- 1) What does the distribution and thickness of mud deposits in the Northern Andaman Sea indicate about the history and evolution of the subaqueous delta?*
- 2) What are the tectonic and oceanographic factors shaping sediment distribution in the Northern Andaman Sea and the Gulf of Martaban?*
- 3) Is the Ayeyarwady Delta in a period of equilibrium, and if so, what does this suggest for the future of the delta?*

Chapter 2: Background

2.1. Myanmar

As the largest country in Southeast Asia, Myanmar relies heavily on the Ayeyarwady Delta. Covering 61% of the territory of Myanmar, more than 20,570 km² of the Ayeyarwady Delta is cultivated, 60% of which is rice (Besset et al., 2017). However, over the last decade there has been a gradual shift in farming practices from rice to aquaculture (shrimp, fish, etc.). The delta is a flat, low lying plain that receives freshwater and sediment input from Ayeyarwady and Chindwin Rivers, along with several smaller distributaries (Hedley et al., 2010). The climate in Yangon is tropical, with noticeable wet and dry seasons of equal duration. The wet season occurs during the southwest monsoon, between mid-May and October, eventually transitioning to the dry season, the northeast monsoon, between December and February (Ramaswamy et al., 2008). During the southwest monsoon, the region sees nearly 89% of its total rainfall, and the river discharges upwards of 91% of its total annual load (Rodolfo, 1969; Ramaswamy et al., 2004). Since Yangon expanded in 1983, the population has doubled, increasing rapidly and prompting many studies on how the land is responding relative to water use. One such study, "Sinking Yangon," (Horst, 2017) explores this dilemma through the use of Interferometric Synthetic Aperture Radar (InSAR) and reveals how over-extraction of municipal groundwater supplies can lead to significant subsidence in densely populated areas.

2.2 Ayeyarwady Delta

The development of modern deltas, such as the Ayeyarwady and Thanlwin, is reflective of the slowdown of postglacial, eustatic sea-level rise during the Holocene, starting around 7 ka BP (Hedley et al., 2010). Most of the modern-day, tide-dominated deltas are located in tectonically active, low latitude regions and form along macrotidal coasts, fed by larger river systems in terms of sediment discharge such as the Ayeyarwady, Ganges, and Yangtze

(Goodbred et al., 2011). The continual exposure to large tidal ranges and high sediment loads allow for deltas, such as those mentioned above, to quickly prograde seaward. Extensive research by Middleton et al., (1991) and Goodbred et al., (2011) concluded that the development of tide-dominated deltas in macrotidal regions is amplified on where the continental shelves are broad, i.e., Bay of Bengal (Ganges-Brahmaputra), Gulf of Papua (Fly), Andaman Sea (Ayeyarwady), that are strongly connected to the open ocean and are close to an active orogeny. In high energy basins, like the Andaman Sea, the Himalayan-Tibetan uplift provides abundant sediment yield for the Ayeyarwady delta to form and prograde rapidly (Goodbred et al., 2011).

The Ayeyarwady River Delta is a mud-silt, tide-dominated system that is 300 km wide and 200 km N-S. The Ayeyarwady and Thanwlin Rivers rise in the eastern Himalayas and flow southward, through Myanmar, and are the primary source of freshwater and suspended sediment delivered to the Northern Andaman Sea (Rao et al., 2005; Ramaswamy et al., 2008;). The Ayeyarwady River stretches 2280 km and discharges into the Andaman Sea in the west through a series of smaller distributary channels. During the summer monsoon, 92% of the total sediment load discharged into the Andaman Sea occurs. There are nine total distributaries, though 76% of water discharged from the delta comes by way of the Pyamalaw, Ayeyarwady, and To-Thakutpin Rivers (Figure 2.1; Kravtsova et al., 2009).

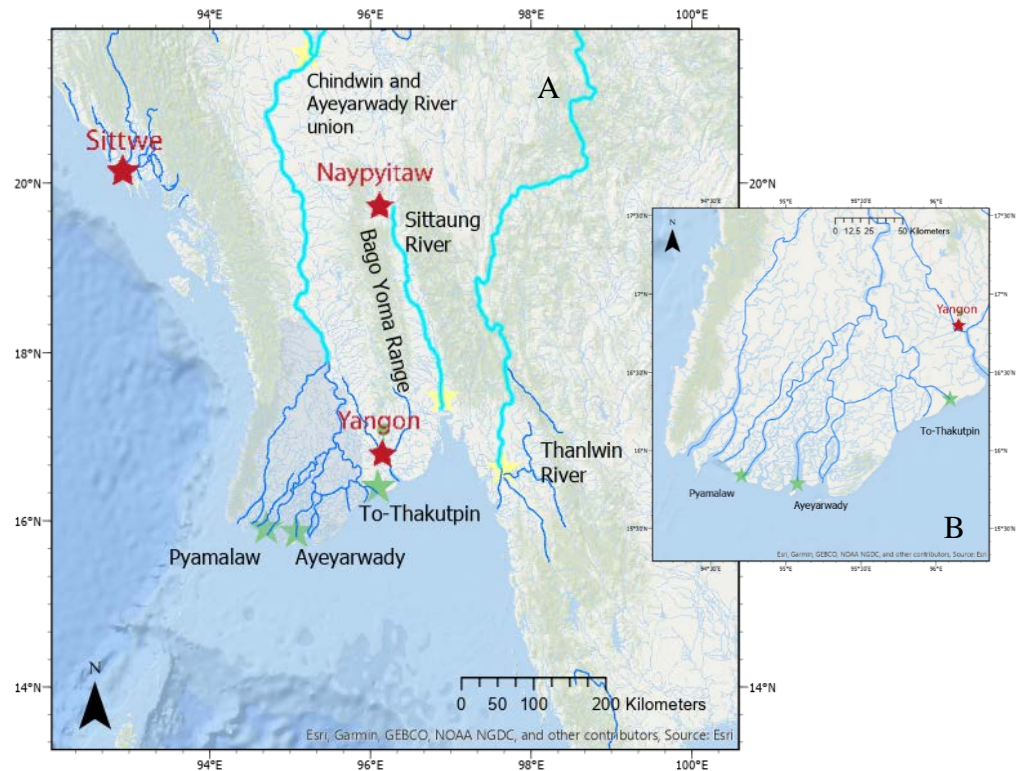


Figure 2.1. (A) River network of Myanmar. Green stars represent the three major distributaries in the delta. Yellow stars represent other major rivers in the region. The area of the Ayeyarwady delta is highlighted by a semi-transparent blue. (B) Close up of the major distributaries in the delta.

The Thanlwin River is 2400 km long and stretches from the Tibetan Plateau to the Andaman Sea, crossing through the Ayeyarwady-Thanlwin Delta in the east near Mawlaymine (Kuehl et al., 2019). The total catchment area of the rivers that drain the delta region is 0.7×10^6 km². It covers many lithologies including Eocene-Miocene through Quaternary sediments of the Myanmar Central Basin, the Cretaceous-Cenozoic Flysch of the Indo-Burman mountain ranges, and the Cretaceous-Eocene metamorphic rocks from the eastern syntaxis of the Himalayas (Robinson et al., 2007; Awasthi, 2014; Garzanti, 2016; Kuehl et al., 2019). The Ayeyarwady-Thanlwin contributes > 600 MT of suspended sediment discharge (SSD) annually, ranking as the third-largest river system in terms of SSD in the world. In terms of total annual organic carbon transport, the Ayeyarwady–Thanlwin combine to deliver half of the total dissolved load from the

Tibetan orogen to the oceans, a yield of 5.7 – 8.8 MT a⁻¹, and that is second only to the Amazon (Bird et al., 2008).

2.3 Andaman Sea and Gulf of Martaban

According to Rodolfo et al. (1969a), the offshore bathymetry of the Northern Andaman Sea is representative of a broad (120 km), low gradient continental shelf that increases in the east to 250 km wide in the center of the Gulf. The shelf break here is at 110 m depth, and surface sediment is estimated to be 50% modern and 50% relict (Rodolfo, 1969; Ramaswamy et al., 2004; Rao et al., 2005; Hedley et al., 2010). Of that sediment, 90% can be classified as siliciclastic, while the remaining 10% is carbonate. The Gulf of Martaban and the Bay of Bengal are underlain by silty clay that gradually transitions to sand and silt within the Martaban Depression (Figure 2.2; Ramaswamy et al., 2004). As the latitude decreases, the sediment transitions entirely to the sand fraction in the Martaban Canyon.

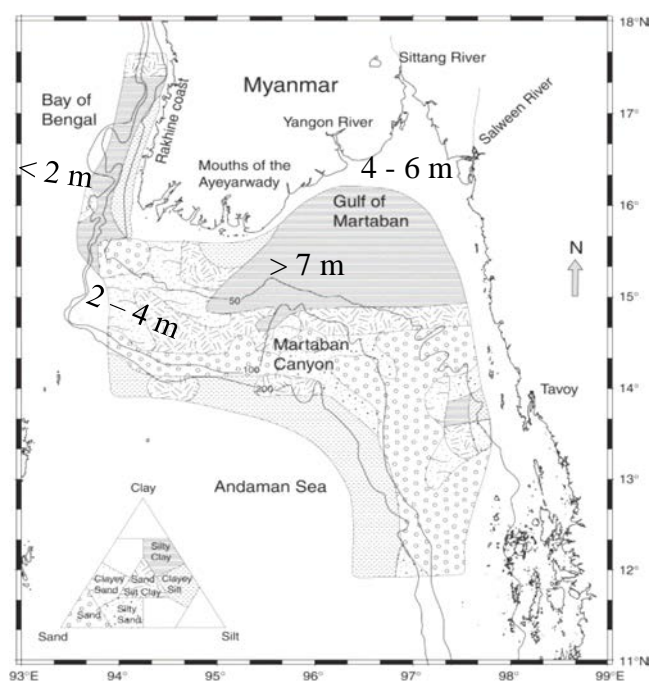


Figure 2.2. Sediment distribution across the subaqueous delta and tidal range in the Northern Andaman Sea. (Rao et al., 2005).

2.4 Coastal hydrodynamic setting and monsoonal climate

The Gulf of Martaban is macrotidal, and therefore it experiences perennially high suspended sediment in the Gulf and along the Ayeyarwady continental margin (Ramaswamy et al., 2004). The only significant changes to suspended sediment concentration in the Gulf of Martaban results from the spring-neap tidal cycles where the turbid zone extends to its maximum extent and retreats to its minimum (Ramaswamy et al., 2004). The area of the turbid zone oscillates in phase with spring-neap cycles, varying from 45,000 km² during spring tides, to 15,000 km² during neap tides (Rao et al., 2005). Tidal ranges average 6 m in the Gulf, but are highest in the west where tidal ranges regularly exceed 7 m. The mouths of the Ayeyarwady are mesotidal with a range of 2-4 m. In western Myanmar, along the Rakhine coast, the tidal range is generally less than 2 m. Tides in the Andaman Sea are semi-diurnal with the most influential currents occurring during the spring tide, reaching upwards of 3 m s⁻¹ in the Gulf (Rao et al., 2005). In response to the seasonal reversal of monsoon currents, the oceanic flow of surface waters in the Northern Andaman Sea changes twice yearly from cyclonic during the spring and summer to anti-cyclonic for the remainder of the year (Figure 2.3; Ramaswamy et al., 2004; Rao et al., 2005). During the summer monsoon, May–November, sediment is displaced eastwards into the Gulf of Martaban (Figure 2.3a), while during the winter monsoon, the current reverses and sediments are directed westwards, into the Bay of Bengal (Figure 2.3b).

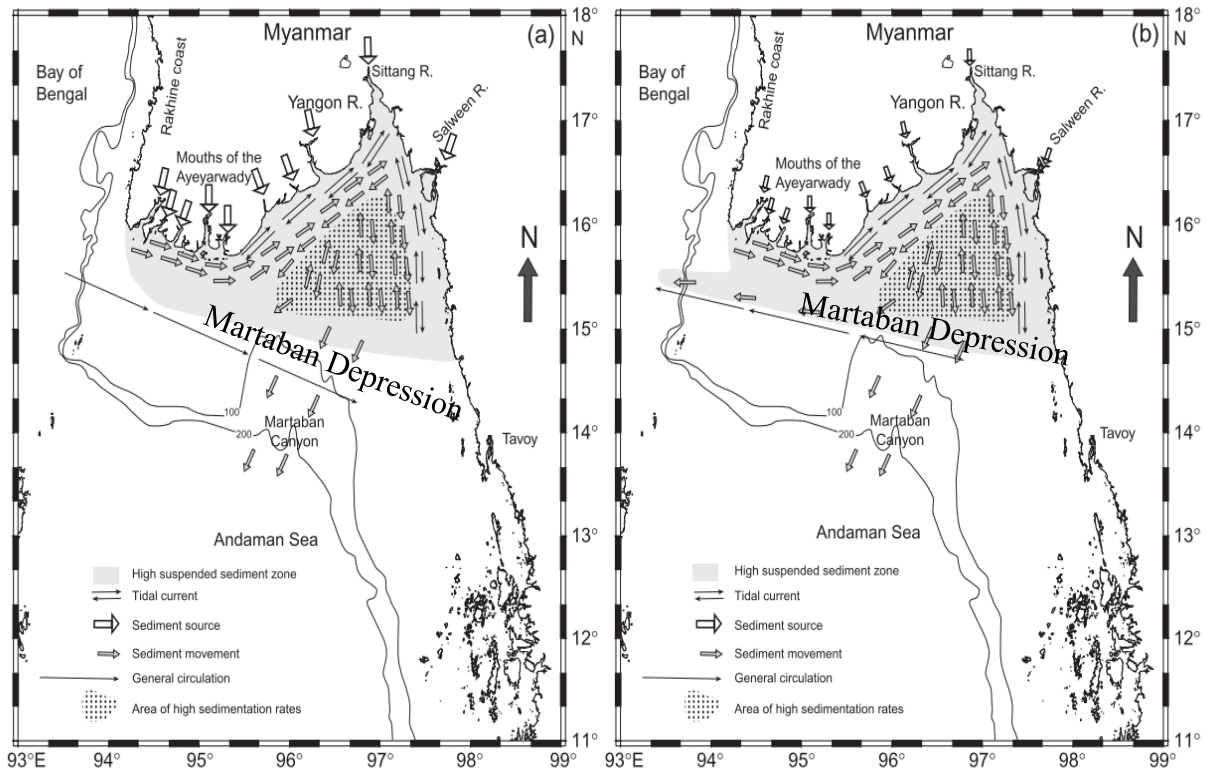


Figure 2.3. Direction of suspended sediment transport due to the seasonal reversing monsoons. (A) The direction of sediment movement during the dominant SW monsoon, in which the current orientation is towards the SE. (B) The direction of suspended sediment during the NE monsoon, where a small portion of the suspended sediment escapes into the Bay of Bengal and the general current orientation is towards the NE (Rao et al., 2005).

As seen in the satellite images, suspended sediment discharged by the Ayeyarwady is displaced by the tidal forces and prevailing westerly currents of the SW monsoon and becomes trapped in the Gulf of Martaban (Figure 2.4a, Figure 2.4b). When the turbid zone reaches its maximum footprint during the spring tide (Figure 2.4c), the suspended sediment forced into the Gulf can accumulate along the outer edge of the turbid front. During the neap tide (Figure 2.4d), the turbid front retreats to its most landward position, in which suspended sediment either stays in the turbid zone or accumulates in the Gulf. As the spring tide rotates back, sediment that accumulated in the Gulf is resuspended and then forced from the nearshore to the foreshore. Between December and February, the northern Andaman Sea is subjected to the northeastern

monsoon. Approximately 8% of total sediment discharge occurs during this time, much less than the 92% discharged by the summer monsoon. Throughout the winter monsoon, the incoming swell from the Bay of Bengal encourages sediment transport eastwards into the Gulf of Martaban. However, the NE directed winds also drive currents that transport suspended sediment in the Gulf towards the Bay of Bengal (Figure 2.4e).

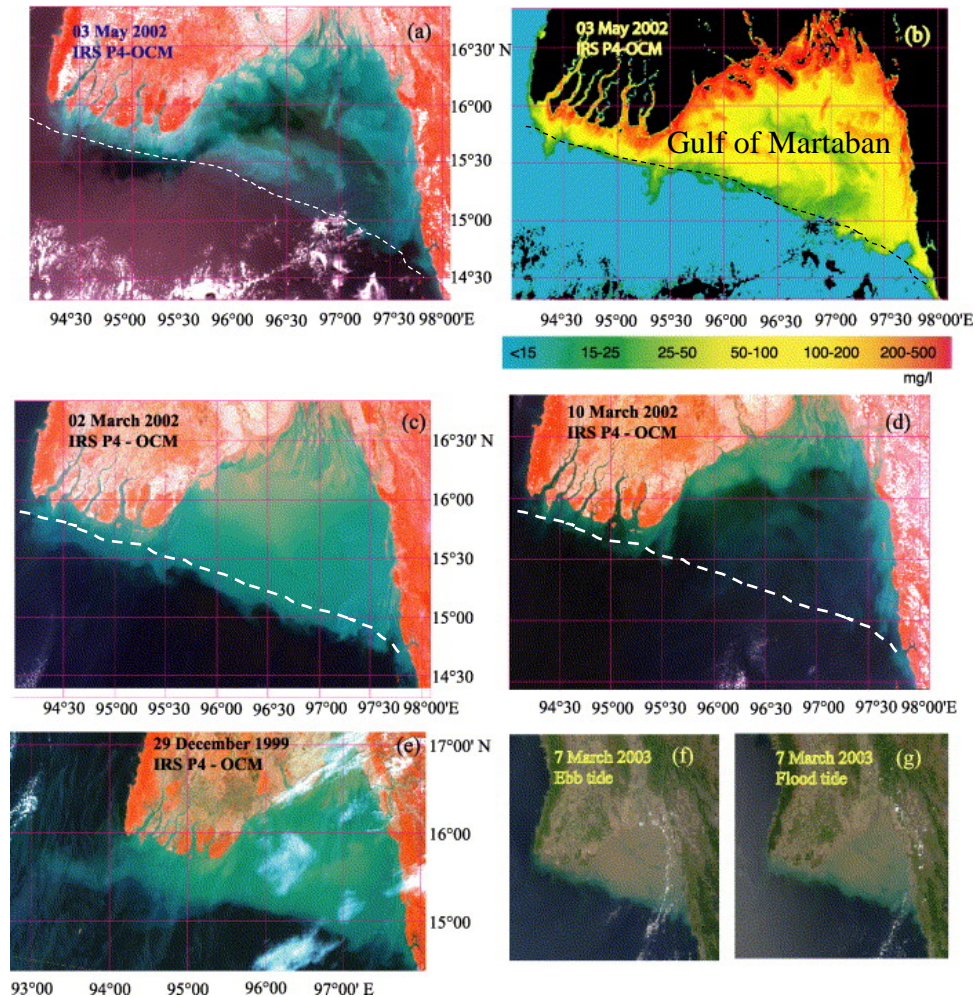


Figure 2.4. (A) False-color composite (B) processed image of A showing sediment concentration (C) Maximum extent of turbidity front during the spring tide (6m) (D) minimum during neap tide (2.9m) (E) westward plume transporting sediments to the Bay of Bengal (F) MODIS satellite image during Ebb tide (G) MODIS satellite image during flood tide. White dashed line represents the maximum seaward extent of the turbid zone (modified from Ramaswamy et al., 2004).

2.5 Geological setting

The Andaman Sea occupies a back-arc extensional basin, developed in response to the continual rotation of the obliquely converging Indian Plate relative to a fixed Eurasian plate (Curry et al., 2005). In the Paleogene, the Indian Plate began its oblique descent beneath the Eurasian Plate, forming the N-S striking Andaman trench and initiated the clockwise rotation of the Sunda Arc (Curry et al., 2005). During this time, transpressional crustal thickening and metamorphism occurred between Thailand and Myanmar as a result of the obliquely subducting plate (Srisuriyon et al., 2014). Through the coupling and decoupling of platelets and the formation of fault lines, a micro plate, known as the Burma Plate (or Burma microplate), developed (Figure 2.5), likely in the Eocene, that extended from Sumatra into the Sagaing Fault (Figure 2.6). The Burma Plate connects to the right lateral Sumatra Fault in the southwest in the back-arc of the Andaman Sea. Over time, the under-thrusting of the Indian-Australian plate pulled the Burma Plate northwards, relative to the Sunda Plate, subsequently resulting in the NE-SW “rhombochasm-like opening” of the Andaman Sea (Curry et al., 2005; Diehl et al., 2013).

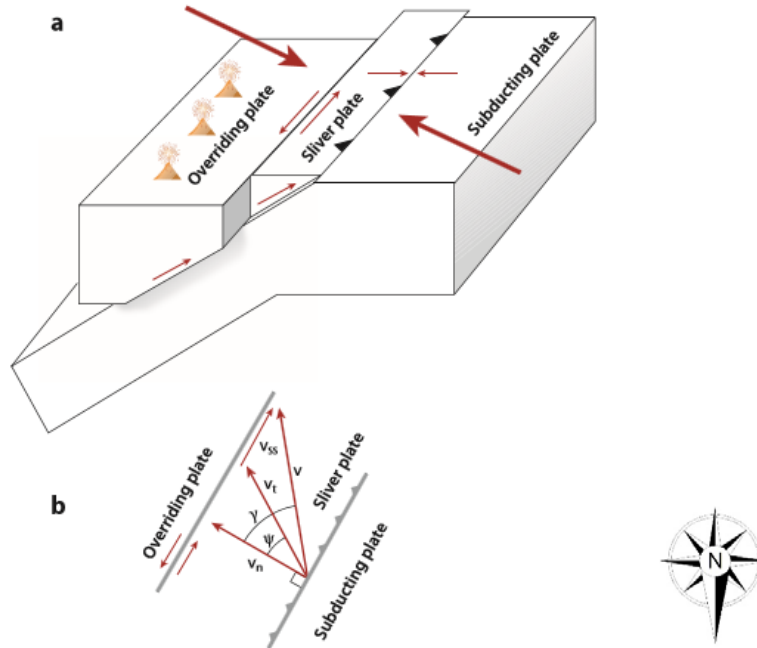


Figure 2.5. Geometry of the micro plate and the conditions required for formation. Oblique subduction under the overriding plate allows for along strike shear stress at the base; over time, this can break off the front edge of the over-riding plate and gradually develop into the micro plate. Diagram by (McCaffrey et al., 2008).

Presently, the Andaman Sea lies just above and behind the eastwardly dipping Andaman Convergence Zone, where convergence is highly oblique. Gradually, episodic back-arc extension normal to the direction of the subduction zone resulted in the pull-apart opening of the Andaman Basin. This oblique opening, combined with the extensive strike-slip faulting of the micro plate, led to increased spreading rates during the Eocene (Curry, 2005). The Andaman micro plate, or Burma Micro Plate, is connected in the south through a cluster of post-rift spreading basins and transform faults to the Andaman Spreading Center. In the north, it cuts across the Gulf of Martaban and the adjacent shelf to link to the Himalayan Syntaxis (Figure 2.6; Sloan et al., 2017).

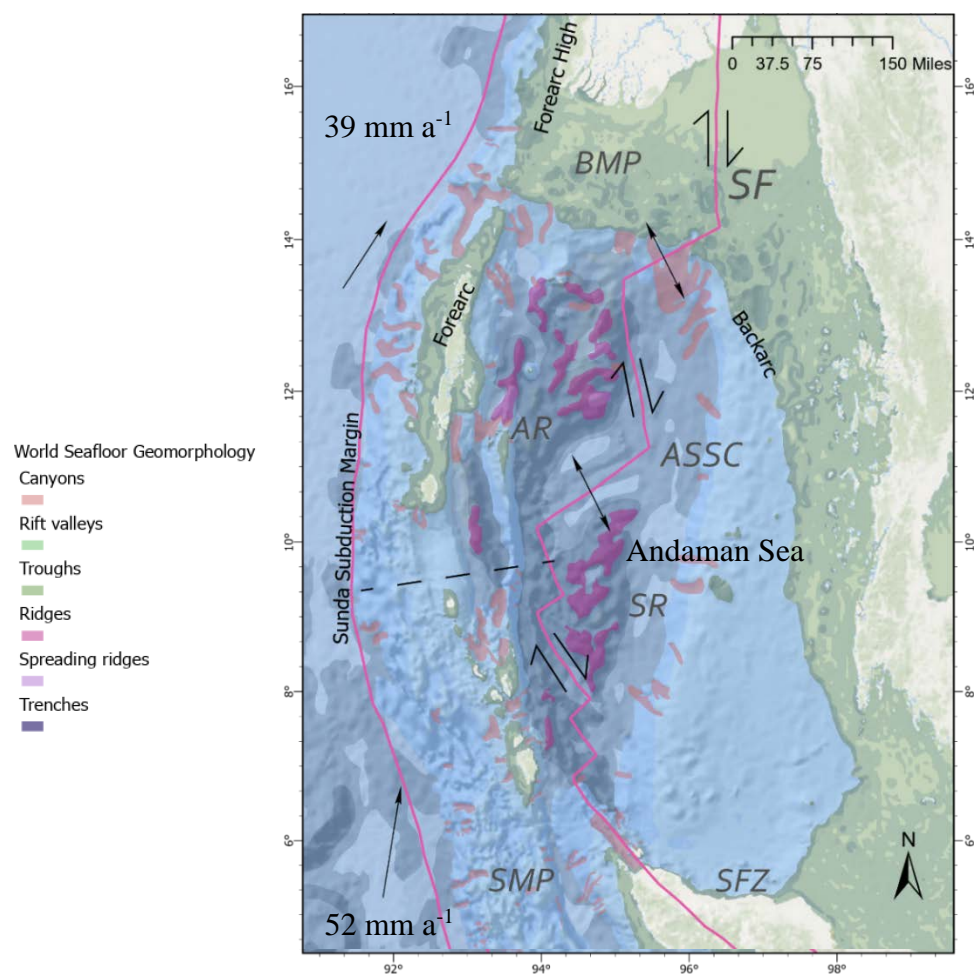


Figure 2.6. Bathymetric map of the study area showing the location of major geologic features. Black arrows indicate spreading direction. AR = Alcock Rise; ASSC = Andaman Sea Spreading Center; BMP = Burma Micro Plate; SF = Sagaing Fault; SMP = Sunda Micro Plate; SR = Sewell Rise; SFZ = Sumatra Fault Zone. Black dashed line represents transition from Sumatran Micro Plate to Burma Micro Plate.

2.5a Sunda Subduction Margin

The Sunda convergent margin marks the collision zone between the Indo-Australian Plate and the Eurasian Plate during the late Paleocene. Subduction along the margin has been dated back to the Late Cretaceous, shortly after the breakup of Gondwana (Moeremans et al., 2015). This collision at about 59 Ma initiated the clockwise rotation of the Sunda Subduction Zone, and gradually increased obliquity within the convergent margin (Curry, 2005; Moeremans et al., 2015). The zone extends well over 3,000 km, where convergence rates range from 63 mm a⁻¹ in

South Sumatra to 52 mm a^{-1} in Northern Sumatra, then decrease to 39 mm a^{-1} directly adjacent to the Andaman Islands (Moeremans et al., 2015). At 8° N subduction becomes highly oblique, an angle of $\sim 11^\circ$ from trench parallel with convergence rates decreasing from $34\text{-}14 \text{ mm a}^{-1}$ (Paul et al., 2001; Moeremans et al., 2015). As a result of oblique, clockwise rotation of the subduction zone, the Sunda forearc micro plate, or Sunda Micro Plate, which is sandwiched between the Sumatra Fault Zone and the Andaman trench, accommodates strain from trench-parallel convergent motion and is stretched, or strain is accommodated elsewhere, like deformation within the back-arc region (Natawidjaja, 2018).

2.5b Sumatra Fault Zone

The Sumatra Fault Zone (SFZ; Figure 2.7) is a 1900-km-long, highly segmented, dextral strike-slip fault running from the Sunda Strait and eventually transforming into Andaman Spreading Center in the north. The slip rate of the SFZ increases towards the northwest, from 6 mm a^{-1} in the Sunda Strait to 20 mm a^{-1} in the Aceh region (Natawidjaja, 2018). Only two of the nineteen segments, identified by Natawidjaja et al., 2000, are longer than 200 km. Therefore, it would appear that the slip area from single earthquake events is limited locally, and the magnitudes generally do not surpass $M_w < 7.5$ (McCaffrey, 2009). McCaffrey et al. (1991) estimated a uniform forearc stretching rate of $4 \times 10^{-8} \text{ mm a}^{-1}$ by using earthquake slip vectors as thrusting direction indicators. GPS slip rate estimates and slip rates from features offset by the SFZ are consistent with his prediction; however, he acknowledged that discrepancies regarding the specific geometry of deformation are not well understood (McCaffrey, 2009).

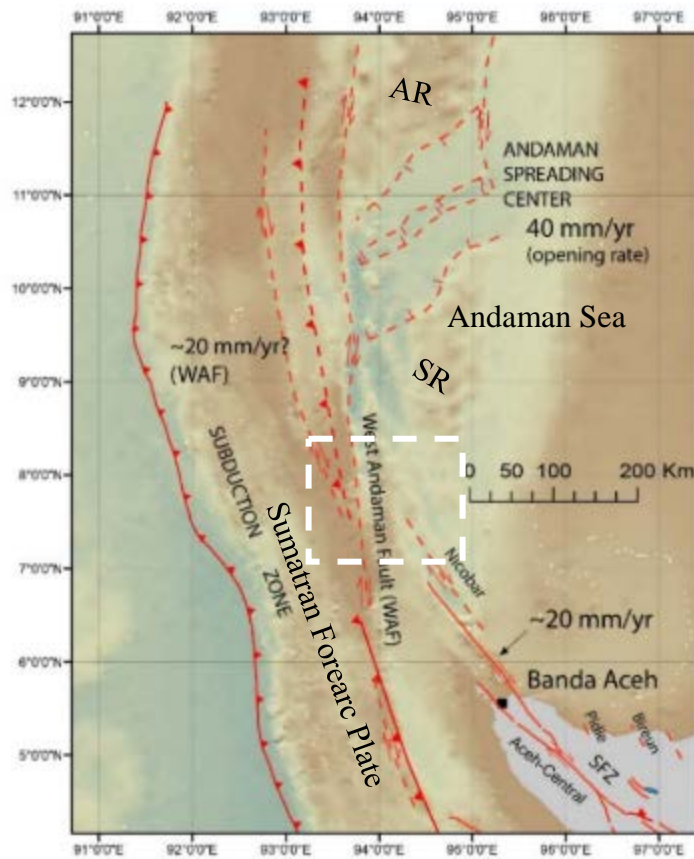


Figure 2.7. Northern Terminus of the SFZ showing the SFZ transforming into the Andaman Spreading Centers. Abbreviations: Sumatra Fault Zone (SFZ), West Andaman Fault (WAF), Andaman Spreading Center (ASSC), Sewell Rise (SR), Alcock Rise (AR). Figure modified from Natawidjaja et al., 2018.

2.5c Back Arc Spreading Center

The central basin of the Andaman Sea is dominated by the 400-km-wide Andaman Sea Spreading Center (ASSC) that is bounded by the Alcock Rise and Sewell Ridge, which act as a robust structural control locking into place the geometry and long term N25°W spreading orientation of the ASSC (Curry, 2005; McCaffrey, 2009; Diehl et al., 2013). The spreading rate within the ASSC has varied over time. In general, the spreading rate has increased from 15 mm a⁻¹ around 2 Ma to the current rate of 38 mm a⁻¹ (Carter et al., 2017a). Extension in the spreading

center involves the formation of new oceanic crust, unlike other pull-apart basins in which extension is driven by trench rollback (McCaffrey, 2009; Diehl et al., 2013).

2.5d Sagaing Fault

The Sagaing Fault (SF) is critical to the tectonic framework of Southeast Asia and is the defining geological feature in the eastern margin of the Andaman Sea (Figure 2.8). The 1,500 km strike-slip fault links two major tectonic domains--the eastern Himalayan syntaxis in the north and the Andaman Sea in the south (Curry, 2005; Sloan et al., 2017). The Sagaing Fault activated in the early Pliocene along with the ASSC (Bertrand et al., 2003; Srisuriyon et al., 2014). The eastern SF runs directly through the Gulf of Martaban and bisects the Thailand Peninsula, eventually linking to the Himalayas. In the south, the fault connects to the ASSC through a series of pull-apart basins and arc-parallel strike-slip faults (Figure 2.8; Morley et al., 2016). A permanent cGPS network across the southern and northern portion of the East Sagaing Fault reveals that the strike-slip fault is moving 34.34 mm a^{-1} NE and 40.61 mm a^{-1} SE (Sone Aung et al., 2016). As indicated by the cGPS network, the slip rates decrease as proximity to the primary SF decreases, suggesting that the western part of Myanmar might be more structurally locked than the eastern segment.

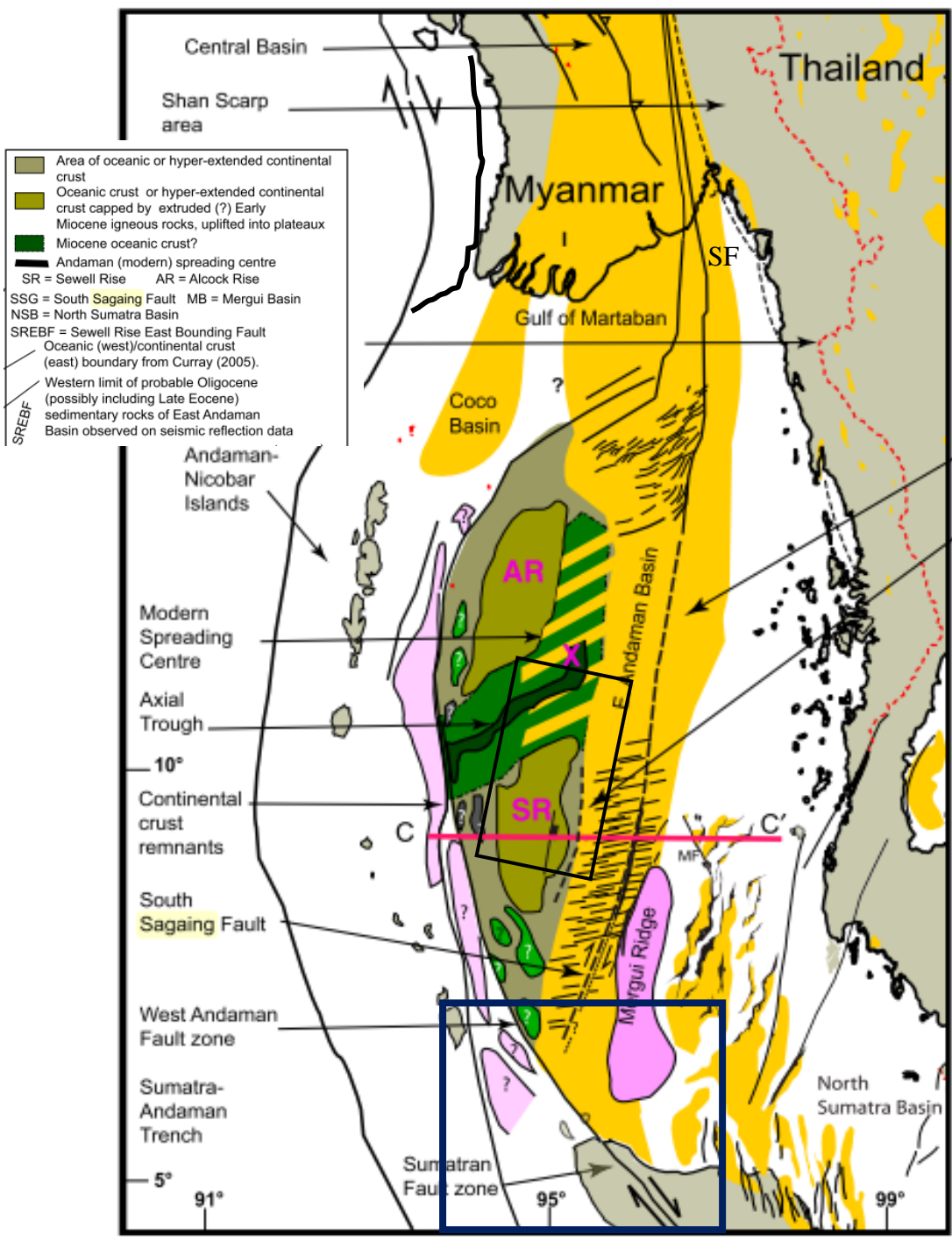


Figure 2.8. Geological map of the Andaman Sea. Sagaing Fault (SF) outlined in black. Rectangle highlights location where the SF connects to the ASSC. A series of pull apart basins separates the northern SF, the ASSC, and the south Sagaing Fault. Dark blue rectangle indicates location of Figure 2.7. Modified from (Morley et al., 2016).

Chapter 3: Methods and Materials

To answer the scientific questions mentioned above, we conducted a 14-day cruise using a local vessel (Sea Princess) in December 2017. The research cruise was a joint effort by scientists from Mawlaymine University, University of Yangon, Virginia Institute of Marine Science (VIMS), and North Carolina State University. More than 1500-km of high-resolution Chirp sonar data were collected from the Andaman Sea and the Bay of Bengal. To compare and calculate long-term tectonic deformation, we used four years (2016-2019) of Sentinel 1A Interferometric Synthetic Aperture Radar data obtained from the Alaska Satellite Facility. Thirty sediment cores were also collected on the cruise and analyzed post-cruise by researchers at VIMS.

3.1 Chirp Sub-bottom Profiler and Seismic data

Two Compressed High-Intensity Radiated Pulse (CHIRP) Sub-bottom Profilers, the 512i and the 424i, operating at frequency modulated (FM) pulses of 0.5–12 kHz and 4–24 kHz, respectively, were the primary methods of geophysical data collection during the December 2017 cruise. These instruments provide a 2D stratigraphic cross-section of the seafloor, by emitting an acoustic pulse from the transducer that travels through the water column. When the pulse hits the sediment layer, a portion of the acoustic energy is reflected towards the receiver mounted in the Tow-fish. The system uses Two-Way Travel Time (TWTT), and based on how long it takes for the pulse to travel from the transducer to the sediment layer, ping off the sediment, and travel back to the receiver, a measurement of depth is calculated by factoring in the speed of sound through water (1500 m s^{-1}). The intensity at which the pulse returns, and the time needed for it to return, is reflective of the acoustic impedance of the subsurface geology. The pulse emitted from a 512i or 424i will not penetrate bedrock or highly compacted sand, therefore when the pulse encounters this material, it is quickly reflected, and it is unable to record any stratigraphy.

However, if the sediment at which the pulse is directed is soft or loosely consolidated, then portions of the pulse will continue to ping through the stratigraphic layer where there are changes in acoustic impedance. The resulting image does not identify the composition of the sedimentary layers but instead changes in density, which can be interpreted as changes in stratigraphic layers. The same profiler has been extensively and successfully used on the shelves off the Mekong, Red, Yangtze and Yellow River mouths (Liu et al., 2004, 2007, 2009, 2017, etc.)

One thousand five hundred nautical miles of geophysical transects were collected aboard the *Sea Princess* during the December 2017 cruise in the Andaman Sea (Figure 3.2). The seismic profiles collected from the CHIRP 512i and the CHIRP 424i were processed using *Discover Sub-Bottom* software (SBP Version 38.0.1.113). Within the software, individual 300-megabyte .jsf profile files were played back, adjusted to reduce noise, captured, and then converted into image files. The line segments were then uploaded into Photoshop and pieced together to create the final TIF file. Transgressive surfaces viewed in the profiles were used as indicators to separate Holocene and pre-Holocene/relict sediment layers. Also, thicknesses of mud layers from individual seismic profiles were recorded and used to create a sediment thickness isopach of the Northern Andaman Sea and determine an approximate sediment budget.



Figure 3.1. Paul Liu on the deck of the Sea Princess preparing the CHIRP unit for deployment (12/2017).

3.2 Sediment coring and sampling

During the cruise, 30 Kasten, box, and gravity cores were collected (Figure 3.2). The Kasten cores were dissected on the ship in vertical increments of 2 cm and placed in plastic whirl bags. Wet samples for ^{137}Cs , ^{210}Pb , and ^{14}C analyses were frozen aboard, then shipped to the Virginia Institute of Marine Science (VIMS) for analysis. Samples from the gravity cores were acquired in 1-meter core barrels and then sealed, stowed, and shipped to VIMS for further analysis. At VIMS, the cores were processed by Dr. Steve Kuehl and his colleagues. There, his team measured ^{210}Pb geochronologies in all 30 cores, and a select few were also examined for ^{14}C age distributions. The sediment accumulation rates in all the seismic profiles listed in the results section were provided by Dr. Kuehl and his team.

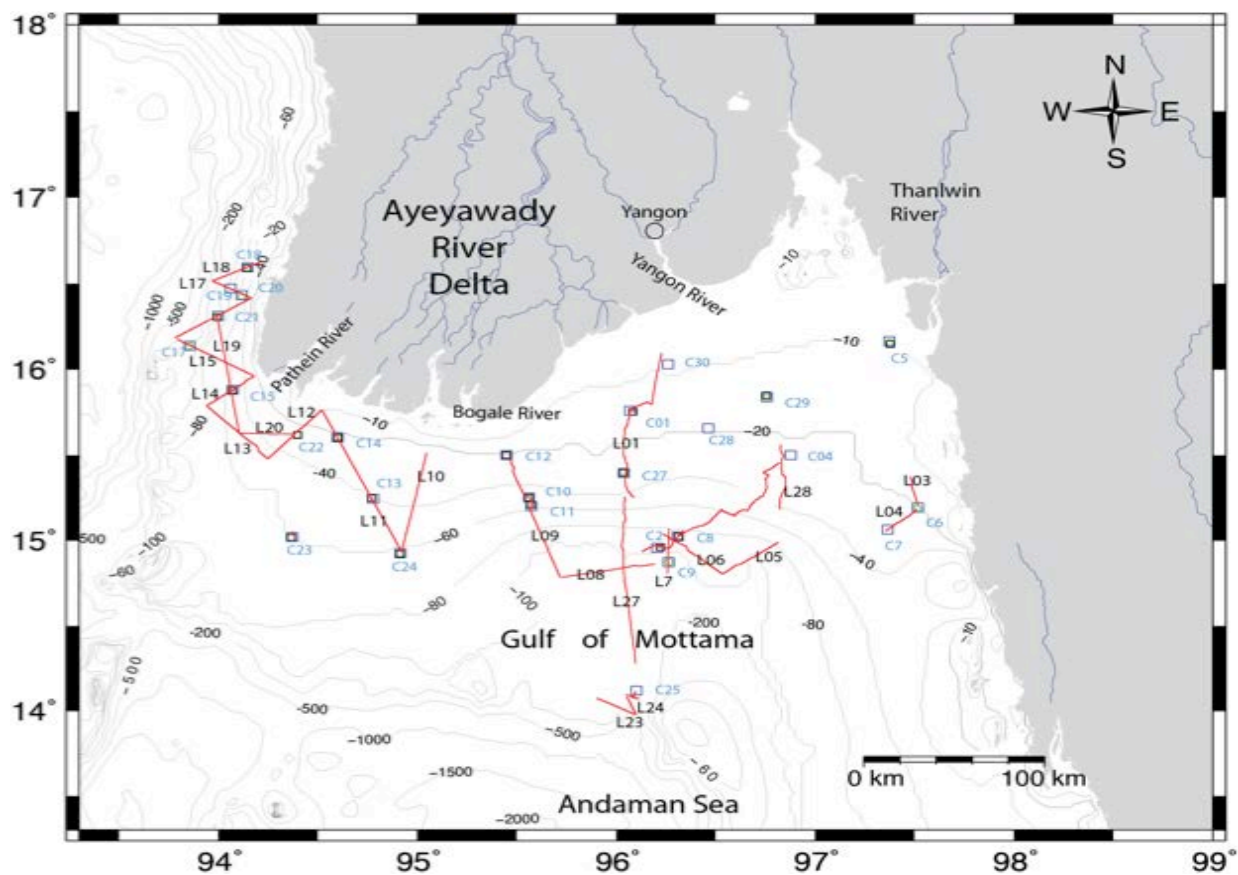


Figure 3.2. Transects from the December 2017 cruise of the Andaman Sea. The square symbols (ex: C6, C7) depict the locations of core sampling while the lines represent the geophysical transects collected by the 512i Chirp Unit.

3.3 InSAR Data to measure uplift and subsidence

Due to the lack of GPS observation stations across the Ayeyarwady Delta, Interferometric Synthetic Aperture (InSAR) was chosen to estimate surface uplift and subsidence over four years. The relatively low cost and open access for Sentinel-1 (S1) SAR data make the utilization of SAR imagery for research purposes possible. For instance, recent InSAR based studies have successfully determined subsidence rates over the Nile Delta (Gebremichael et al., 2018) and Ganges-Brahmaputra Delta (Higgins et al., 2014). For this project, data from the Sentinel 1A (S1A) satellite was acquired via the Alaska Satellite Facility Data Search Vertex. The images gathered were level-1 Single Look Complex (SLC), Interferometric Wide (IW), with

“VV” single-polarization, as suggested by the SeNtinel’s Application Platform or “SNAP” user guide (version 7.0.3). These images were acquired from January 2016–January 2020. This time frame was chosen because agricultural areas during the rainy season (summer monsoon) do not provide consistent results; however, during the dry season, they are sufficiently stable to surpass any temporal decorrelation (Horst, 2017).

The S1 satellite observes the earth at a frequency of six days, with each SAR image covering a 250 km swath while providing a spatial resolution of 5 x 20 m (Cian et al., 2019). The single look complex (SLC) IW type was chosen because it is capable of returning complex magnitude, phase, and amplitude (Q and I), values which are necessary for determining land displacement. The return is georeferenced using data from the satellite and produced in zero Doppler geometry, a standard option for slant range SAR imagery (SNAP user guide). SNAP exploits the phase information acquired by two SAR images of the same area from different dates. The flowcharts in Figure 3.3 provide the methodology used to measure large scale deformation of the Ayeyarwady delta.

3.4 InSAR data processing workflow

The following workflow was created using the Sentinel-1 Toolbox (S1TBX) version 7.0.2. For the first phase, the orbital information of one of the January 2016 images was collected along with the corresponding orbital information of a January 2020 image. S1A orbital information has a latency of 20 days and an accuracy of 5 cm (Horst, 2017). This information was used as the *read* and *read1* in the first phase (Figure 3.3). Coregistration is a vital part of interferometric processing. In order to accurately stack the time-series images, two or more images of the same orbit and area are required (SNAP User Guide). One image is selected as a “Dominant,” while the other is defined as the “Subordinate.” In this way, the “Subordinate”

images will align range and azimuth with the “Dominant” images to ensure sub-pixel accuracy (Horst, 2017). The alignment of the Master and Slave images must be accurate to within $1/1000^{\text{th}}$ of a pixel, as any difference in squint angle to ground targets can lead to a sizeable Doppler-centroid variation that will result in a phase jump at burst boundaries (Horst, 2017). SNAP offers several resampling methods to interpolate data. This study utilized bicubic interpolation. Though computational time far exceeded other methods, such as nearest-neighbor or bilinear interpolation, bicubic interpolation produced much more realistic results. The Enhanced-Spectral-Diversity method was used to counteract any phase jumps that might occur. This method estimates a constant azimuth shifter between images that drastically lowers any discontinuities between bursts. Finally, an interferogram stacking tool is applied to stack all the bursts together, resulting in a continuous interferogram. To obtain the complete interferogram after mosaicking the three swaths together, the Terrain Observation with Progressive Scans SAR or “TOPSAR”-Deburst tool was used. The “debursting” package removes the black bands from the sub-image, and by doing so, seamlessly joins the bursts into a single image (Horst, 2017).

The TOPSAR merge tool was used to rejoin the swaths that were separated before the first phase. Doing this after phase 1 allows for improved coherence between the images because the noise from temporal or geometric decorrelation and volume scattering may result in non-coherent conditions that can subsequently corrupt the interferometric phase. Therefore, merging after the processing of the individual swaths allows for more coherent conditions, as is imperative when monitoring subsidence and uplift with InSAR (Horst, 2017).

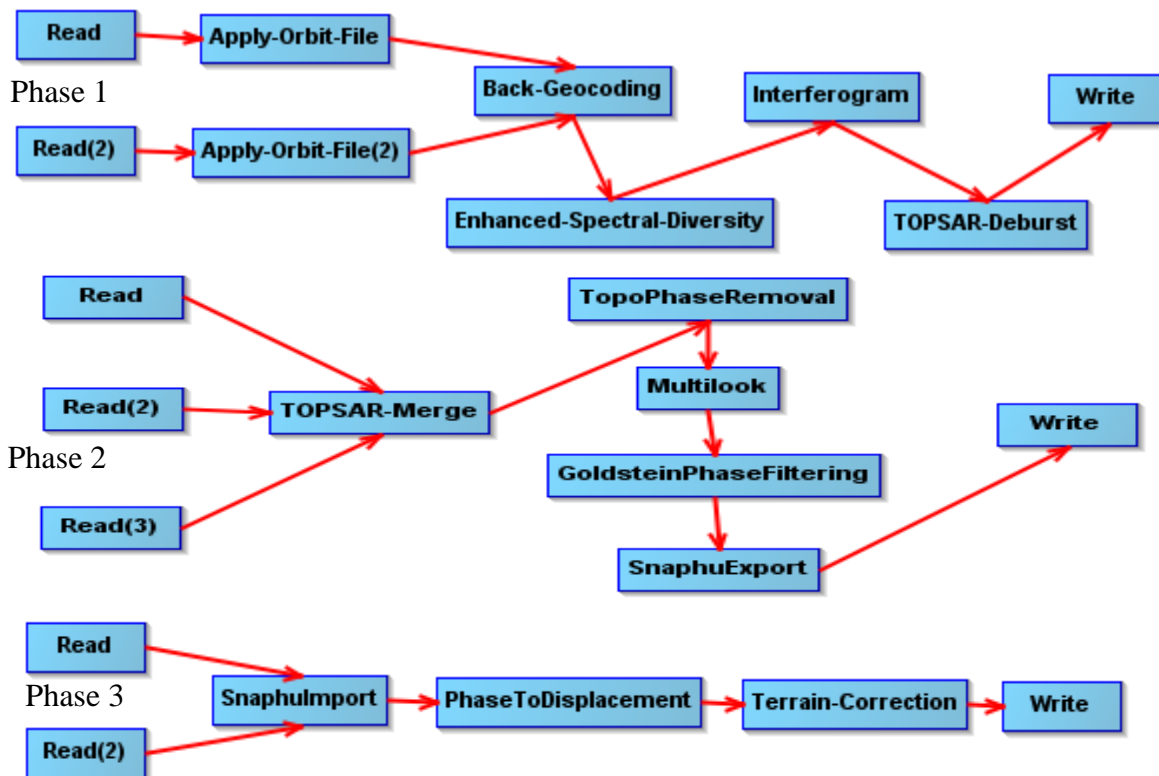


Figure 3.3. InSAR phase methodology as suggested by SNAP user guide.

Phase 2 concentrates on noise reduction while maintaining spatial resolution. After topographic phase removal, the interferogram may still appear noisy. The Multilook tool minimizes this noise. The multilook tool improves interpretability and reduces speckle noise produced by the original SAR imagery (SNAP User guide). To account for any loss of coherence, the signal to noise ratio must be increased which can be done by filtering the wrapped phase and applying the Goldstein Phase Filter with a pre-defined algorithm (Horst, 2017). The Goldstein Phase Filter adjusts the interferogram based on the power spectrum filtering parameter, patch size of the InSAR phase, and the smoothing window of the power spectrum (SNAP User Guide; Horst, 2017). The final tool used in phase 2 is SNAPHU export. SNAPHU is an algorithm developed by Chen et al. (2002) that determines the most likely unwrapped output based on the observed input data. This program applies the Statistical-cost Network-flow

Algorithm for Phase Unwrapping (SNAPHU) by viewing the product as a maximum a posteriori probability estimation problem. The interferometric phase in its original product is ambiguous and, therefore, cannot be related to topographic height. However, phase unwrapping integrates the phase difference between neighbor pixels, and by removing any ambiguous altitude integers, a phase variation between points on an interferogram is determined, subsequently providing the actual altitude (Chen et al., 2000; 2001; 2002).

Phase 3 begins by importing the unwrapped phase back into SNAP along with the filtered file generated during Phase 2 from the application of the Goldstein Filter tool. Once the interferometric phase is imported, the Phase to Displacement operator is applied. This function, designed by Ferretti et al., (2007), converts the interferometric phase into a displacement map with units of meters. Finally, the Range-Doppler Terrain Correction operator was applied to compensate for any image distortion due to the topographic variation and tilt of the satellite sensor (SNAP user guide). The final displacement maps of the study area were then mosaicked together using the SAR Mosaic operator and resampled using bilinear interpolation. A variety of other resampling methods were tested; however, this proved to be the most accurate. Pixels with a coherence of > 0.1 were removed by application of a Boolean term to the final displacement map. For the annual displacement map, pixel coherence improved, and therefore the coherence threshold was set to > 0.15 .

Coherence in a deformation map is essential. Therefore, to reduce any misguided interpretation, limits on visible data were applied. As indicated by the corresponding scatter plot to the displacement map (Figure 3.4), upon which the displacement versus coherence is plotted, and a greater concentration of pixel coherence in the displacement interval of $-0.066: 0.025$ is observed. Thus, the color scale was fit to the -0.066 to 0.025 m a^{-1} interval by making pixels

outside of this range transparent. To smooth out the data for better interpretation, a moving kriging window based on the number of pixels was applied (Figure 4.20). This reclassification tool created 14 bins and used bilinear interpolation to average between sets of neighboring pixels.

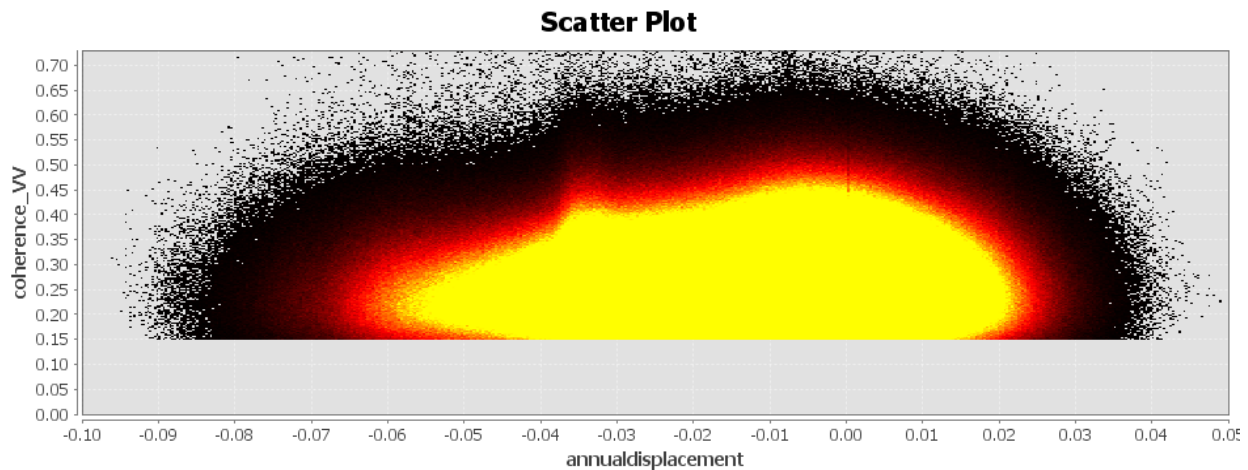


Figure 3.4. A scatter plot of the displacement data produced from SAR imagery. The data compares annual displacement against coherence of the respective pixels. The yellow illustrates the area where the concentration of pixel coherence and yearly displacement is highest. The interval for the deformation map were determined by this plot (-0.06: 0.025).

Normalized Difference Vegetation Index (NDVI) measurements were made of the survey area using multispectral Landsat-7 data downloaded from USGS in order to verify the validity of the data time frame. The equation for NDVI is:

$$NDVI = \frac{NIR - VIR}{NIR + VIR}$$

Equation 1. NDVI calculation. NIR = Near-infrared, VIR = Visible-infrared

In previous studies, it has been shown that the validity of pixels in Sentinel 1A imagery in delta settings is dependent on NDVI values of < 0.7 (Hajj et al., 2018). If the NDVI values are higher than 0.7, it indicates that radar cannot penetrate through the tree canopy, and therefore, the data cannot be relied on to produce an accurate time series of vertical deformation. The NDVI values

in January 2016 are low enough that the Sentinel 1 data collected over the same time frame, can be relied on (Figure 3.5). The highest NDVI values reside in the protected mangrove sanctuary and small waterways; however, these values still do not surpass the pixel validity threshold recommended by Hajj et al., (2018).

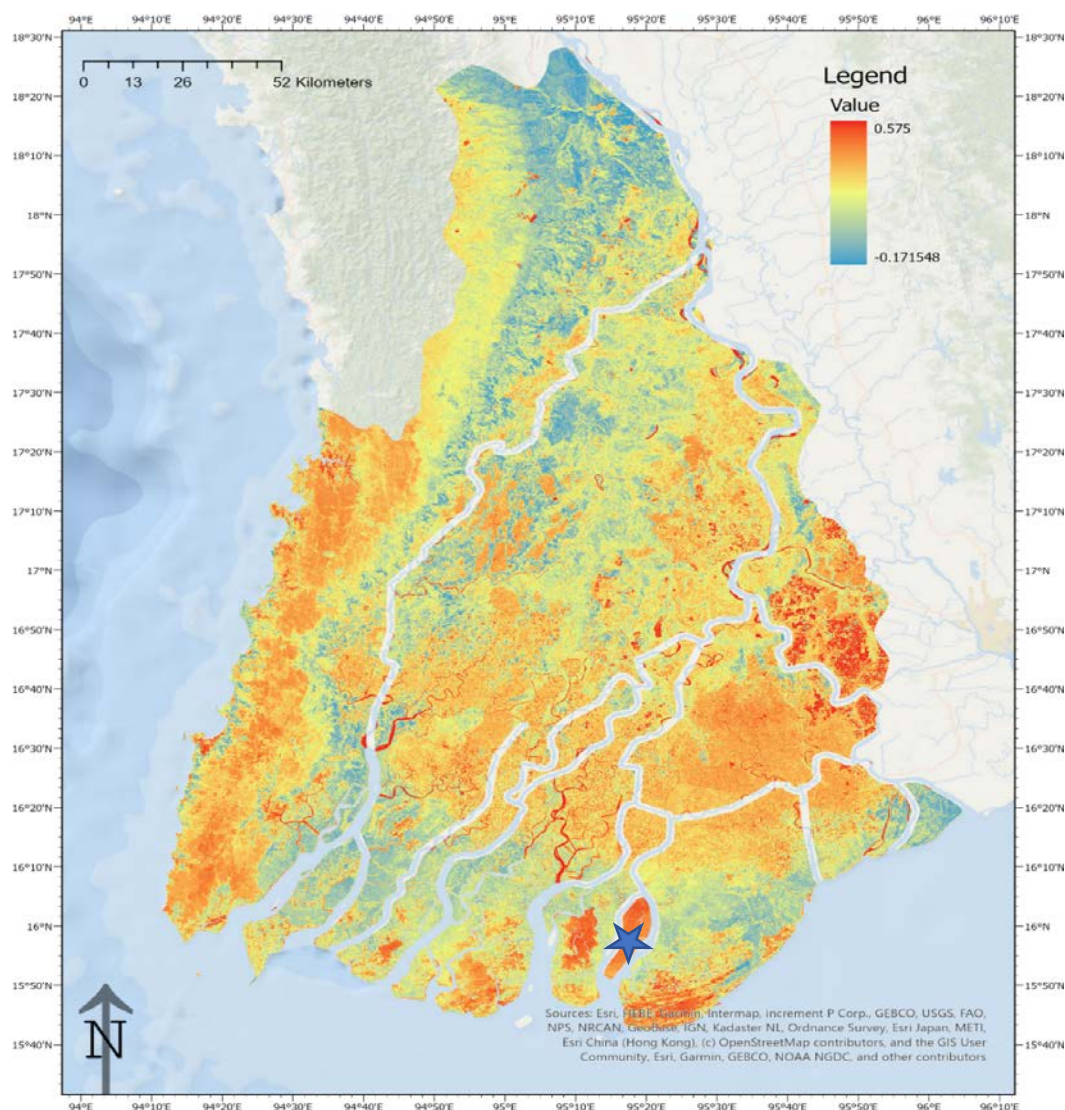


Figure 3.5. NDVI values for January 2016. Normalized Difference Vegetation Index (NDVI) measures “greenness” related to the amount of chlorophyll. So, areas of high NDVI should also be the greenest in the corresponding RGB image, with the exception of smaller waterways that also have high NDVI values. The validity of pixels in Sentinel 1 imagery depends on an NDVI value of < 0.7 (Hajj et al., 2018). The Ayeyarwady delta displays low enough NDVI values during the dry season to produce reliable Sentinel 1 results. The blue star indicates the protected mangrove sanctuary.

Chapter 4: Results

In this section, I present the results from the CHIRP sonar profiles, including the sequence stratigraphy, sediment distribution, and bookshelf faulting, as well as the uplift and subsidence rates derived from the InSAR analysis.

4.1 Sequence Stratigraphy and Transgressive Surfaces

The following section provides a comprehensive look at the CHIRP Acoustic Image Profiler results. Stratigraphic interpretations of seismic profiles are based on the presence or absence of acoustic reflectors. Variations in the character and spatial relationships among reflectors yield insight into the sedimentary, tectonic, and oceanographic history of a geologic basin (Van Wagoner et al., 2003). In the seabed, the strength of a reflector varies depending on the acoustic impedance of the sediment. Generally, there is a direct relationship between grain size and acoustic impedance; thus, as grain size increases, the strength of the reflector does as well. In contrast, weak reflectors indicate low acoustic impedance and suggest smaller sediment grain size (Alexander et al., 1986; Velozzi, 2004).

The seismic profiles recorded during the December 2017 Sea Princess cruise reveal an acoustically opaque subsurface overlain by a prominent acoustic reflector and an acoustically transparent, compound cliniform. When compared to similar subaqueous deltas like the Yangtze, Yellow, and Mekong (Liu et al., 2004, 2007, 2017), the prominent acoustic reflector appears to be the base of the post-glacial transgressive surface (TS) (Figure 4.1). The opaque subsurface residing beneath the TS is likely pre-Holocene sands, channel structures, and hardened corals (Figure 4.8 & Figure 4.9). The appearance of the TS indicates that the sea level rose rapidly, flooding the relict sands and refilling the channel structures. In doing so, the top surface was truncated, leaving behind a distinct unconformity (Figure 4.1). Thus, the TS in this study is used to separate Holocene sediment from post-Last Glacial Maximum (LGM), latest

Pleistocene sediment. In several profiles, Holocene sediment accumulation pinches out before the termination of the TS, indicating that there is a definable boundary at which Ayeyarwady derived sediment accumulates or does not accumulate (Figure 4.1, Figure 4.12, Figure 4.17).

The transgressive surface is covered by a thin Transgressive System Tract (TST) and then capped by a maximum flooding surface (MFS), marking the maximum landward position of the Andaman Sea shoreline during the Holocene (Figure 4.5, Figure 4.6, Figure 4.7; Mitchum et al., 1977). This surface separates the prograding clinoform from the transgressive surface and signals that the sediments above the MFS are part of the highstand system tract (HST) (Figure 4.5, Figure 4.17). These HST sediments make up a part of the Ayeyarwady derived subaqueous clinoform that extends to the 130 m water depth in the Martaban Depression. Several transects shed light on the complex inner structure and evolution of the subaqueous clinoform. For example, in the shore attached clinoform the HST is divided into two fore-stepping sigmoid units (T1 & T2) separated by a truncated subsurface; T1 and T2 are interpreted to be early highstand and late highstand, respectively (Figure 4.5). The T1 and T2 layers are overlain by a highly reflective T3 layer that has accumulated overtop the landward segment of the profile. The occurrence of the T3 layer suggests that the clinoform has increased in proximity to the river mouth, where coarser-grained sediments are preferentially depositing, and finer-grained sediments are restricted from accumulating.

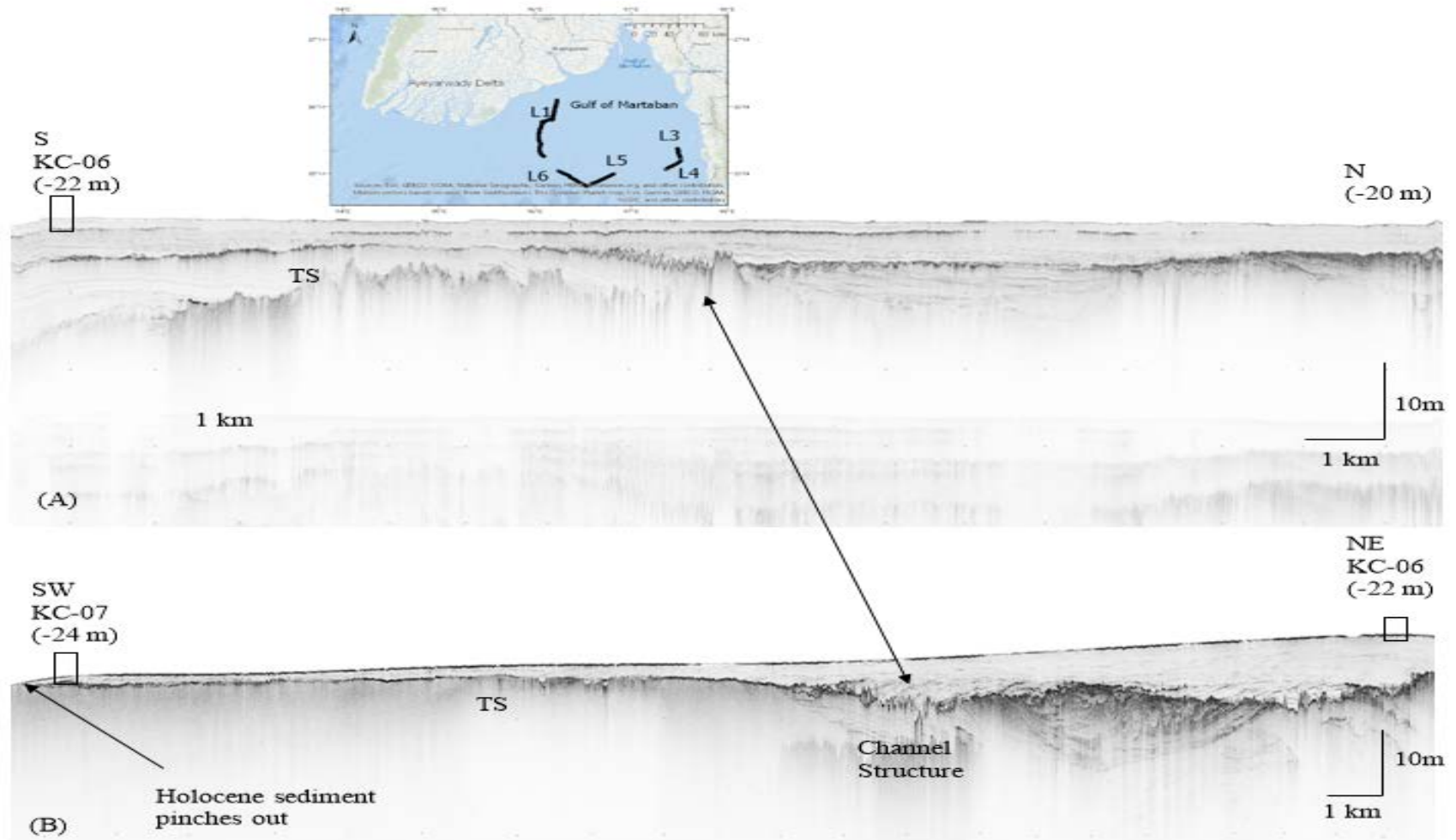


Figure 4.1. Seismic Profile of Line 3(A) and Line 4(B). The prominent acoustic reflector (TS) appears at ~ 30 m water depth in both transects. ~8 m of well stratified, parallel Holocene layers have accumulated overtop the TS and infilled the relict channel structures.

At the SW end of Line 4, the Holocene sediment begins to pinch out, indicating that this might be the southeastern-most extent of which Ayeyarwady derived sediment accumulates.

4.2 Sediment Distribution and Thickness

4.2.1 Gulf of Martaban and Mouths of the Ayeyarwady

In the Gulf of Martaban, seismic profiles reveal highly reflective, well-laminated mud deposits on top of a TS (Figure 4.1, Figure 4.4). The thickness of the mud deposits in the Gulf varies greatly by location, though the average is found to be ~10 m. In the eastern extent of the survey, Holocene sediment appears to pinch out near the ~30 m isobaths, suggesting that this is the furthest southeastern extent of Ayeyarwady derived mud accumulation (Figure 4.1). Acoustic blurring seen in several of the profiles is indicative of the biogenic gas (Figure 4.4). Based on similar subaqueous deltaic clinoforms, the presence of biogenic gas likely comes from decomposing peat deposits below the TS (Alexander et al., 1986; Liu et al., 2005; DeMaster et al 2017). A recent core study in the subaerial portion of the Ayeyarwady Delta found that mangrove peat deposits exist at 28.5 m below sea level (Giosan et al., 2018). Giosan et al, (2018) also carbon-dated the peat deposits to 9,300 cal ybp and concluded that the peat deposits overlay 10,300 years old structure less sands, clayey muds, and weakly laminated channel infills in the Ayeyarwady Delta. The depth of the TS and acoustic blurring of the aforementioned profile (Figure 4.4) strongly agree with this assessment. In addition, the depth of the TS in Line 28 (Figure 4.4) and the dating performed by Giosan et al., (2018) also correspond to the proposed sea-level curve of the Eastern China Sea (ECS). The agreements between these data sets are explored in greater depth in the discussion (section 5.2).

Earlier studies on coral systems in the Andaman Sea have provided evidence that late Pleistocene-Holocene corals existed near the river mouths of the Ayeyarwady and the western coastline but have been subsequently destroyed due to sea-level rise (Panchang, 2008). The seismic profiles in Figure 4.8 and Figure 4.9 reveal a series of hardened coral beds at the same

depth and location previously discussed by Panchang et al., (2008). Hardened coral beds resemble rocky underwater “mountains,” typically formed of limestone over a long period. These coral beds no longer actively support extensive marine life as soft corals do. In contrast, soft corals resemble flower beds and include sea fingers and sea whips, they do not have stony skeletons, and instead, they are supported by wood cores and are protected by their fleshy rind (Panchang et al., 2008). A section of the hardened corals appears to have been covered by Holocene sands, where the topset and foreset of the shore attached clinof orm has accumulated between the -5 m and -20 m water depth (Figure 4.8). The average thickness of the clinof orm is 10 m and appears to have a similar reflectivity as that of the T3 layer in Figure 4.5. The high-resolution imagery did not reveal any bottomset beds, which was to be expected, given the strength of tidal currents around the river mouths. Reflectivity in the profiles continues to decrease seaward, indicating that coarser-grained sediments fall out of suspension in the topset/foreset, while finer-grained sediments remain in suspension, and are restricted from depositing immediately off the mouths (Figure 4.5, Figure 4.6). Kasten cores retrieved seaward of the foreset reveal that the sediment is a mixture of relict sands and mud, consistent with this hypothesis (Figure 4.7; KC-13).

In the Gulf of Martaban, Holocene sediment accumulation rates significantly increase seaward after crossing the 40 m isobath. A distal depocenter has formed between the 30 m and 130 m water depths, where the total thickness of the Holocene sediment accumulation exceeds 60 m. Near the mouths of the Ayeyarwady, Holocene sediment accumulation does not extend beyond the 20 m water depth. The lack of accumulation just off the mouths of the Ayeyarwady is not surprising considering the strength of the tides and currents in this region. The geophysical surveys collected in this area reveal with certainty the locations where Holocene sediment

accumulation terminates, and relict sediment begins (Figure 4.2). By plotting every geophysical profile on a fence diagram, it is quickly apparent the extent to which Holocene sediment accumulates and where it ceases to deposit (Figure 4.3).

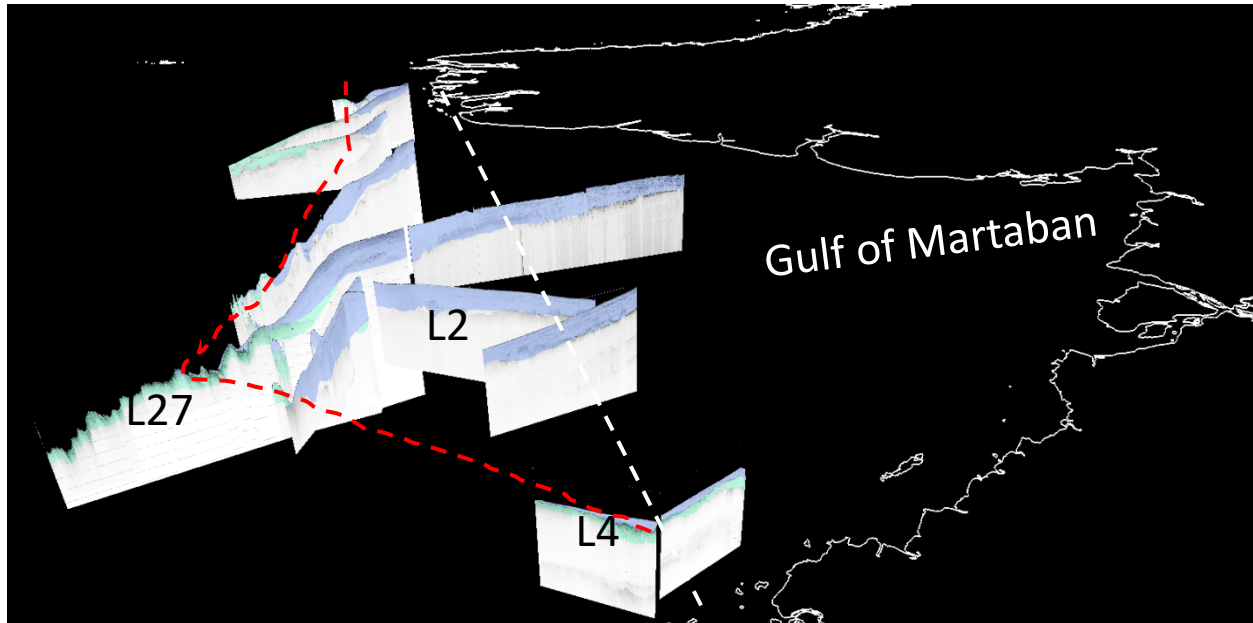


Figure 4.2. Fence diagram of seismic profiles collected in the Gulf of Martaban. The red dashed line indicates the extent of Holocene sediment; the white dashed line indicates the maximum extent of the turbid zone. Purple = Holocene; Green = relict.

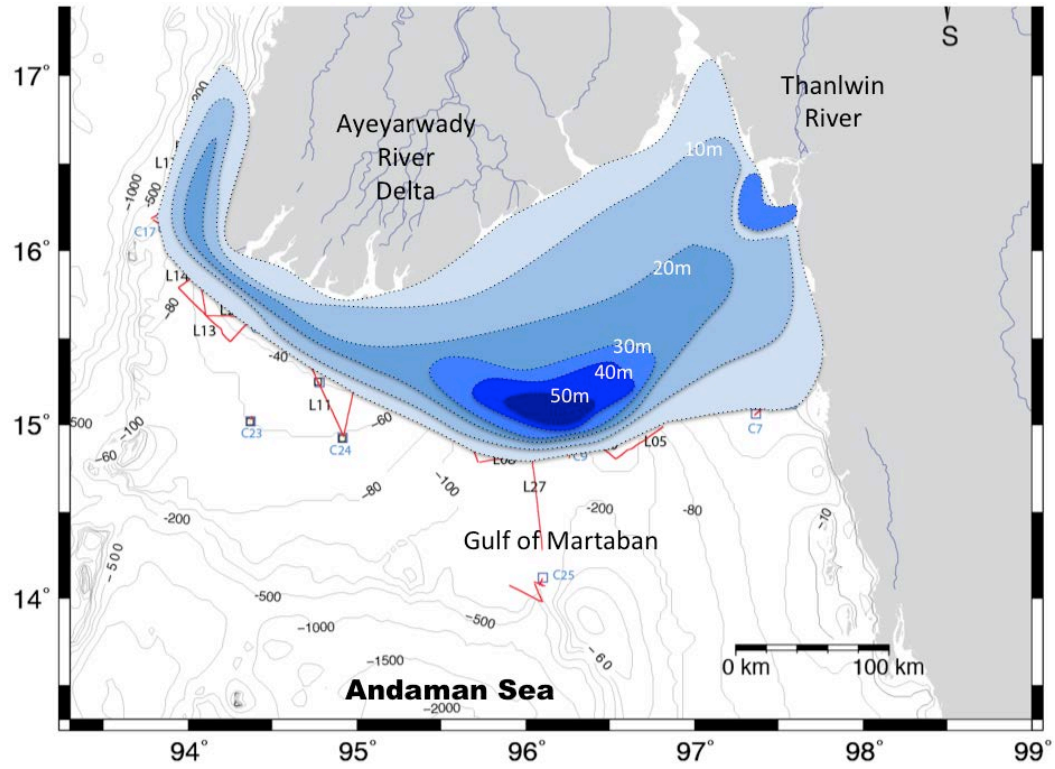


Figure 4.3. A simple Holocene sediment distribution map of the Northern Andaman Sea.

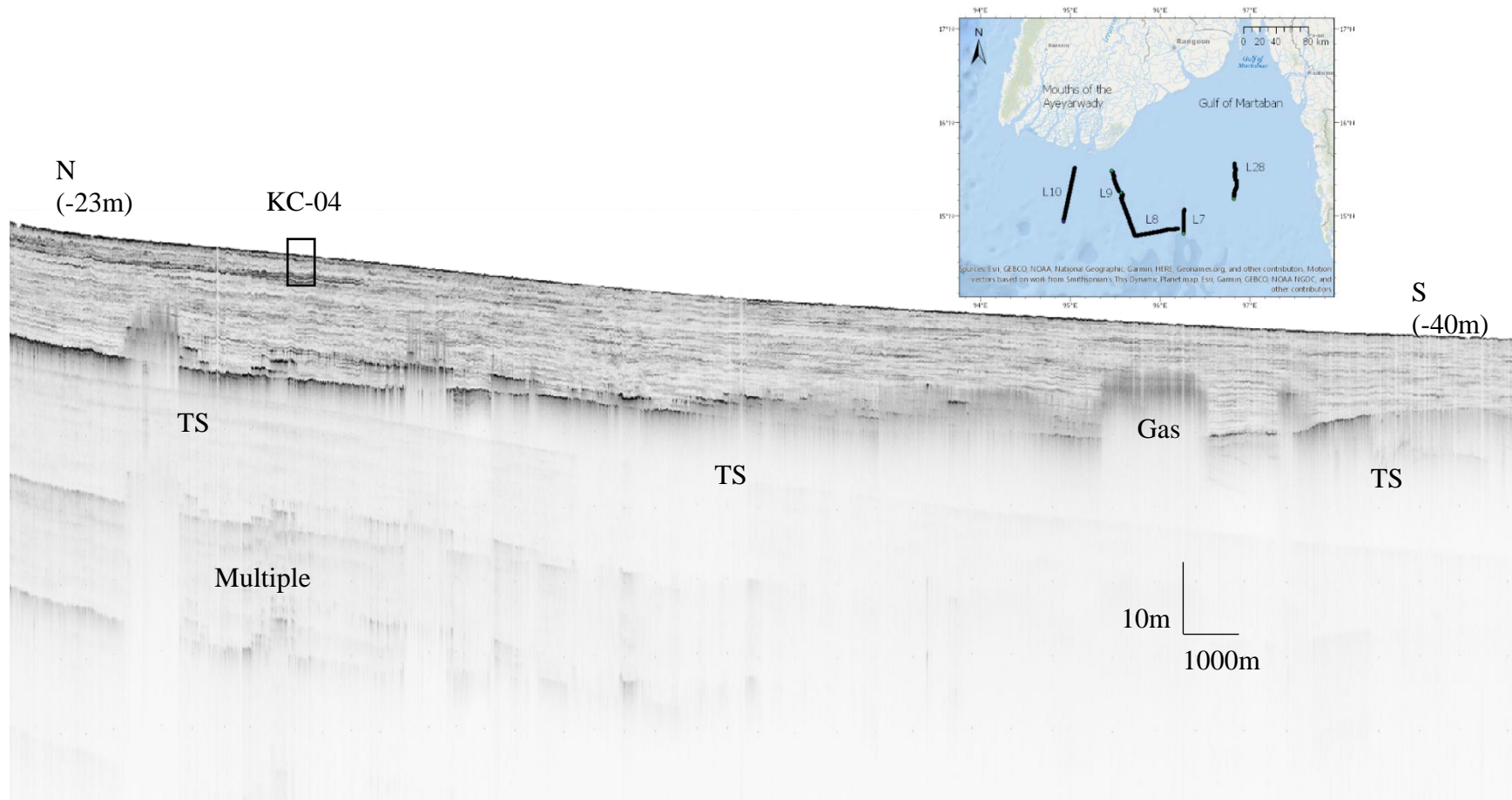


Figure 4.4. Seismic Profile of Line 28 in the Gulf of Martaban. Holocene sediment thickness of < 10 m overlays a highly reflective transgressive surface. Sediment beneath the TS likely consists of med-coarse grained structure less sand. Acoustic blurring in the profile is a product biogenic gas derived from Pleistocene mangrove peat deposits.

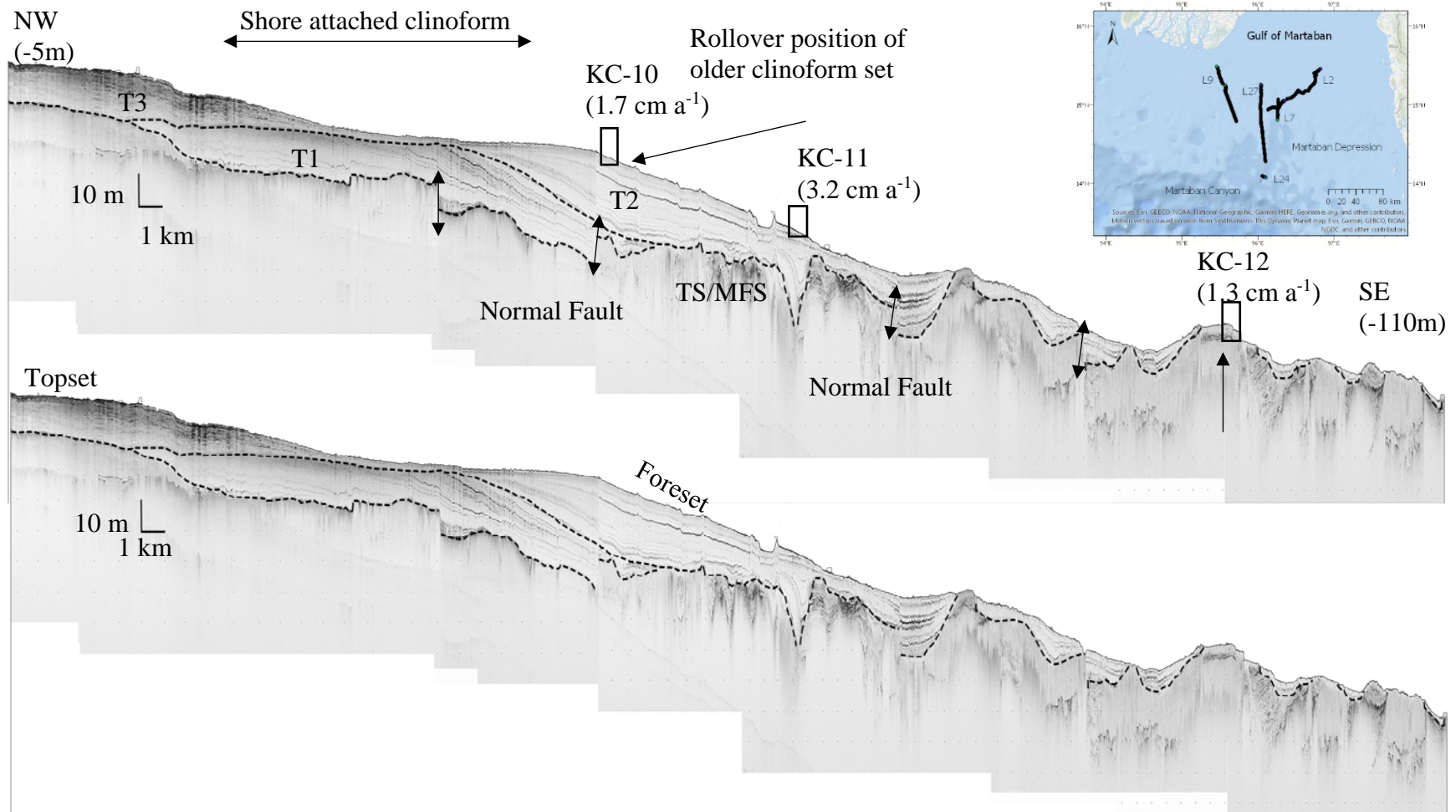


Figure 4.5. Seismic profile of Line 9 located adjacent to the river mouth. This profile reveals the proximal facies of a shore attached clinoform, and the west-most segment of the deeper, compound clinoform. The HST (T1, T2) is separated into two segments, an early Highstand (T1) and a middle Highstand (T2). An MFS separates the HST from the TS. Seaward of the foreset, sediment gradually thins out until normal faults, and relict relief becomes the dominant feature.

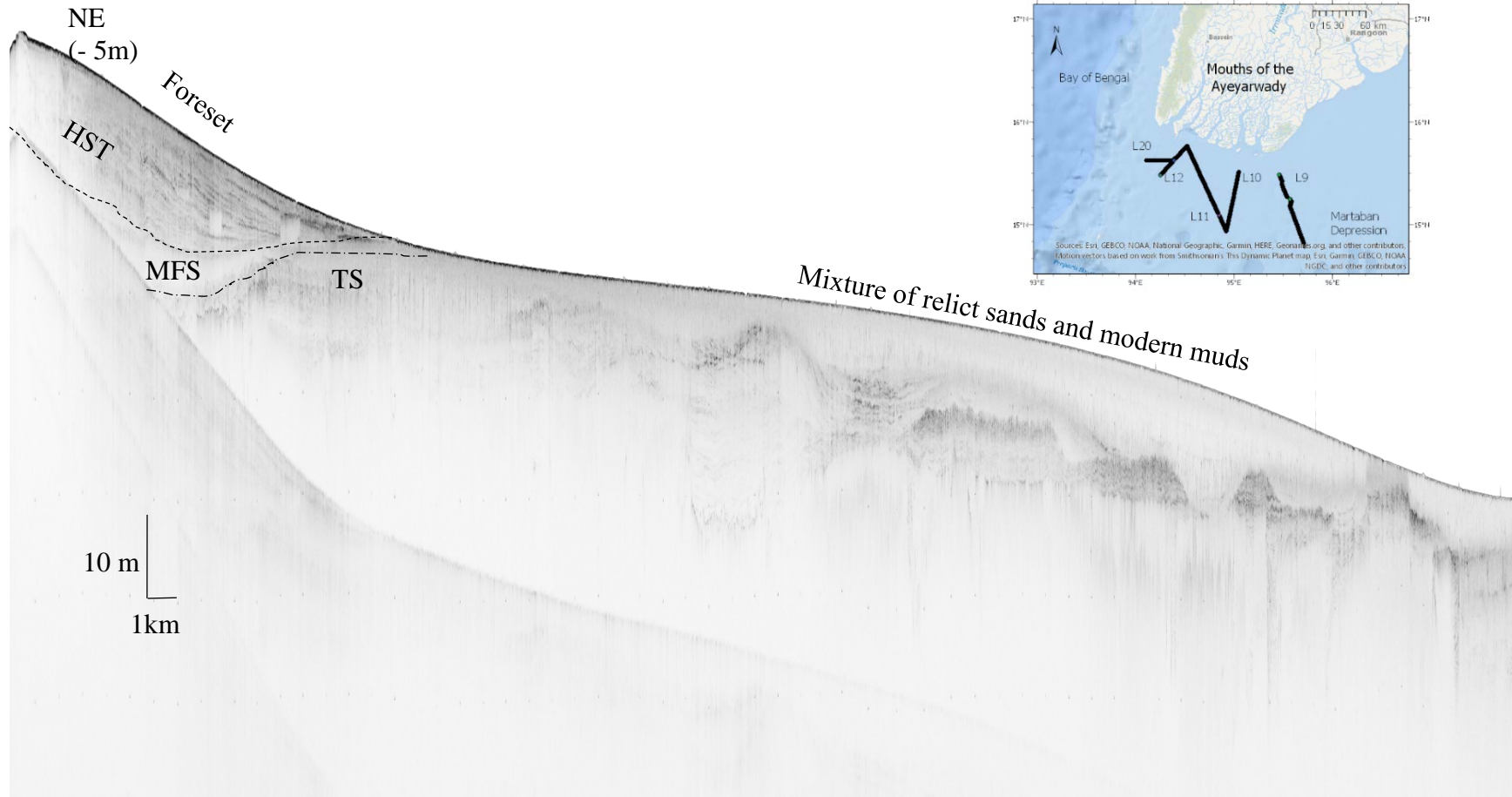


Figure 4.6. Seismic profile of line 10. A continuation of the shore attached clinoform from figure 21. A 10 m thick foreset and no bottomset. An MFS separates the TS from the deltaic deposits. In several locations, the TS has been eroded and replaced by a mix of relict sands and new muds.

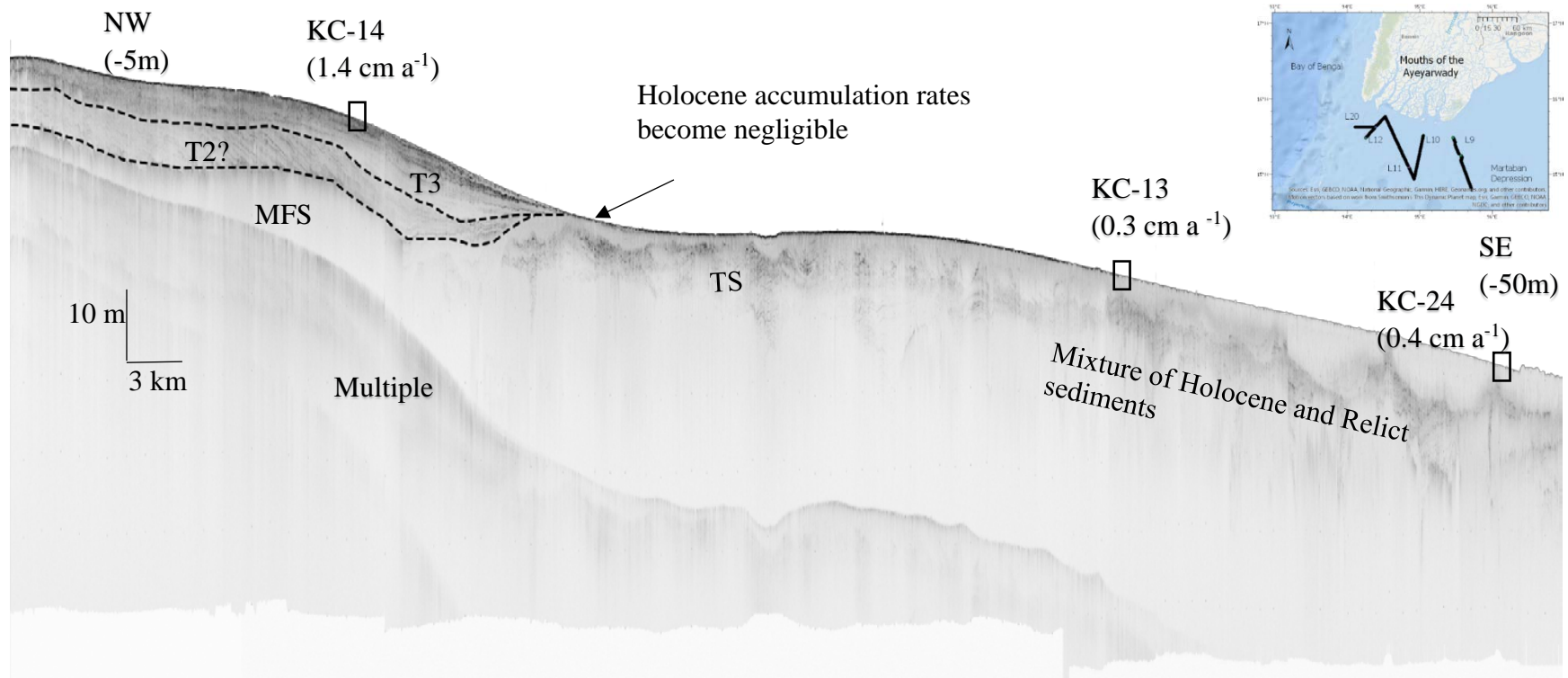


Figure 4.7. Seismic Profile of Line 11 Shore attached clinoform revealing 10 m thick foreset. Due to the erosive nature near the mouths of the Ayeyarwady, bottomset accumulation is negligible. Seaward of 20 m water depth sediment composition is a mix of relict sands and new muds. Kasten cores retrieved in this area yielded a Holocene sediment accumulation rate of $\sim 0.3 \text{ cm a}^{-1}$ (Kuehl et al., 2019). Similar to the other profiles of the shore attached clinoform, the HST is divided into two forestepping units, i.e., T1; T2, and separated by a sub-surface. An MFS separates the HST from the transgressive surface and appears to be truncated at the point at which the foreset stops.

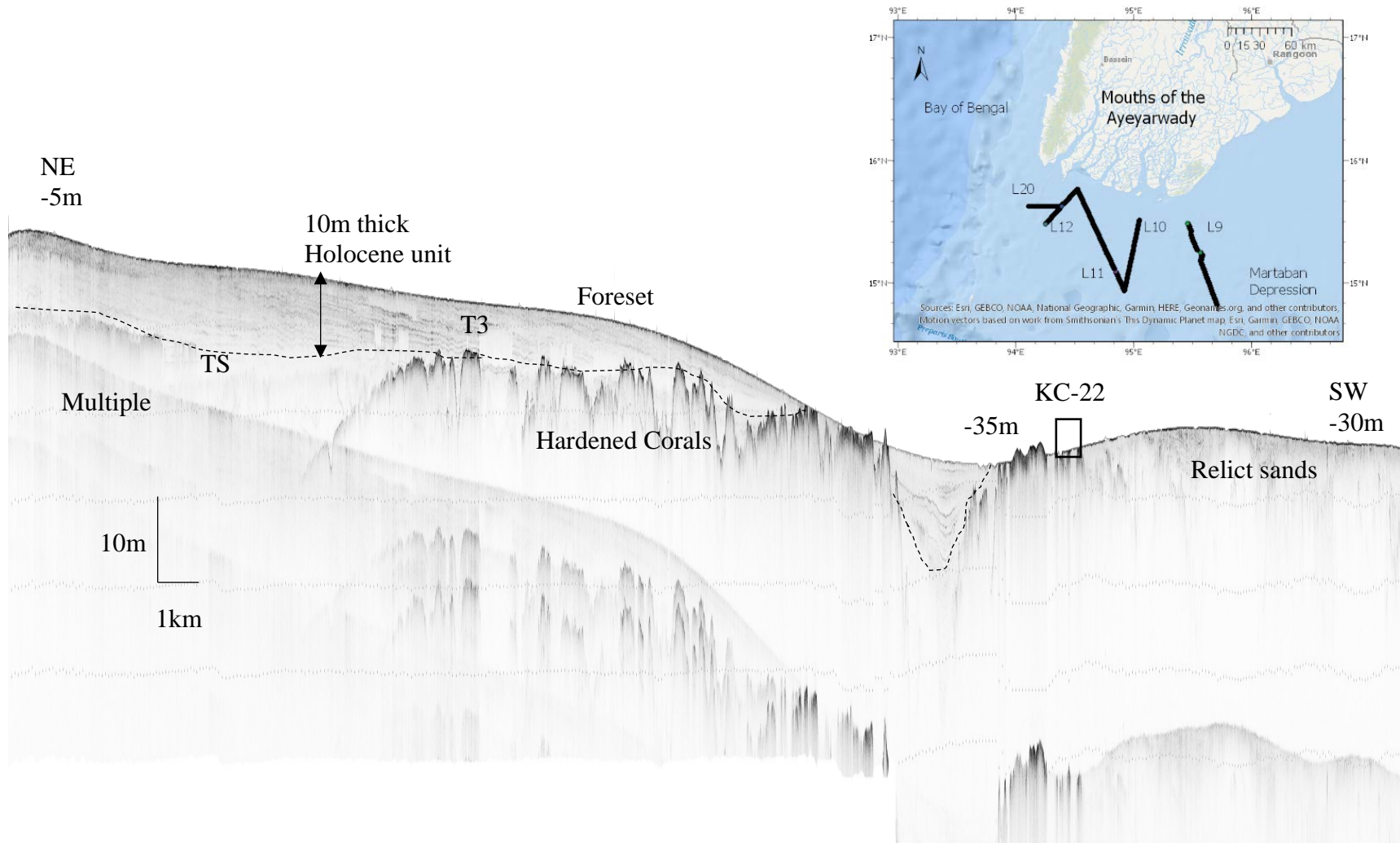


Figure 4.8. Seismic Profile of Line 12. Shore attached clinoform lacking significant structure. A 10 m thick foreset, gently dipping. The foreset exists between the 5 – 30 m water depths. At the -35m water depth, the Holocene sediment pinches out.

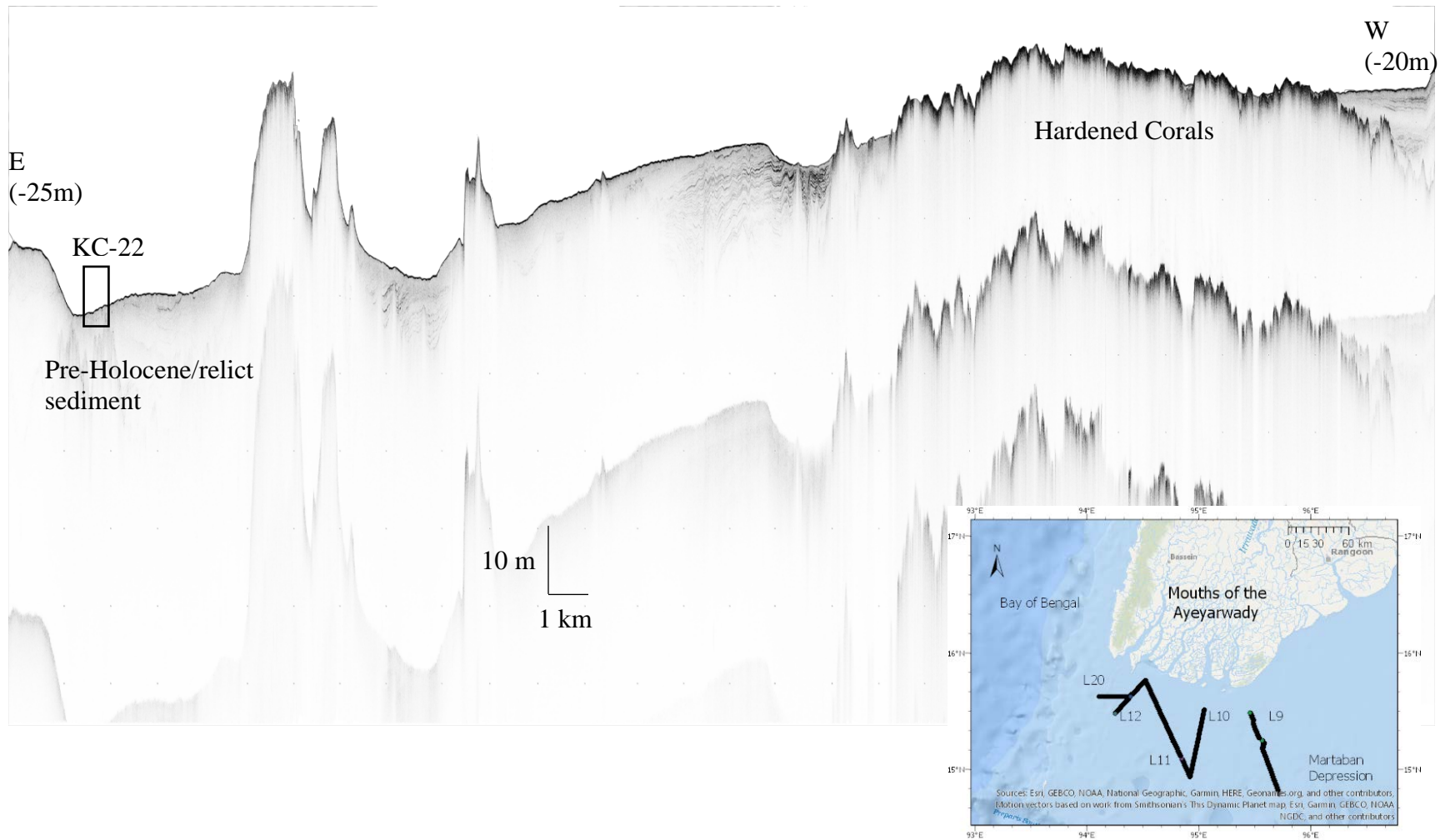


Figure 4.9. Seismic Profile of Line 20: Hardened corals and a mixture of relict sands and modern mud dominate this area directly off the mouths of the Ayeyarwady.

4.2.2 Martaban Depression

Profiles perpendicular to the coastline (north to south) reveal a prominent subaqueous clinoform with gently dipping topset beds, rapidly prograding foreset beds, and heavily eroded, or nonexistent, bottomset beds (Figure 4.11, Figure 4.12, Figure 4.17). The clinoform varies in thickness, 20–60 m in the southeast, and 10–30 m as proximity to the mouths of the Ayeyarwady increases. Profiles in the Martaban Depression reveal a topset that begins at the ~30 m water depth and a thick, steeply dipping foreset that contains a ~60 m thick depocenter and gradually pinches out at depth (Figure 4.12, Figure 4.17).

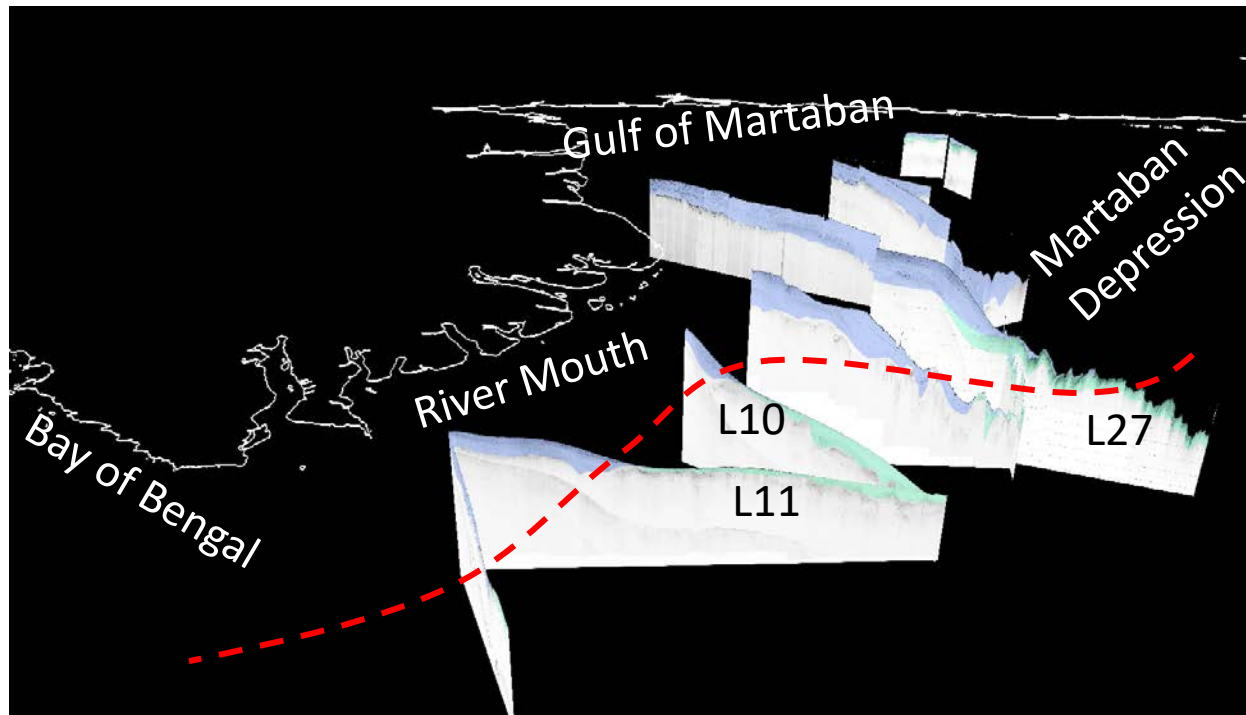


Figure 4.10. Fence diagram of seismic profiles collected in the Martaban Depression and adjacent to the mouths of the Ayeyarwady. The red dashed line indicates the extent of Holocene sediment. Purple = Holocene; Green = relict.

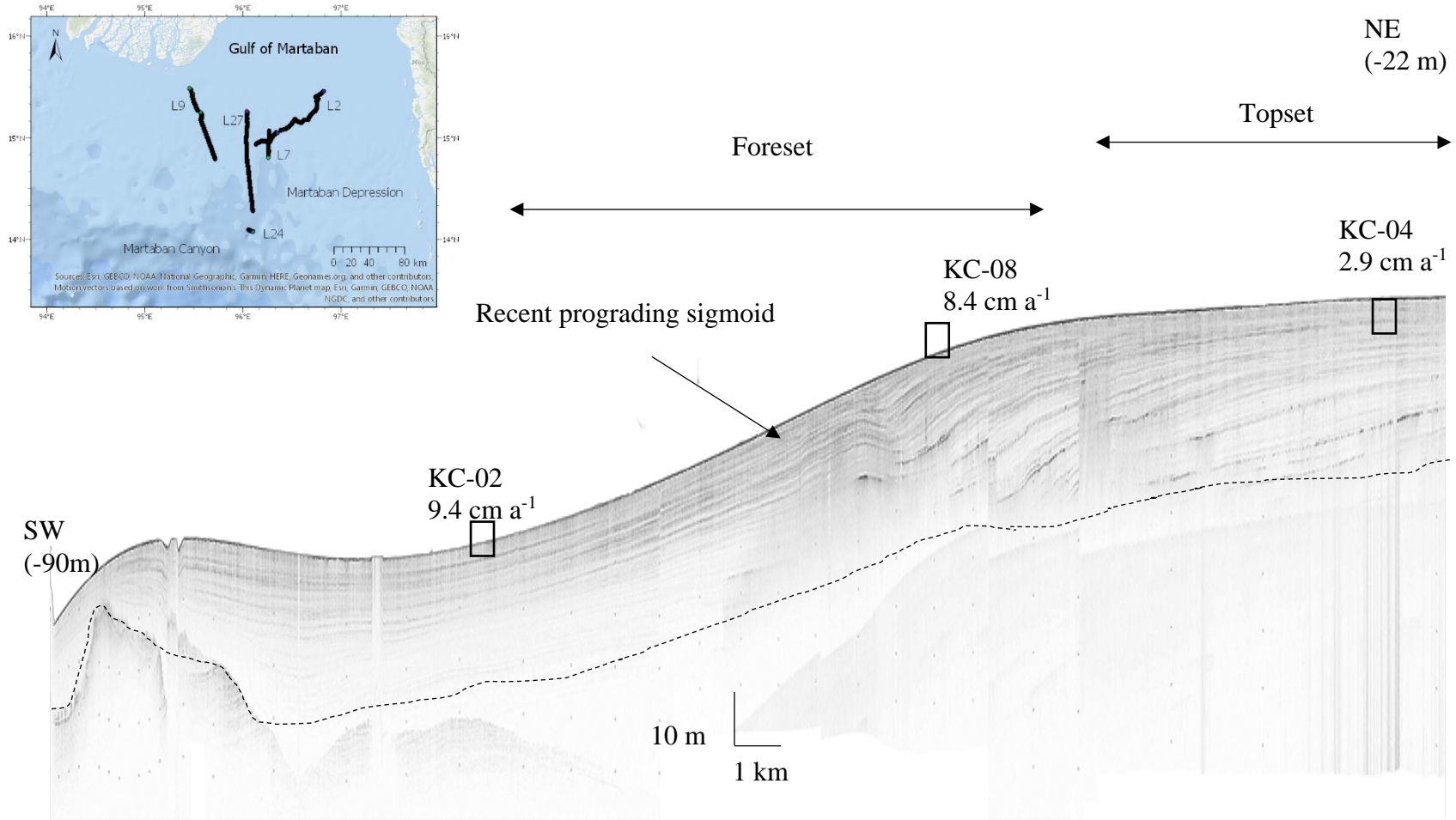


Figure 4.11. Seismic Profile of Line 2 that shows the topset and foreset of a recently prograding sigmoid. This profile is part of the sizable distal depocenter nearing the Martaban Depression. This profile reveals > 50 m of mud accumulation in the foreset and the highest accumulation rates within the study area. Boxes represent the location of Kasten Cores (full index of the location of each Kasten Cores is found in the Appendix).

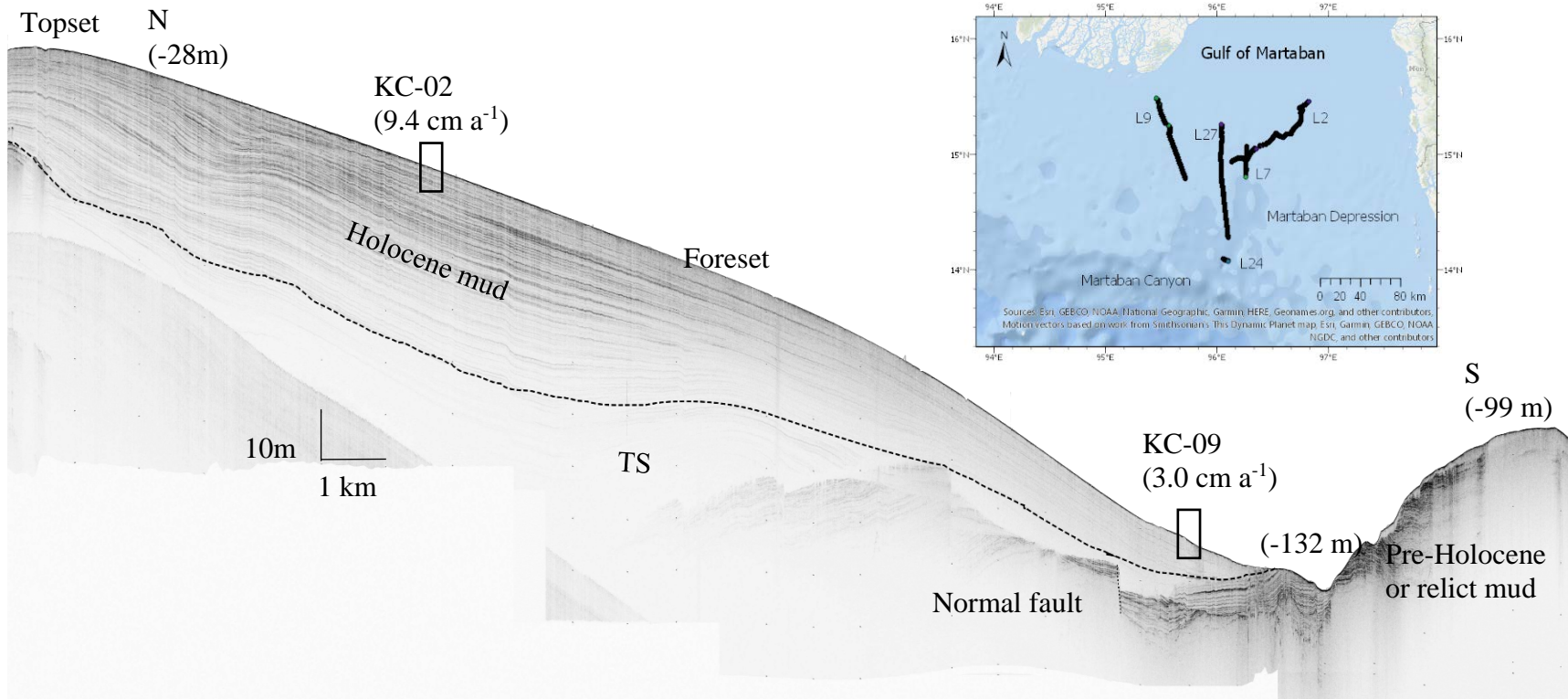


Figure 4.12. Seismic Profile of Line 7 near the transition from the Gulf of Martaban to the Martaban Depression. Accumulation in the foreset ranges from 10-40m with sediment gradually pinching out towards the 132 m water depth. Seaward of the profile, there was no evidence of any sediment accumulation.

4.2.3 Bay of Bengal

There is no evidence of the shore attached clinoform continuing along the Western Rakhine coast. Instead, a mud belt drapes along the shelf and extends to the 150 m shelf break (Figure 4.14, Figure 4.15). The mud belt maintains a constant thickness of ~25 m and increases in accumulation rates northward, away from the mouths. Unlike the deposits in the Martaban Depression, the mud belt does not show any progradation, nor does it pinch out at depth. Instead, it is well stratified and indicates that it has consistently aggraded, supporting the hypothesis put forward by Ramaswamy et al., (2004), Rao et al., (2005), and Kuehl et al., (2019) that a small portion of sediment regularly escapes westward and is transported along the coast, regardless of the seasonally reversing monsoon system. The lack of accumulation at the intersection of Line 19 and Line 20 is likely due to constant sediment resuspension produced by the incoming swell from the Bay of Bengal (Figure 4.13).

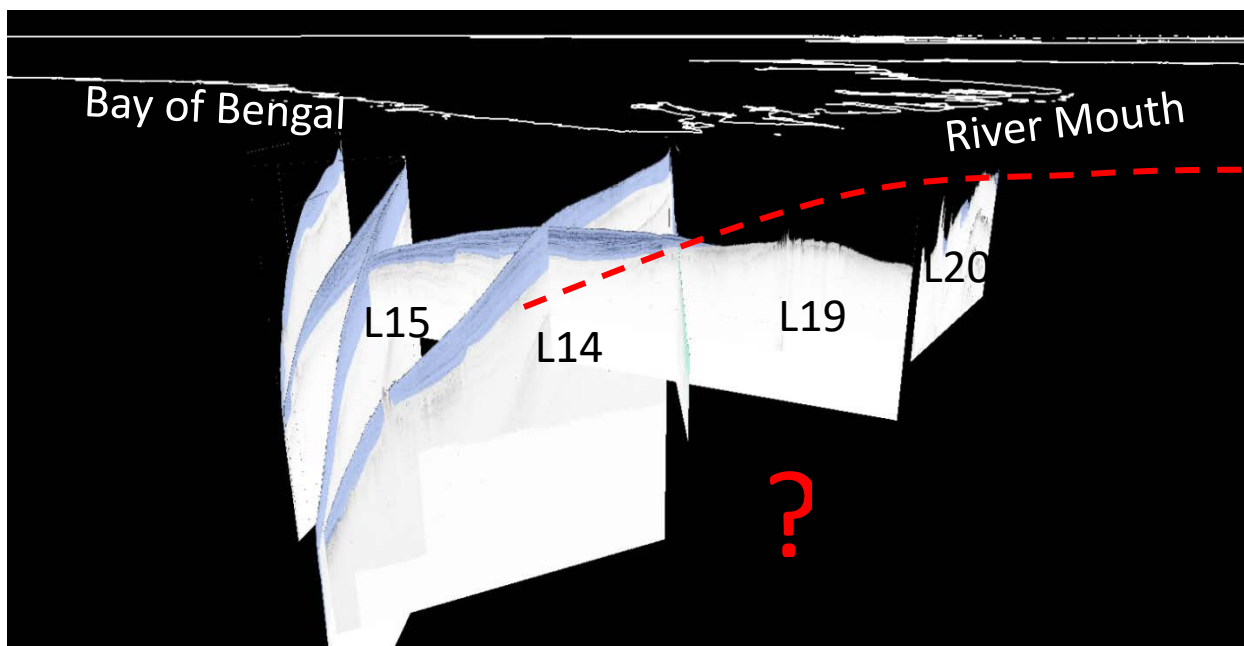


Figure 4.13. Fence diagram of seismic profiles collected in the Bay of Bengal. The red dashed line indicates the extent of Holocene sediment. Purple = Holocene; Green = relict.

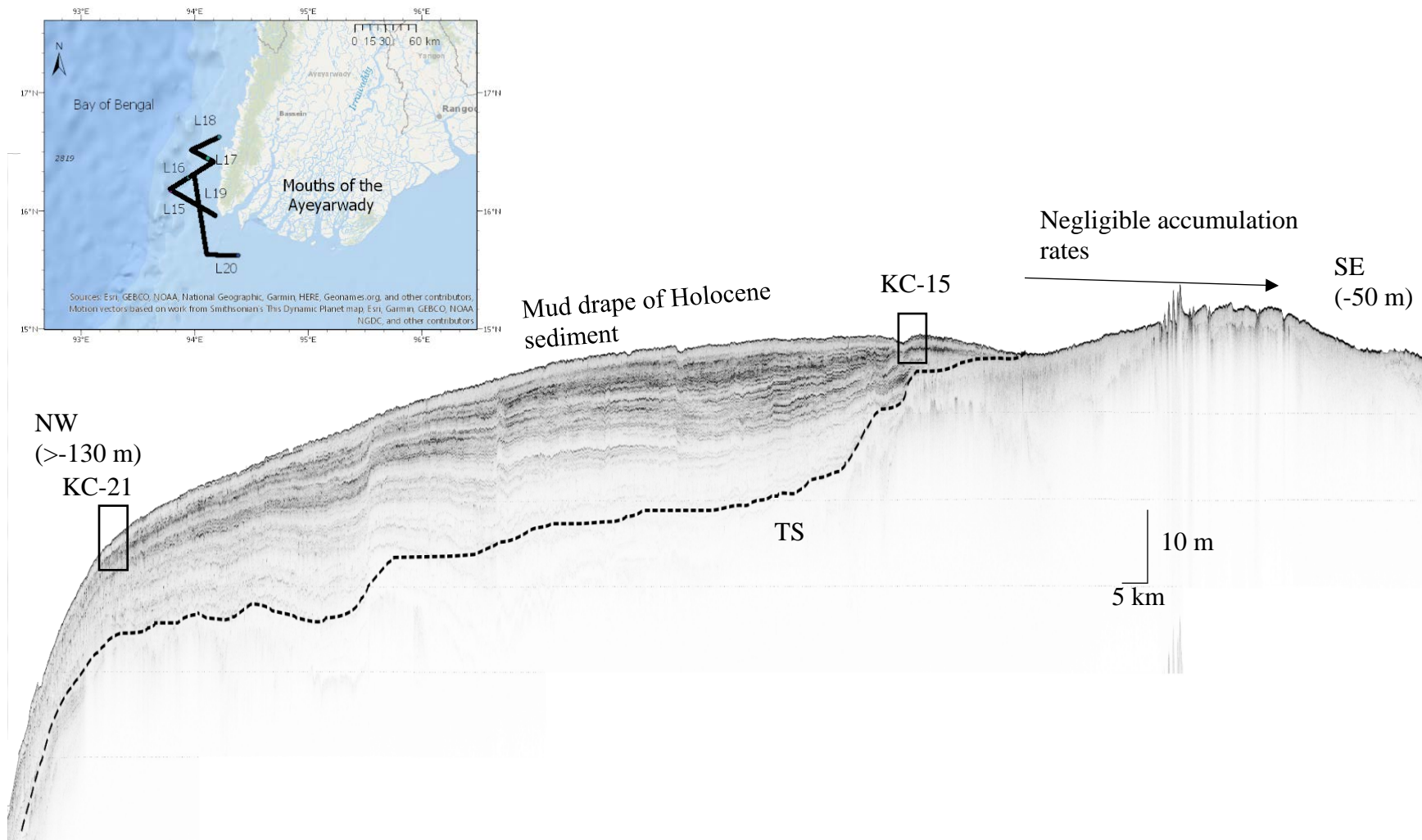


Figure 4.14. Seismic Profile of Line 19 near the Rakhine coastline where mud thickness > 20 m. Accumulation rates become negligible in proximity to the mouths of the Ayeyarwady.

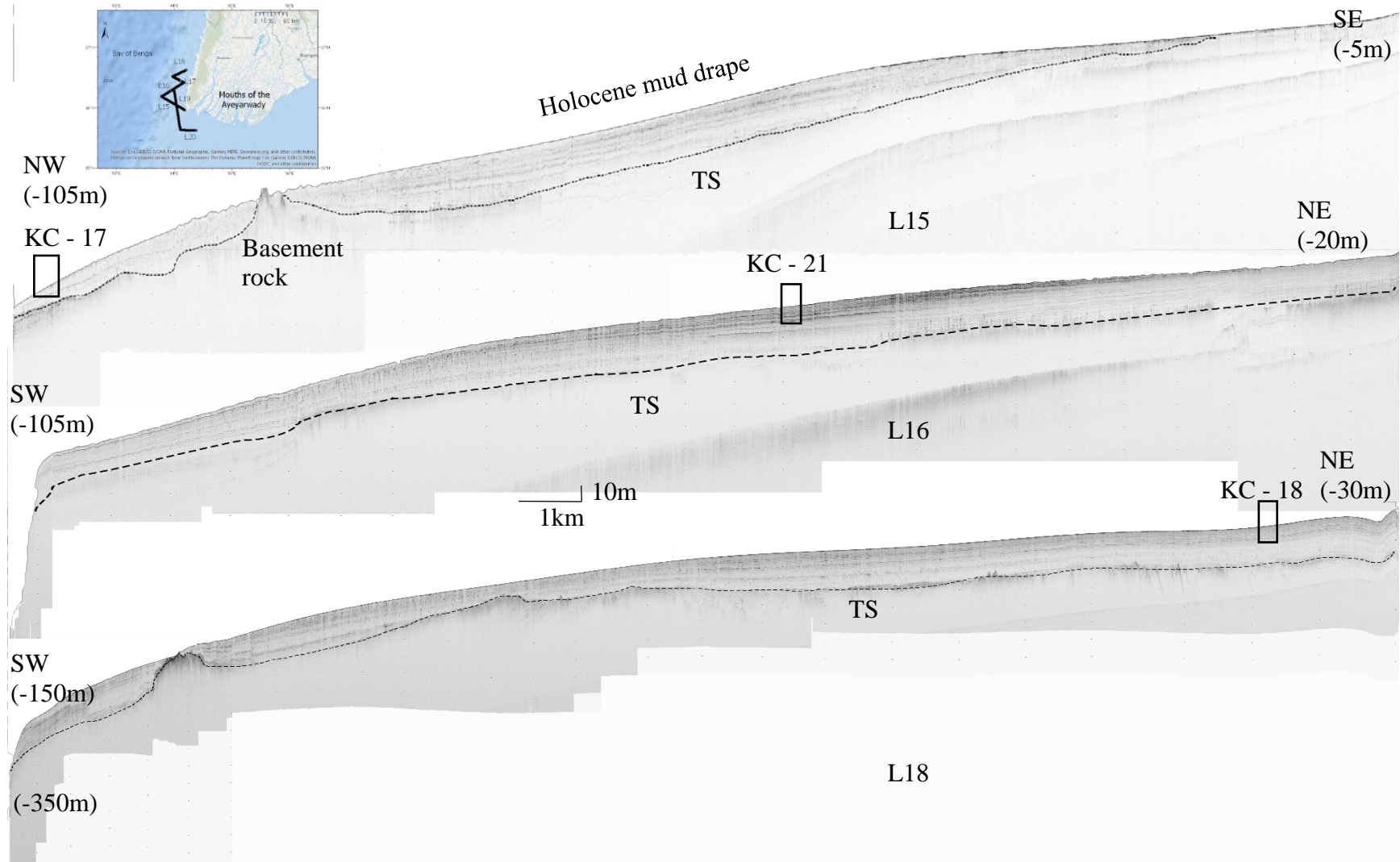


Figure 4.15. Seismic Profile of Line 15, 16, 18 at the most Northern end of our survey in the Bay of Bengal, on the Western Rakhine Coastline. Sediment accumulation stays fairly consistent at ~25 m throughout each transect and gives no evidence to suggest that the sediment does not continue across the trench, into the Bay of Bengal.

4.3 Bookshelf Faulting and Martaban Canyon

Reflectivity in the seismic units increases from the mid-shelf to the outer shelf, illustrating the presence of relict sands and blocky, step-like surface bathymetry indicative of a pull-apart basin associated with the Sagaing fault. Shallow, bookshelf faults, characteristic of an extensional basin, appear in the seismic imagery throughout the Martaban Depression (Figure 4.5, Figure 4.12, Figure 4.17). These fault sets are concentrated between the 90–110 m water depths and do not appear in any of our other transects throughout the study area. The transgressive surface was used as a marker for the measurement of the average vertical offset of the normal faults. The TS in the Martaban Depression exists at ~70 m water depth and displays an average vertical offset of ~7 m (Figure 4.16). Still further seaward, the profiles collected in the Martaban Canyon do not reveal any Holocene sediment accumulation. A gravity core was attempted at the Martaban Canyon head (Figure 4.18); however, nothing was retrieved, likely due to the sandy composition. The profiles reveal a V-shaped canyon head with depths exceeding 300 m, with banks occurring at 150 m. There was no evidence of Holocene sediment accumulation or progradation on, or into the canyon head nor along the banks or the surrounding shelf.

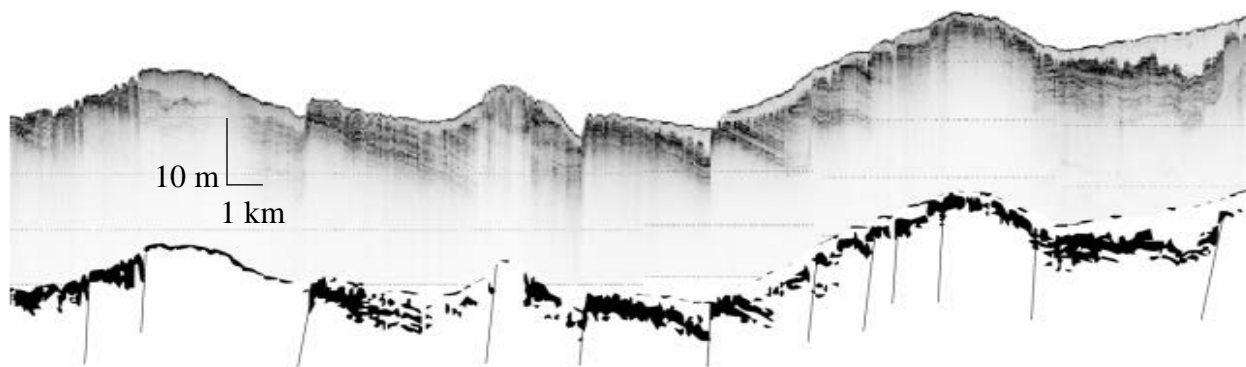


Figure 4.16. Close-up of the bookshelf faulting in Line 27.

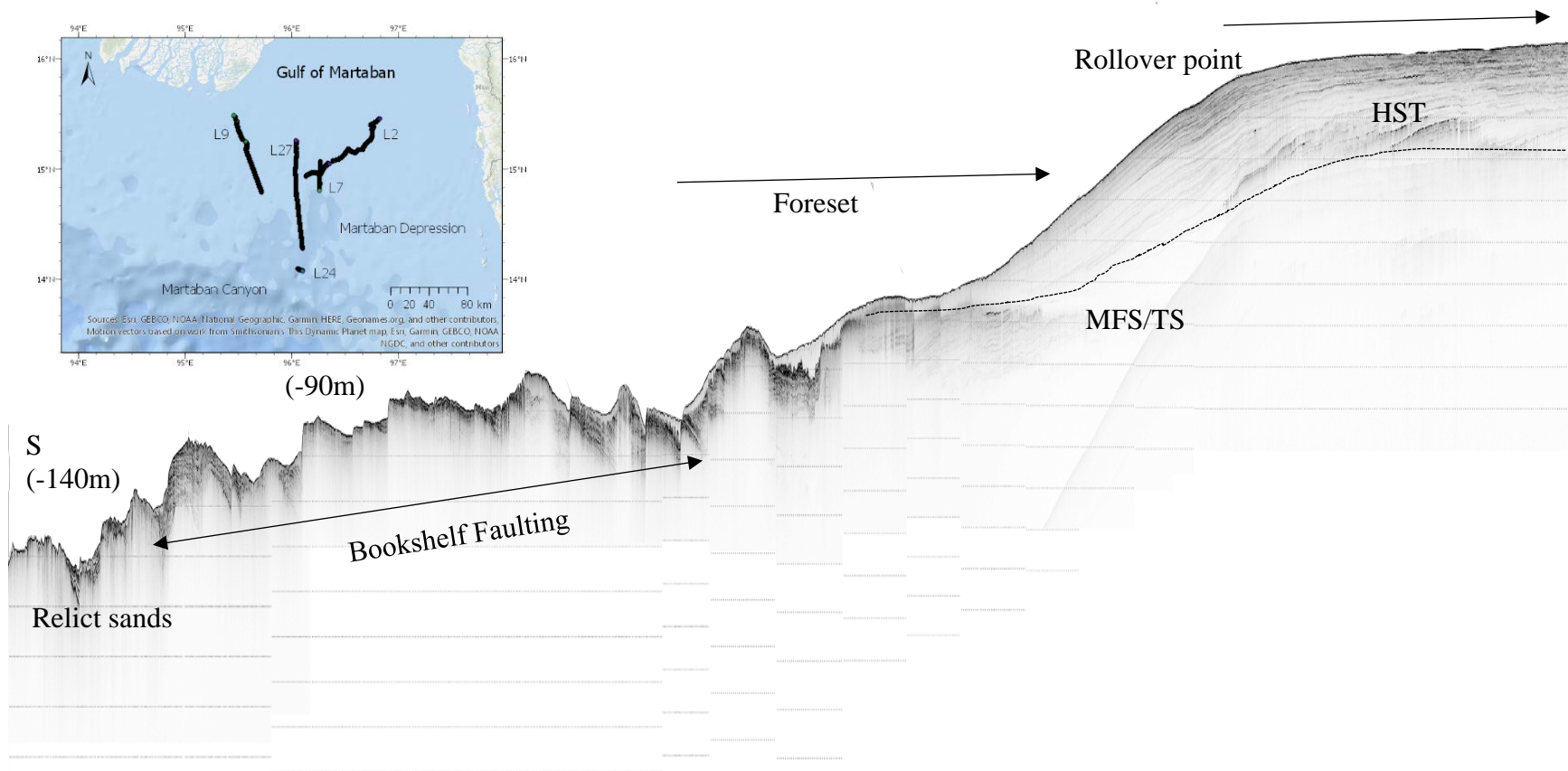


Figure 4.17. Seismic Profile of Line 27 located in the Martaban Depression. This profile reveals a thick foreset bed of the clinoform with no bottomset, indicative of the erosive nature of the Andaman. Beneath HST is the TS that represents the base of the postglacial transgressive surface. Underneath the TS are the pre-Holocene units and relict sands.

Holocene sediment appears to gradually thin at (-90 m) water depth, until it pinches out completely, where the predominant features are back-arc basin bookshelf faults.

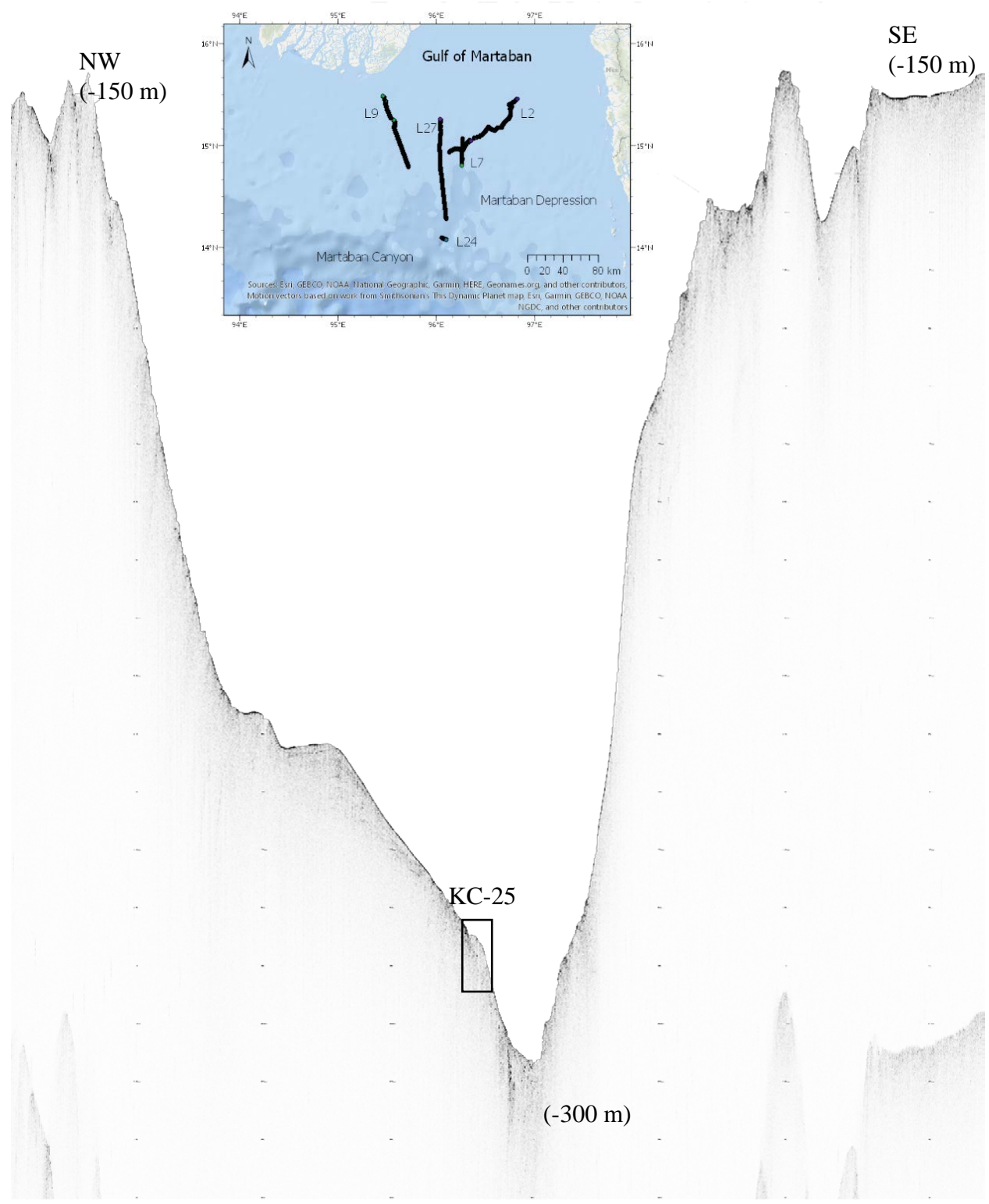


Figure 4.18. Seismic profile of Line 24 in the Martaban Canyon head. There is no evidence of Holocene sediment accumulation on the floor of the canyon nor along the banks.

4.4 InSAR Subsidence and Uplift Mapping

The processed SAR imagery collected between January 2016–January 2020 revealed that the Ayeyarwady Delta is experiencing an average of 15 mm a^{-1} , and up to 25 mm a^{-1} , of uplift or aggradation along the mouths eastward of one of the three main distributaries, the Ayeyarwady. The results indicate that the mouths westward of the Pyamalaw distributary are subsiding at an average rate of 10 mm a^{-1} , with accelerations up to 25 mm a^{-1} . The area proximal to the To-Thakutpin has remained mainly at equilibrium, reporting a maximum uplift rate of 10 mm a^{-1} , but a mean of just 1 mm a^{-1} . The coast eastwards of the Yangon River show a much higher uplift rate than the portion between the To-Thakutpin and the Yangon, $\sim 10\text{--}20 \text{ mm a}^{-1}$. Between the Ayeyarwady and Pyamalaw distributaries (Figure 4.19), the displaced land seems to be aggrading on the back end and subsiding on the seaward portion of the mouth. In contrast, the area north of the mouths appears to be subsiding by up to 66 mm a^{-1} .

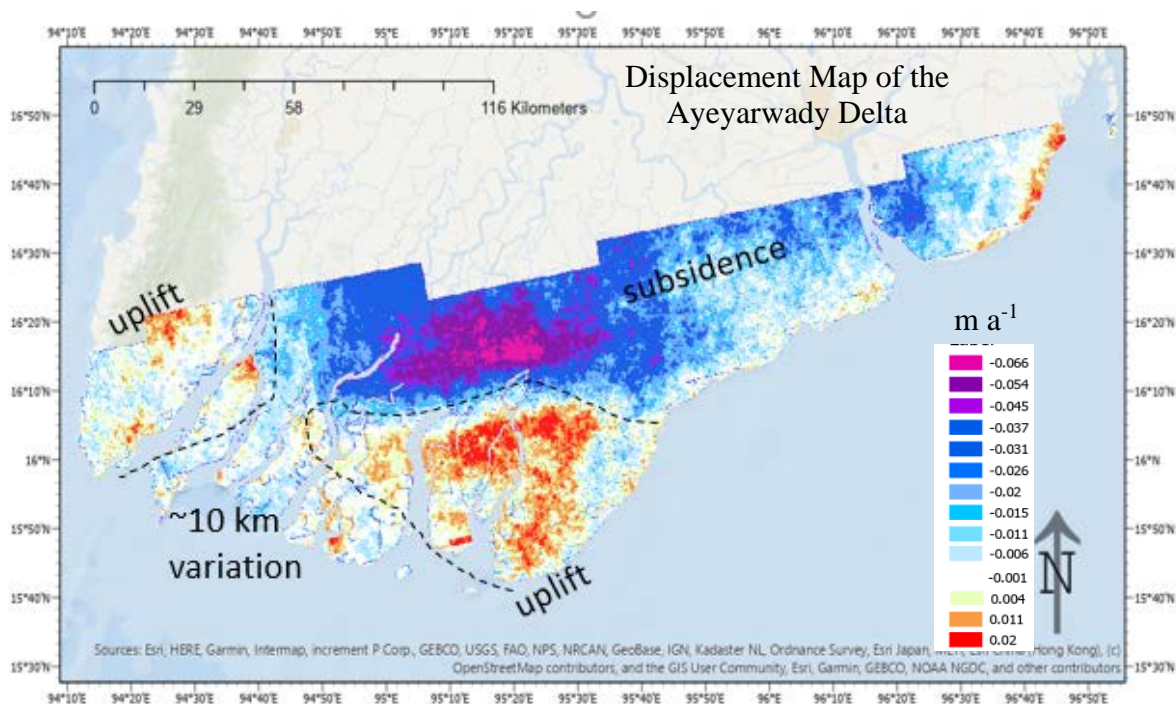


Figure 4.19. S1A InSAR displacement results averaged over 4 years (2016-2020) to provide an annual rate of displacement. A Boolean operator was used to exclude pixels with a coherence of less than 0.15. Warm colors represent uplift/aggradation and cool colors represent subsidence. The main distributaries of the Ayeyarwady River are identified.

Of the study area imaged, only 25% of the delta appears to be uplifting or aggrading, 10% has maintained homeostasis, and the remaining 65% is subsiding (Figure 4.20). The spatially averaged mean annual displacement across the delta is $-1.3 \pm 2.5/-6.0$ cm.

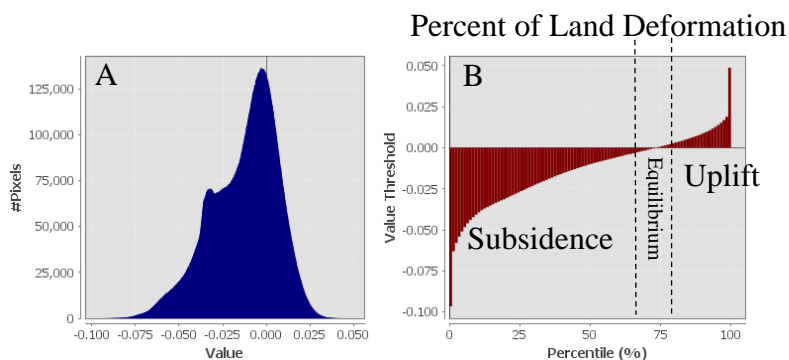


Figure 4.20. (A) Histogram statistics of the deformation dataset. From the figure, the majority of pixels fell between the $-0.06: 0.025$ bins. (B) Percent of land deformation. The majority of the delta, 65%, is subsiding. Meanwhile only 10% of the delta is currently at equilibrium and the remaining 25% experiences uplift or aggradation annually.

Chapter 5: Discussion

This section discusses the sediment distribution patterns, driving forces, and the tectonic role of distributing sediment, while also providing a brief comparison to other deltas.

5.1 Oceanographic controls on sediment thickness and distribution

Major tide-dominated rivers such as the Ganges-Brahmaputra, Fly, Indus, and Ayeyarwady, export most of their sediment to the shelf, where it is then subjected to a variety of marine processes (Walsh et al., 2009). Sediment dispersal and the development of subaqueous clinofolds are controlled by processes such as waves, tides, and geostrophic currents, but these processes have an even more significant effect when they coincide with high river discharge (Goodbred et al., 2011). The Gulf of Martaban is considered one of the world's largest perennially turbid zones, covering an area of over 45,000 km²; however, this area varies significantly as it oscillates with the spring and neap tidal cycles. Patches of relatively less turbid water within the highly turbid zone were observed by Ramaswamy et al., 2004, and again in Google Earth imagery collected from December 2011. The geophysical profiles and Kasten cores collected in the study area agree with the previous observation by Ramaswamy et al., 2004. Over the last decade, the areal footprint of the less turbid patch has varied, yet imagery suggests that it remains a consistent feature (Figure 5.1). It has been suggested that this phenomenon can result from the intrusion of clear offshore waters that lead to the rapid settling of suspended sediments, thus creating a patch of less turbid water in an otherwise highly turbid zone (Ramaswamy et al., 2004). It has also been suggested that the rapid settling of suspended sediment may result from a decrease in tidal currents; however, there is no evidence to suggest that the tidal currents in the Gulf of Martaban vary sufficiently enough to allow for rapid sedimentation.

One of the primary distributaries of the Ayeyarwady delta is the To-Thakutpin River (Figure 5.1). It is possible that an increase in freshwater discharge from this distributary would encourage rapid sedimentation locally and yield a patch of less turbid water in a highly turbid zone. In this study, sediment accumulation rates measured from Kasten cores collected near the patch of less turbid water are over three times more rapid than those collected further away. The data from the cores collected near to the patch of less turbid water reveals this is a consistent feature in the Gulf of Martaban and that the sediment accumulation rates recorded in this study agree with the turbid front gradient and SSC profile proposed by Ramaswamy et al., (2004) (Figure 5.2).

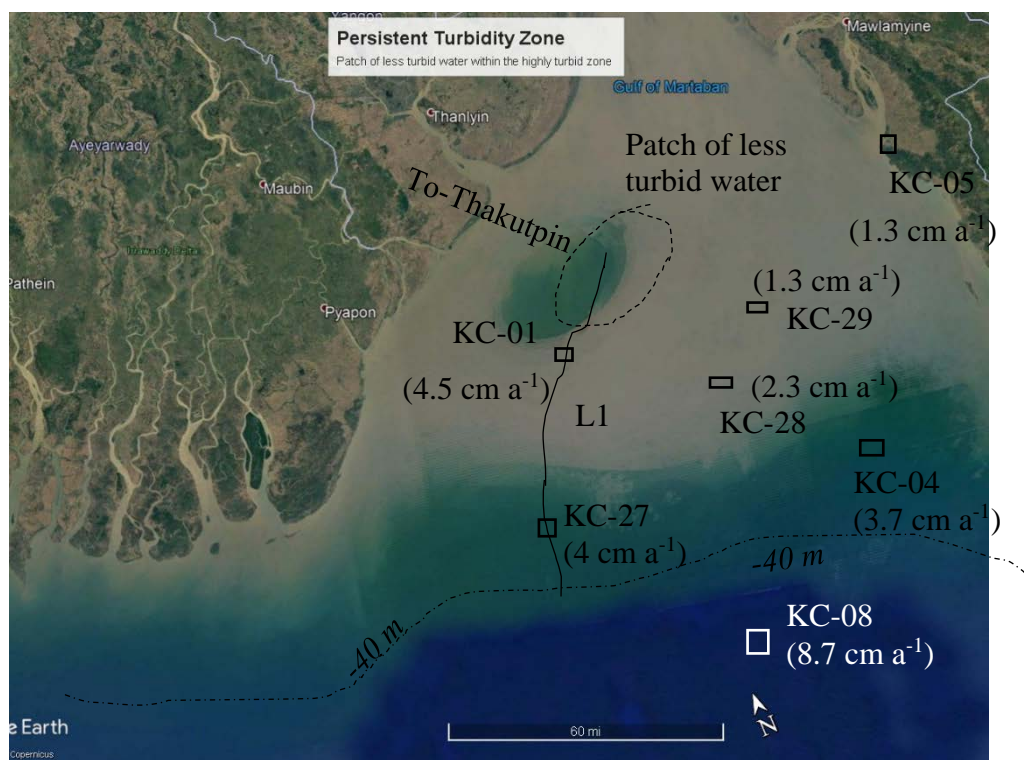


Figure 5.1. Highly turbid area with a patch of less turbid water. L1 = Line 1; KC-01 – Kasten Core 1. Sediment accumulation rates were calculated from excess ²¹⁰Pb geochronologies (Kuehl et al., 2019).

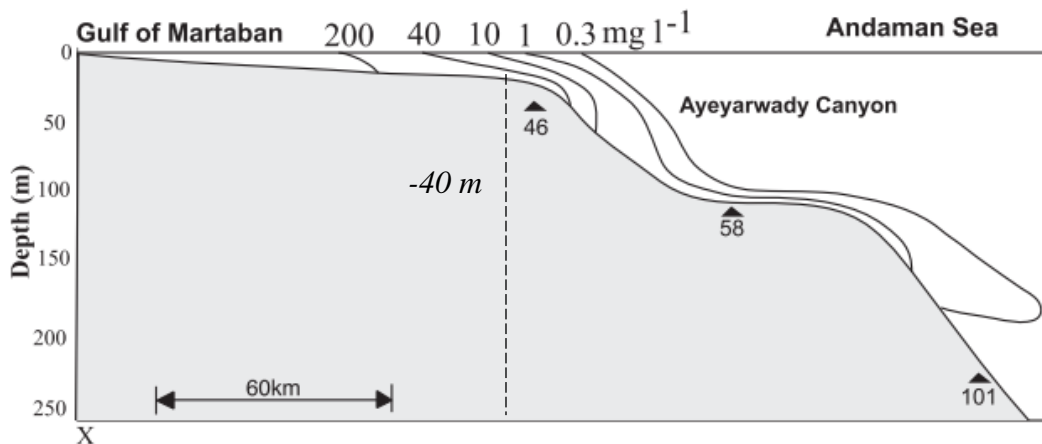


Figure 5.2. SSC profile across the Ayeyarwady shelf. As SSC decreases, so too does turbid water energy (Modified from Ramaswamy et al., 2004).

Due to strong tidal currents, seasonally reversing monsoon systems, and shallow bathymetry, the Gulf of Martaban acts as a highly efficient sediment trap (Ramaswamy et al., 2004; Rao et al., 2005; Kuehl et al., 2019). Winds directed offshore during the NE monsoon allow the turbid water zone to reach its maximum footprint, while winds directed towards the shore during the SW monsoon greatly reduce the footprint of the turbid zone and pull the waters closer to shore (Liu et al., 2020). In doing so, the seasonal changes in tidal amplitude allow the turbid front to migrate, periodically releasing nearshore sediment to the foresets, where the turbid zone begins to lose energy around the 40 m isobaths. As observed from the sediment accumulation rates provided by Kuehl et al. (2019), after surpassing the 40 m isobaths, rapid sedimentation occurs (Figure 5.3).

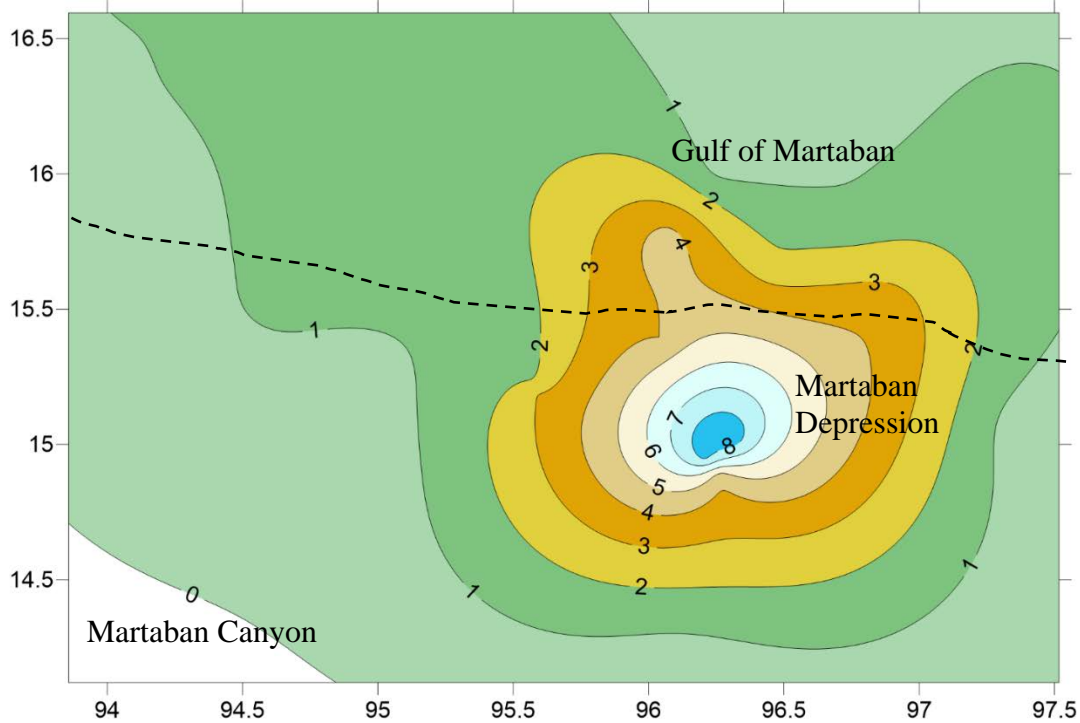


Figure 5.3. Sediment accumulation rate isopach. This reveals that the maximum footprint of the turbidity front reaches the ~40 m isobath, and the water becomes less turbid seaward of the 40 m isobath as the material begins to rapidly fall out of suspension. Accumulation rates reported by Kuehl et al., 2019.

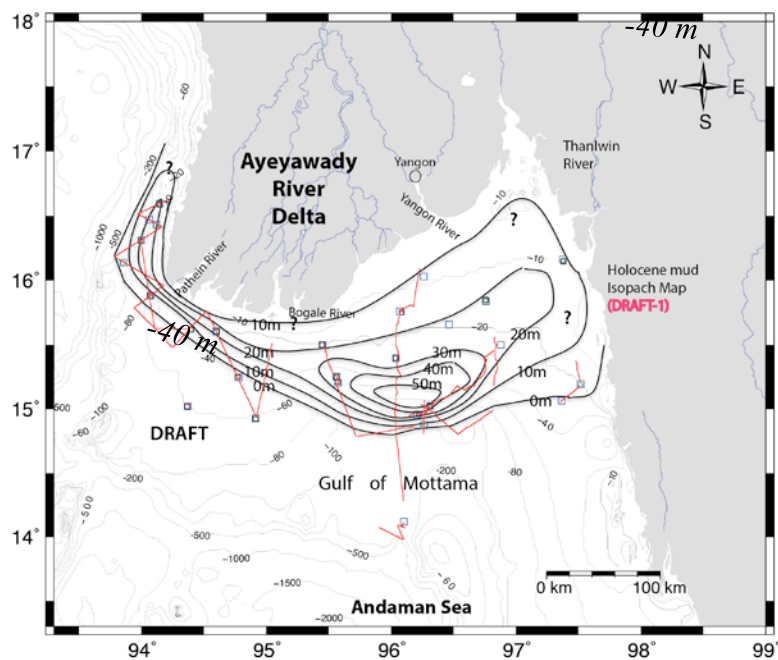


Figure 5.4. Isopach map of layer thickness based off seismic profiles reported in Table 1.

Seaward of the 40 m isobaths, the seismic profiles reveal a large, distal depocenter that is up to 60 m thick and extends to the outer shelf, around the 130 m water depth (Figure 4.2, Figure 4.12, Figure 4.17). South of 14.5° N latitude, sediment accumulation quickly diminishes, where, predominately, the features are rugged surfaces with blocky, bookshelf faulting, indicative of the extensional basin that the Northern Andaman Sea resides in (Figure 4.17). Geophysical profiles collected across the 500 m deep Martaban Canyon reveal that no modern sediment has accumulated or prograded to the canyon floor or along its banks at 150 m water depth. This observation contrasts with Ramaswamy et al., (2014), who suggested the canyon is a mechanism for off-shelf transport of sediment to the deep Andaman Sea. Of course, since seismic profiles were not collected in the deep Andaman Sea, it is still possible that sediment is accumulating therein, or is transported as a bottom current.

The mud drape extending along the western coast of Myanmar does not show any signs of cross-shelf progradation (Figure 4.15). Kasten cores collected here reveal that the sediment is composed of dense layers of fine-grained, sandy silts and clays that are consistent with other Ayeyarwady derived Holocene samples (KC-15, KC-17, KC-18, KC-21; Kuehl et al., 2019). A sediment coloration change was reported by Kuehl et al., (2019), suggesting that the mud drape is accumulating some percentage of sediment input from a source other than the Ayeyarwady, likely from smaller rivers discharging from the Indo-Burman range.

The total sediment budget for the Andaman Basin was calculated using ArcGIS 10.6 to determine the total area of the subaqueous delta ($> 60,000 \text{ km}^2$) and then multiplying by the maximum thickness of sediment layers from the geophysical profiles in each of the main areas: Western Myanmar Shelf, Mouths of the Ayeyarwady, and the Gulf of Martaban, which yielded a total volume of $1,075 \text{ km}^3 \pm 10\%$ (Table 1). The mass was determined by multiplying the

average dry bulk density of the sediment, 1.2 g cm^{-3} , by total volume, equating to 1,290 billion tons. After dividing by the time since sea level stabilized close to the modern levels ($\sim 7,000$ years), the total flux of sediment to the Ayeyarwady subaqueous delta was 215 MT a^{-1} . Of this total, 20 MT a^{-1} (10%) accumulates near the mouths, 180 MT a^{-1} (83%) in the Gulf of Martaban, and 15 MT a^{-1} (7%) along the western Myanmar Shelf (Liu et al., 2020) (Table 1). Although this estimation does not include any additional input from smaller mountainous rivers discharging from the Rakhine coast, it still appears consistent with the rates reported from surface sample measurements by Rao et al., (2005).

Table 1. Summary of the Modern Ayeyarwady and Thanlwin subaqueous delta characteristics based off geophysical profiles. (Liu et al., 2020).

	Western Myanmar Shelf	Shelf off the Ayeyarwady River mouths	Gulf of Martaban	Total
Mud cover area (km^2)	5,000	10,000	45,000	60,000
Maximum water depth (m)	>300	30	130	
Maximum thickness (m)	20	15	60	
^{210}Pb -derived accumulation rates (cm/yr)	0.3-1.0	0.4-1.4	0.3-9.4	
Estimated volume ($\times 10^9 \text{ m}^3$)	75	100	900	1075
Estimated mass ($\times 10^9 \text{ ton}$)	90	120	1080	1290
Annual flux (Mt/yr)	15 (7%)	20 (10%)	180 (83%)	215

For deltaic systems such as the Yellow, Yangtze, and Mekong, the majority of sediment reaching the coast is only deposited near the river mouths temporarily (10-20%), while approximately 30-40% exhibits unidirectional, alongshore transport that extends 300-800 km

from the river mouth (Figure 5.5; Liu et al., 2009; Liu et al., 2020). In contrast, the Ayeyarwady River sedimentary system is highly effective at dispersing sediment due to a bi-directional tidal transport under the SW and NE monsoon systems (Kuehl et al., 2019). This unique process has created an environment in which only five percent of the total sediment yield accumulates nearest the mouths, while 41% is transported alongshore (~200 km), into the distal depocenter of the Martaban Depression. The remaining four percent escapes westwards, into the Bay of Bengal, and is transported up the Rakhine coast, eventually accumulating as part of the 25 m thick mud drape. The remaining 50% of sediment remains in the delta plain (Figure 5.5) The bi-directional sedimentary process has resulted in the development of the dominant sediment features in the Northern Andaman Sea recorded in the geophysical surveys, the well stratified, homogenous mud drape along the western coast of Myanmar and extending to the shelf edge, and the 60 m thick distal depocenter within the Martaban Depression.

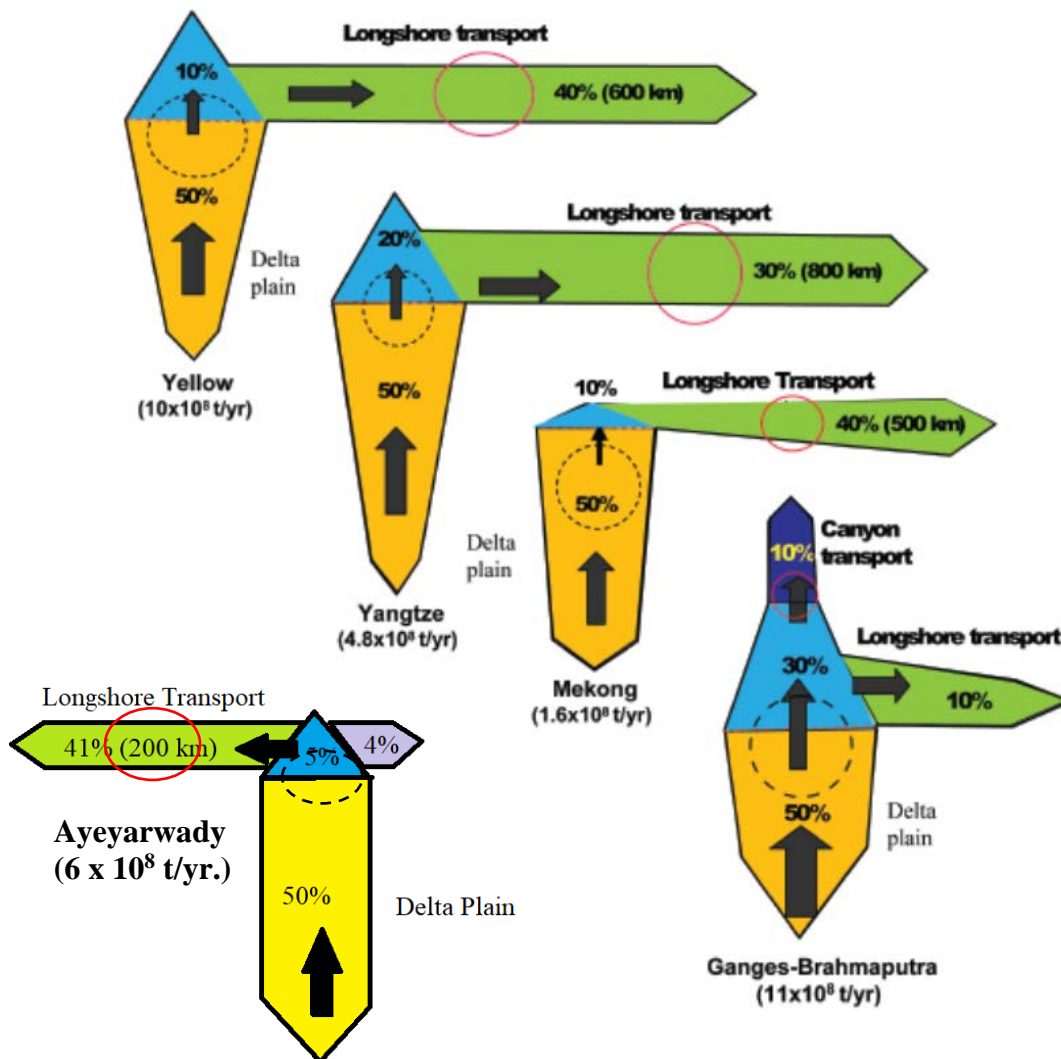


Figure 5.5. Conceptual model of the fate of Ayeyarwady derived river sediment to the Northern Andaman Sea. The dash circles represent the proximal deponent near the river mouth, and the red circles represent the distal deponent. Modified from Liu et al., (2009).

5.2 A tale of two clinoforms

At the last glacial maximum (LGM), sea level was approximately 125 m lower than it is at present, exposing the inner shelf of the Andaman Sea. As the climate changed, the rapid rise in post-glacial sea level played a pivotal role in the evolution of the Ayeyarwady Delta and the subaqueous clinoform. Postglacial sea-level rise was discontinuous, it was step-like, where periods of slow transgression were alternated by periods of rapid flooding (Fairbanks et al.,

1989; Bard et al., 1990; Velozzi, 2004). Attempts to better constrain the timing and depth of meltwater pulses and flooding events in the western Pacific have been undertaken using proxies such as submerged coral reefs and mangrove peat deposits (Liu et al., 2004). However, sea-level change data for the Ayeyarwady Delta and the surrounding Andaman Sea are sparse and unreliable. In addition, there is no existing data on uplift or subsidence (Giosan et al., 2018).

Our seismic profiles document the TS thoroughly and show that it exists beneath the shore attached clinoform and the more extensive, distal clinoform deposits. In the distal clinoform, the depth of the TS is -70 m (Figure 4.11, Figure 4.12, Figure 4.17). This transgressive surface depth matches that of other TS found in the subaqueous deltas of the Yangtze and Yellow Rivers where the sea-level curve shows that there was a 15 m jump (95 -80) during Meltwater Pulse 1-A (MWP-1A) (14.3 – 14.1 ka BP) (Figure 5.6; Liu et al., 2004; Velozzi, 2004). Following MP-1A, sea level stagnated, and transgressive sediments accumulated, creating the TS. This suggests that the (-70 m) transgressive surface formed after the rapid sea-level rise of MWP-1A, between 14 -12 ka BP, and associated truncation of strata. The TS of the shore attached clinoform is much shallower, ~ 30 m (Figure 4.5, Figure 4.7). Combining the seismic profiles with the sea-level record indicates that the shallower TS likely formed between 11–9.5 ka BP, in response to a pause in the postglacial sea-level rise after MWP-1B (Figure 5.6; Liu et al., 2004). From 9.5–9.2 ka BP, sea level jumped again, from -32 to -10 m during MWP-1C, and then continued to rise to +3 m during the middle Holocene highstand ~ 7 ka BP (Velozzi, 2004). Since the Holocene highstand, sea level rise has decelerated and stabilized (Liu et al., 2004). Based on this interpretation, the inner mid-shelf of the Northern Andaman Sea has experienced at least two major rapid sea-level rise events.

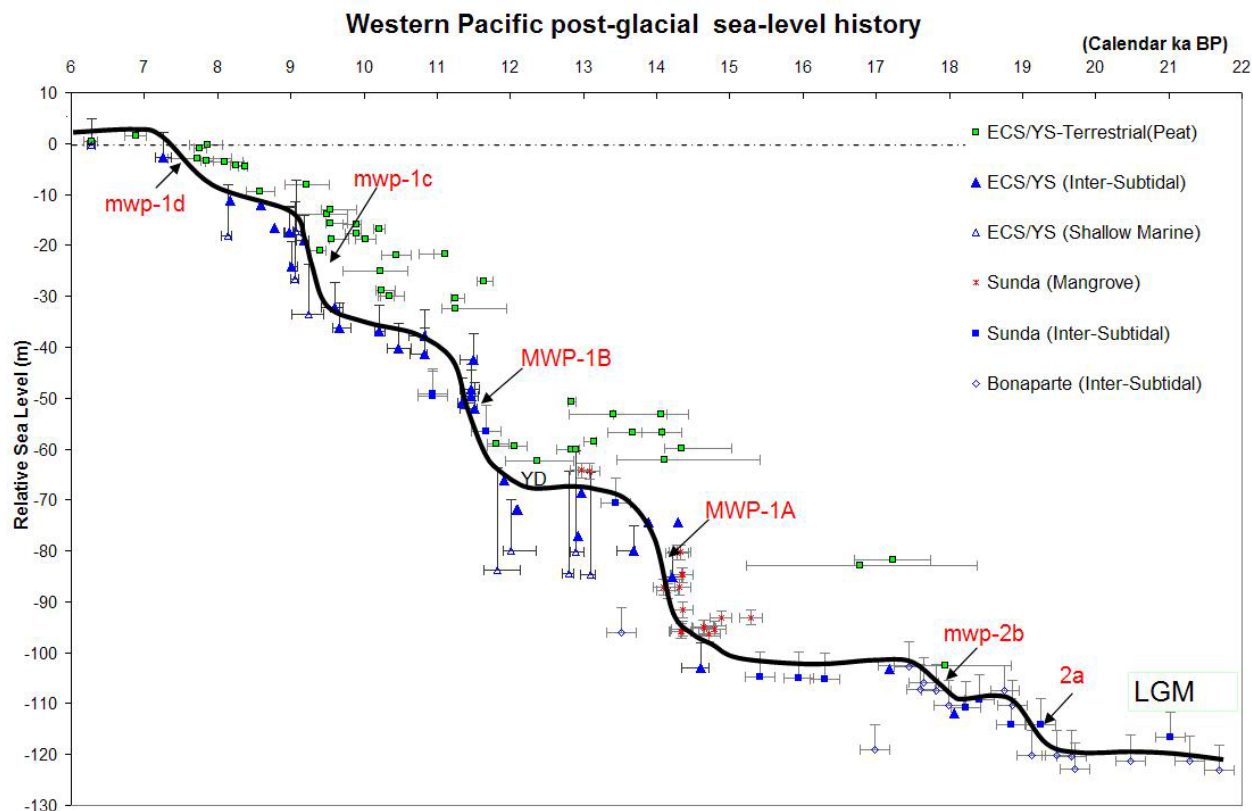


Figure 5.6. Western Pacific post-glacial sea-level curve (Liu et al., (2005).

In some profiles where the TS is deeper (-70 m), it appears that it blends into the MFS (Figure 4.12, Figure 4.17). At this depth, one would typically find a TST separating the TS and the MFS (Chen et al., 1986; Velozzi, 2004). The lack of the TST would suggest that either the TST was truncated, or the mid-shelf off the Ayeyarwady was sediment starved and the depocenter might not have reached to 15° N latitude before the middle Holocene highstand. The topset–foreset rollover point of the compound clinoform occurs at the ~ 30 m water depth (Figure 4.17), which seems to be consistent with similar compound clinoforms found in the Gulf of Papua and the Eastern China Sea (Walsh et al., 2004; Liu et al., 2004).

Reflectivity in the acoustic impedance of the highstand system tracts in the shore attached clinoform varies significantly (Figure 4.5). The acoustically transparent, rapidly prograding T1& T2 highstand beds are composed of fine silt and clay, with a small fraction of sand and coarse silt

(KC-10), compared to the dominantly sand and coarse-grained silt, acoustically opaque, highstand bed of T3 (KC-12; Kuehl et al., 2019). Other Kasten cores collected in the foreset (KC-13, KC-14; Figure 4.7) indicate that sediment texture throughout the 10 m thick foreset off the mouths of the Ayeyarwady is dominantly sand and coarse silt (Kuehl et al., 2019). The exact dating of these sediments is unavailable; however, the finer-grained beds (T1&T2) likely accumulated as the subaerial delta was still prograding (Figure 5.7).

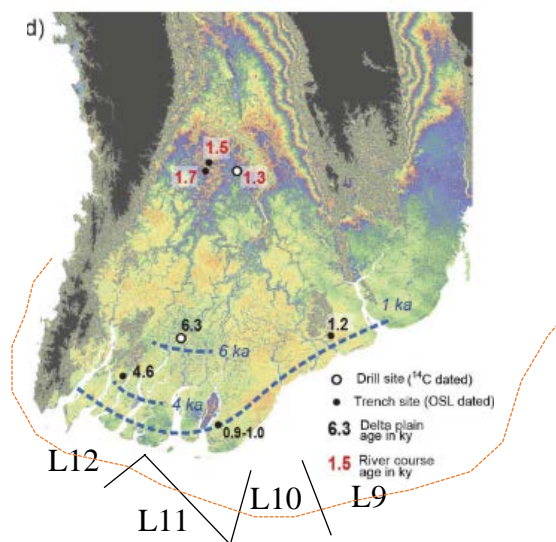


Figure 5.7. Historical progradation of the Ayeyarwady delta. Lines 9-12 = Figures 21-24 (Modified from Giosan et al., 2018).

Radiocarbon dating of sediment cores retrieved in the subaerial delta by Giosan et al., (2018) reveal that at 6 ka BP, the mouths of the Ayeyarwady would be sufficiently far enough away for finer-grained sediment to accumulate at the current location of the clinoform (Figure 4.5). As the delta reaches its present location, marine processes restrict finer-grained sediment from accumulating, thus appears the coarser-grained T3 layers overlaying the finer-grained T1 & T2 layers. Strong tidal currents and the seasonally reversing monsoon currents transport the finer-grained sediment away from the mouths, into the distal depocenter in the Martaban Depression (Figure 4.11, Figure 4.12, Figure 4.17; Liu et al., 2020).

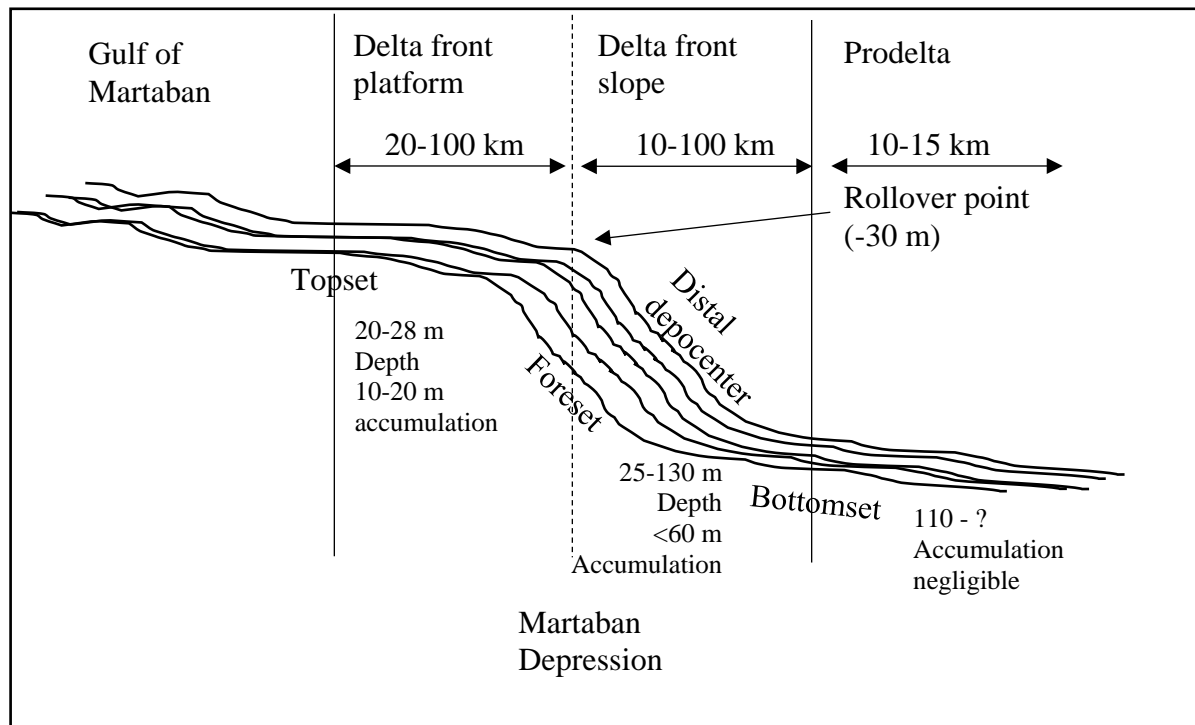


Figure 5.8. Cartoon of the Ayeyarwady Subaqueous delta.

Recent studies have suggested that due to the delta's current coastline position, shoaling, wave resuspension, and seasonally reversing currents are major actors in displacing sediment away from the mouths (Kuehl et al., 2019; Liu et al., 2020). However, it is also possible that uplift near the mouths has reduced accommodation space, resulting in sediment bypassing and restricting accumulation to thin, parallel layers (T3) of coarse sand (T1&T2; Figure 4.5, Figure 4.6, Figure 4.7). Similarly, increased accommodation space in the Martaban Depression has resulted due to subsidence from active extensional systems splaying off the termination of a major strike-slip fault. The Holocene sediment displaced from the mouths of the Ayeyarwady due to the seasonally reversing monsoon currents and persistently strong tidal currents accumulate in the distal depocenter, within the bathymetric low of the Martaban depression (Figure 5.11).

5.3 Delta shift and possible tectonic influence

Long term uplift and subsidence rates of the Ayeyarwady Delta since the middle Holocene are unknown. The only continuous GPS network in the region comprises eight stations that form two transects across the Sagaing Fault, a right-lateral strike-slip fault east of the delta (Sone Aung et al., 2016). The only documented uplift rate available in the literature is of the Shillong Plateau, due north roughly ~600 km of the southern Indo-Burman range, yielding a surface uplift rate of 0.4-0.53 mm a⁻¹ (Biswas et al., 2007). Rather, the majority of research concentrates on co-seismic uplift from single earthquake events (Carter et al., 2017a). For example, after December 26, 2004 earthquake that nucleated off northern Sumatra, GPS instruments recorded an uplift of 63 cm in the Northern Andaman Islands, and 1.1 m of subsidence at Port Blair (Carter et al., 2017a). As a consequence of viscoelastic relaxation of co-seismic stress and slip on the plate interface, Port Blair slowly rose and recovered 24% of co-seismic subsidence by 2007. This lack of reliable vertical offset rates, from either single or long-term events, makes it difficult to determine whether a consistent pattern of uplift and subsidence exists in the back-arc basin complex, or whether the large magnitude earthquakes contribute to local deformation of the delta.

As reported by Raju et al., 2005, during the phases of extension and rifting from the middle Miocene to early Pliocene, the area was subject to rapid sediment influx from mountain building in the North, as well as arc volcanism east of the A-N ridge. Over this short time frame, the intrusion of magma into the shallow crust east of the A-N ridge promoted uplift, while rapid sedimentation in the eastern back-arc basin resulted in subsidence (Figure 5.9).

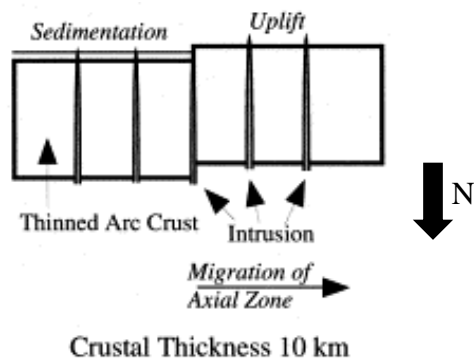


Figure 5.9. Example of Arc Volcanism in the Northern Andaman Sea (Fujiwara et al., 2001).

As the Andaman Spreading Center (ASC) separated the Alcock and Sewell rise complexes during the late Miocene, the Burma Plate was dragged northward by the Sagaing Fault, while uplift of the forearc ensued due to the oblique subduction of the Indian Plate beneath the Eurasian Plate (Raju et al., 2005). Later, in the late Miocene and early Pliocene, the zone of stretching (extensional horsetails) migrated northwest and the creation of a linked system between the Sagaing, West Andaman, and Sumatran Faults began (Srisuriyon et al., 2014). This link encouraged the fault systems to co-develop and maintain similar displacements, much like the Mergui and Manora fault systems do to the southeast of our study area (Srisuriyon et al., 2014). Research revealing the actual depth of the seafloor in the Andaman Sea during the Miocene is inconsistent and unreliable. However, literature published by Srisuriyon et al., (2014) has shown that the Mergui Basin, SE of the ASSC, contains middle Miocene shallow marine prograding clinoforms that are now under < 600 m of water. If we consider that the topsets of the clinoforms must have formed within 30 m water depth, then we can conclude that the Andaman Sea seafloor was relatively shallow before the opening of the Andaman spreading center. At present, the depth of the Andaman Sea Spreading center is approximately 5,000 m. If we assume that extension began at the depth of the seafloor, and the seafloor gradually deepened as

extension persisted, then a subsidence rate of $\sim 1 \text{ m ka}^{-1}$ is required to generate the observed bathymetry of the ASC.

Earthquake hypocenters nucleating at depths of 12-15 km indicated that right lateral, oblique dip-slip faults are concentrated in the Martaban Depression. These faults appear to be good candidates for extensional horsetail structures near the termination of an eastern segment of the strike-slip Sagaing Fault (Figure 5.10; Rangin et al., 1999). These extensional structures are considered to be responsible for the majority of subsidence in the depression and are still highly active, rupturing as recently as 2009. While the normal faults (Figure 4.5, Figure 4.12, Figure 4.18) are the product of back-arc tectonics, they also indicate that the depression is still actively subsiding, based on several meter-thick Holocene sediments accumulating on top of the bookshelf faults. These faults cut through the strata to the surface near the 90 m water depth and display an average vertical offset of 9 m. If it is assumed that roughly 80% of the slip from the normal faults result in subsidence, then the remaining 20% would result in localized uplift (Gallen et al., 2014). Relative dating based upon the earliest transgressive surface through which the faults cut compared to the sea-level curve for the Eastern China Sea (ECS) indicates that they have been active since at least 9 ka. The vertical offset of the faults average $\sim 9 \text{ m}$, which provides a rough slip rate of $\sim 1 \text{ mm a}^{-1}$, similar to the rate of subsidence in the ASC.

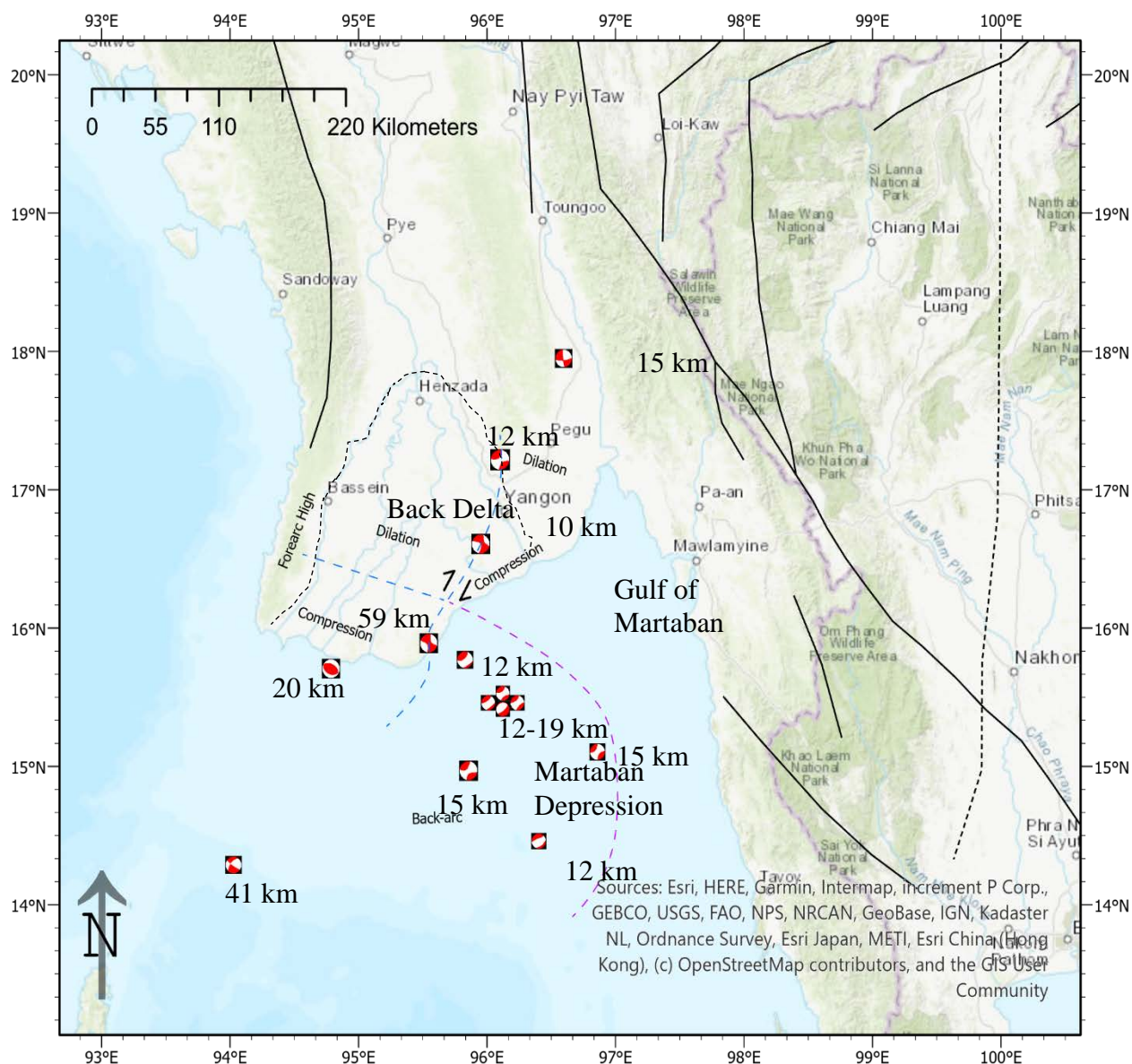


Figure 5.10. Location and focal mechanism of significant earthquakes ($M_w > 5$) near Myanmar since 1976. Earthquake data from Dziewonski et al., 1981; Ekström et al., 2012. The black dashed line outlines the Ayeyarwady delta. The blue dashed line represents the conceptual boundary between dilation and compression due to focal mechanisms.

The location of the tectonic depression (between 30 m–130 m water depth) immediately offshore from the subaerial portion of the delta, between the 14–16° N latitude, has resulted in the distal depocenter being a highly efficient sediment trap (Figure 5.11). Uplift along the mouths of the delta is likely caused by two major components. Since the Andaman Sea is a back-

arc basin and there is an active highly oblique subduction zone located adjacent to the delta, it is natural that there would be uplift in the forearc and subsidence in the backarc; however, a component of the total uplift is likely derived from a large thrust fault located directly off the mouths of the Ayeyarwady (Figure 5.10). The orientation of the thrust fault indicates that compression/uplift is occurring, but the lack of continuous GPS points in this area makes it impossible to estimate the importance of this thrust fault on the long-term uplift of the delta.

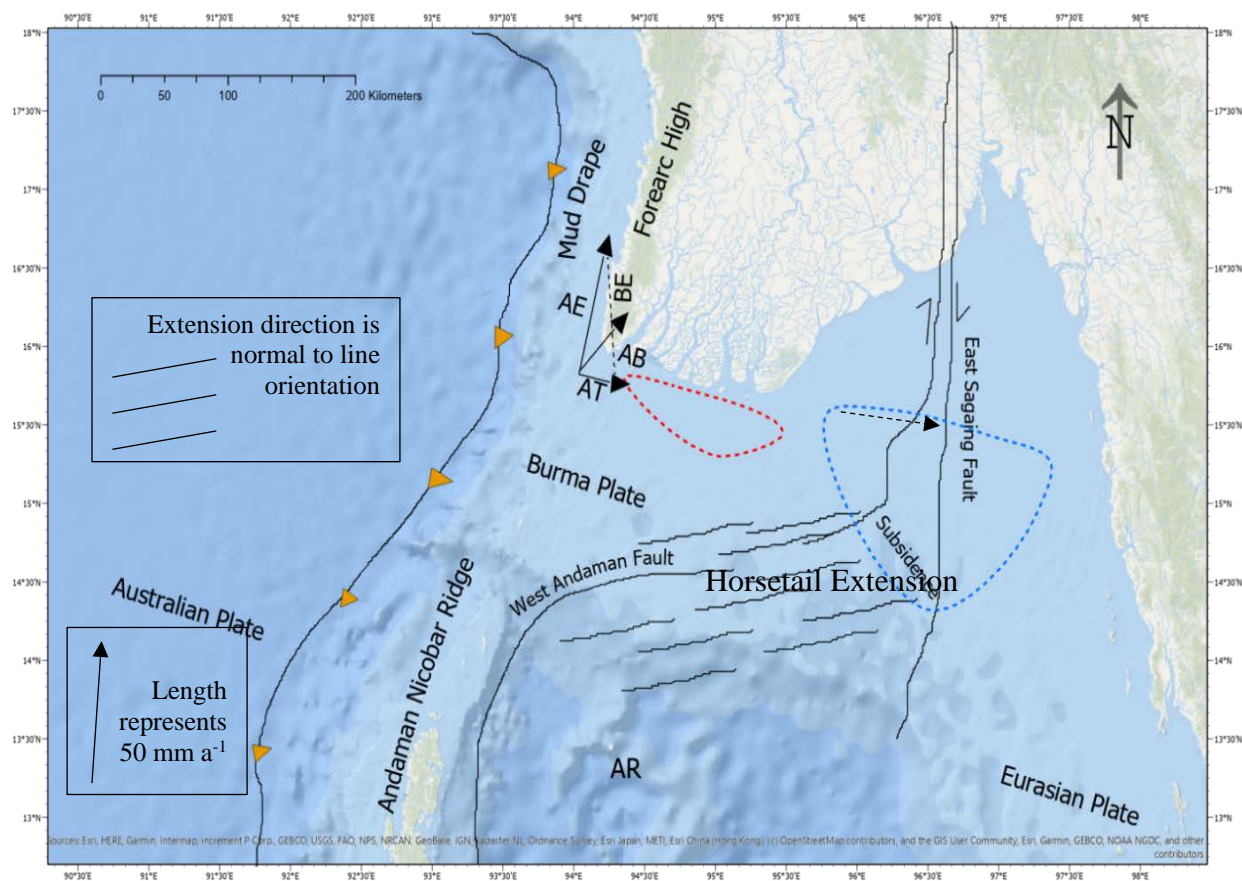


Figure 5.11. Geological features of the Andaman Sea. Abbreviations: AE: Australian-Eurasian motion; AB: Australian-Burma motion; AT: Australian-Trench motion (convergence across subduction zone); BE: Burma-Eurasian Motion; AR: Alcock Rise. The red dotted circle represents the area of reduced accommodation space. The blue dotted circle represents an area of increased accommodation space (Based on Srisuriyon et al., 2014; Morley et al., 2016).

Modern deltas developed as a response to the middle Holocene deceleration and stabilization of post-glacial sea-level rise. Since about 7,000 ybp, the Ayeyarwady Delta prograded nearly 260 km at a rate of 40 m a^{-1} to its current position. However, over the last two centuries, the delta has experienced a period of homeostasis (Hedley et al., 2010). Recent research published by Chen et al., 2020 utilizes landsat imagery and NDVI composites since 1974 to assess distributary channel evolution of the Ayeyarwady delta and coastline change. The study ultimately surmised that accretion along the eastern coastline is occurring, while erosion along the Pyamalaw distributary has resulted in western coastline retreat (Figure 5.13). This study supports the results from the InSAR deformation map and thus might suggest that the delta is approaching or has already exceeded its homeostatic period. Over the course of the delta's evolution, it is plausible that the Indo-Burman Range sheltered the Ayeyarwady Delta from incoming swells sourced in the Bay of Bengal, providing it with a sufficiently stable environment to build up and prograde seaward. Presently, the seaward progradation of the delta has halted because it has surpassed the protection of the forearc mountain range and is now subject to a suite of marine processes. This has subsequently resulted in the cannibalization of distributary channels between the Indo-Burman range and the Bogale Promontory. Incision of the distributary channels suggests that either the progradational deposits are poorly preserved due to the shallow water depth and incised channels, or uplift is occurring at a faster rate than sea-level rise (Galloway et al., 2013). In contrast, distributaries east of the Bogale Promontory are reported to be slowly building seaward, and the coastline appears to be uplifting or aggrading by an average of 5 mm a^{-1} (Figure 5.12; Hedley et al., 2010).

When comparing the focal mechanism map (Figure 5.10) and the SAR annual deformation map (Figure 5.12), it is apparent that the two maps agree with one another. From the

SAR imagery, uplift along the mouths of the delta, and subsidence on the back end, seem to correlate with the focal mechanisms and how one would expect a delta to respond to compressive and extensional forces. A maximum uplift rate of 20 mm a^{-1} between (16.1° to 15.40° N) and subsidence of 66 mm a^{-1} seem to be well within the range of surface land level change observed on similar deltas, such as the Yellow River Delta. A recent study showed that the transition from rice farming to an aquaculture dominated coastline can induce the same rate of rapid subsidence as that of major cities. Since deltas are highly compressible landforms, over-extraction of water for farming practices in a delta can lead to severe implications for the stability of the delta. In fact, in the Yellow River Delta, it was found that 70 km^2 of the aquaculture and salt production facility subsided over 50 mm a^{-1} (Higgins et al., 2013). Since 2007, fish production in the Ayeyarwady Delta has increased by over 250%, while the pond area under management double (Aquaculture, 2020).

The Ayeyarwady Delta is significantly more tectonically complex than the Yellow River Delta; therefore, subsidence rates resulting from the aquaculture component are likely exacerbated in such a highly active tectonic system. Dilation, from the oblique dip-slip fault NW of Yangon to the NE moving Sagaing Fault, stretches the delta between 16.1° to 16.4° resulting in near delta-wide subsidence, with the exception of the coastline (Figure 5.12). The net result of the extension is the lowering of mean elevation. A thrust fault situated just NW of the Ayeyarwady distributary, results in compression of the delta front, subsequently uplifting the region around the Bogale Promontory an average of $5\text{-}7 \text{ mm a}^{-1}$. Interestingly, the Pyamalaw distributary, between 15.5° and 16.1° N is not uplifting with the other distributary mouths; instead, it is subsiding. It is plausible that this displacement map represents a snapshot in time

where there has been a shift eastward of the dominant distributary channels and that sediment discharge from the Pyamalaw distributary has been dramatically reduced.

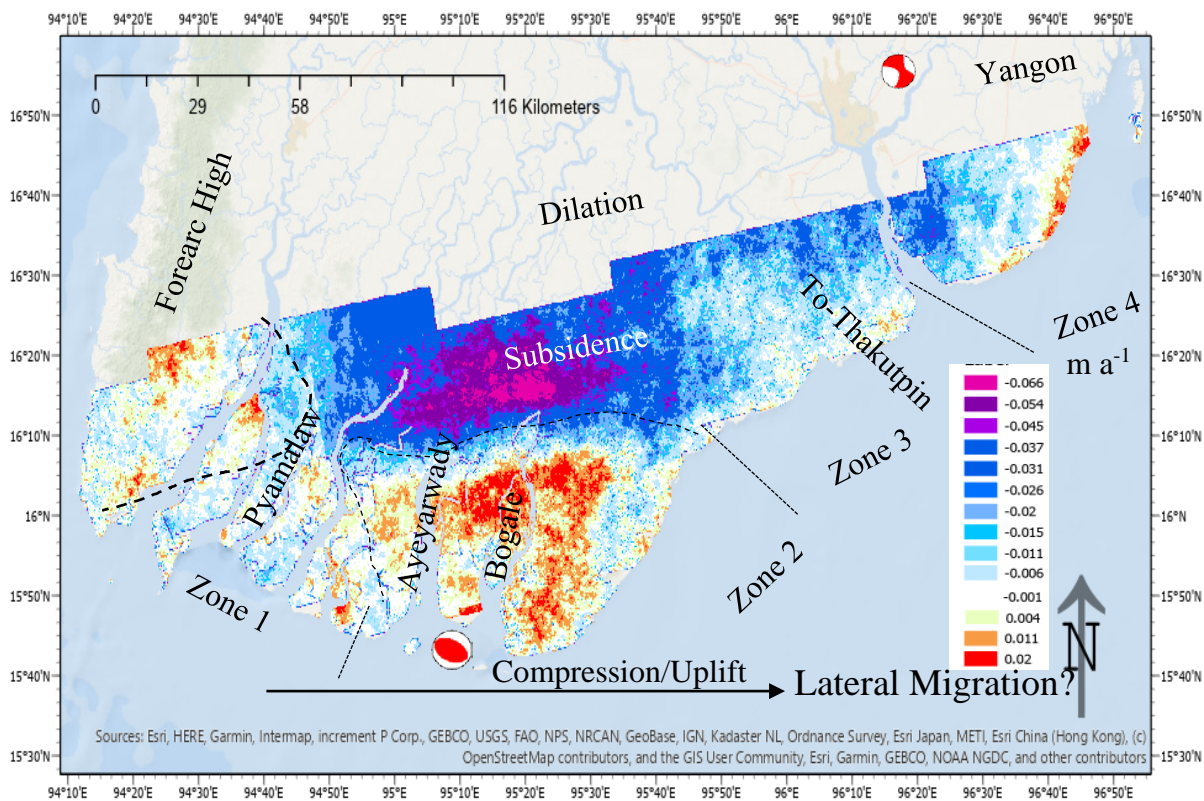


Figure 5.12. SAR Deformation Map (Jan. 2016 – 2020). The warm colors represent uplift and the cool colors represent subsidence. Data was reclassified with a moving kriging window to identify patterns better. Symbols:  Thrust fault; rupture 1980 (15.72N, 94.76E);  Oblique dip slip; rupture 1978 (16.64N, 95.94E); Black dashed lines represent the boundary of compression.

In tide-dominated deltas, sediment grain size often contribute directly to aggradation and the lateral migration and avulsion of river channels (Kuehl et al., 2011). In the instance that the lateral migration of the distributaries is faster than delta progradation, then the delta front facies will be replaced by distributary channel fill (Goodbred et al., 2011). The western section of the Ayeyarwady Delta has not prograded over the last two centuries, in fact recently published literature suggests that the western coastline of the delta is eroding, while the coastline east of the

Bogale Promontory, Zone 3 and 4, is accreting (Figure 5.12; Hedley et al., 2010; Chen et al., 2020).

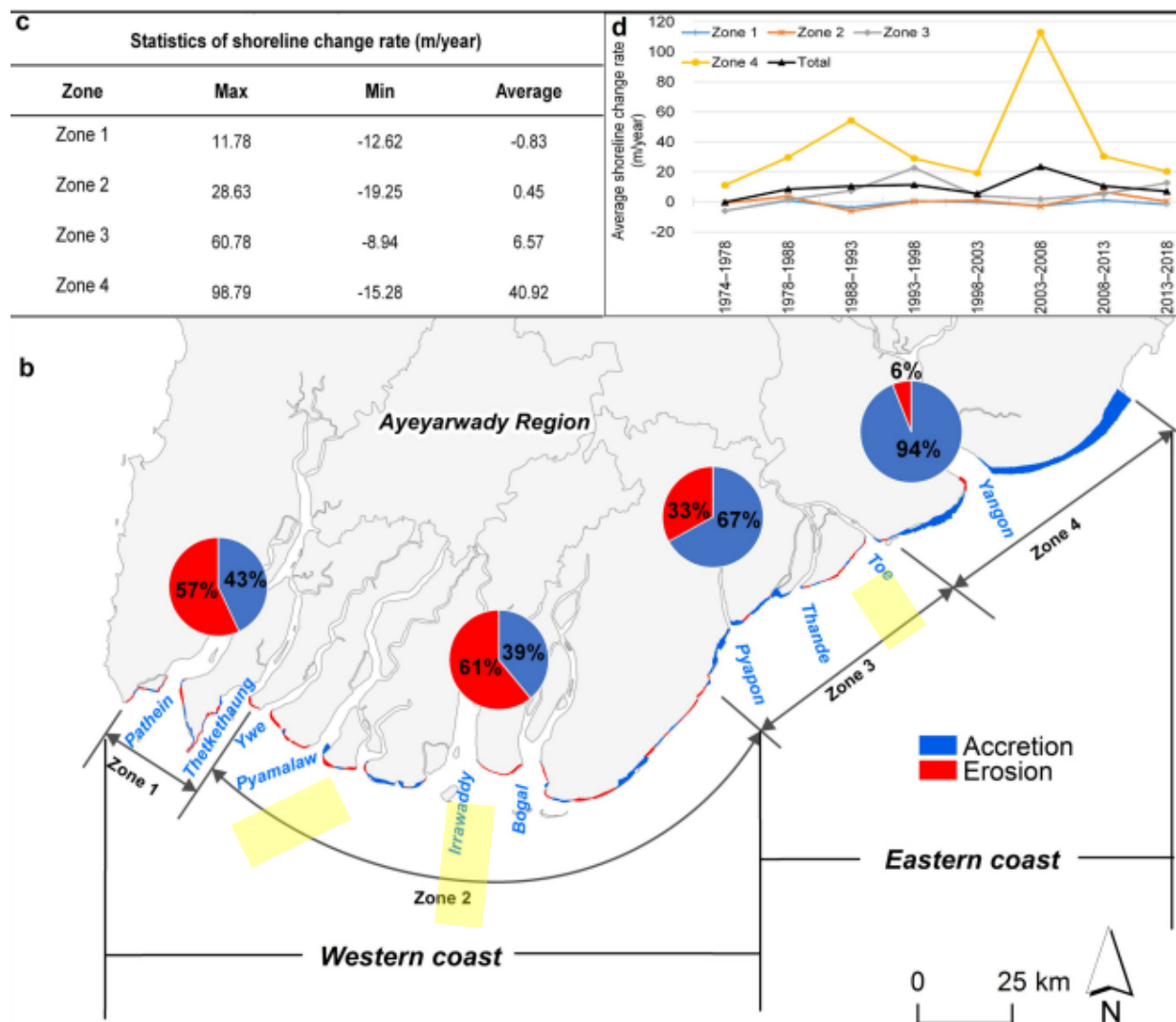


Figure 5.13. Shoreline change 1974-2018. (B) Accretion and Erosion map of the Ayeyarwady delta (C) Statistics of shoreline change per year. (D) Average shoreline change per year (1974-2018). Highlighted are the three primary distributaries that are responsible for discharging > 70% of freshwater and sediment from the Delta to the Andaman Sea (Chen et al., 2020).

Uplift of the delta and coastline accretion appears to be concentrated east of the Irrawaddy distributary while subsidence and erosion is dominantly west of the Irrawaddy distributary (Figure 5.12, Figure 5.13). Therefore, in addition to the gradual uplift of the delta, I

posit that the delta is in a period of lateral migration. The new dataset gathered by Chen et al., 2020 is in close agreement with the InSAR deformation map put forth in this thesis (Figures 5.12 – 5.13). The main distributary mouths have shifted, as indicated by the subsidence around the Pyamalaw channel, aggradation surrounding the Ayeyarwady channel, and the outward growth east of the To-Thakutpin channel and Yangon River. Further, there is a distinct difference in topography between the western and eastern coasts. Significant channel incision in the western coast signals that sedimentation cannot keep pace with sea-level rise; conversely, the eastern coast is void of incising channels, and instead exhibits outward growth of the delta front. Of course, to confirm this would require additional research in each of the nine distributaries regarding freshwater and sediment flux, as well as more reliable continuous GPS measurements to monitor vertical land surface deformation patterns. It is worth noting that the displacement rates reported in the InSAR deformation map also match well with the displacement rates reported by Horst et al. (2017) (Figure 5.12).

5.4 Comparison to Major World River Deltas

In Southeast Asian river systems, the majority of freshwater and sediment discharge occurs during the summer monsoon, but the sediments are only deposited temporarily. The majority of East Asian river systems exhibit uni-directional alongshore transport, where 30-40% of sediment yield accumulates in the distal depocenter about 300-400 km away from the river mouth, and 10% accumulates near the mouths, in a proximal depocenter (i.e., Yellow, Pearl, Mekong, and Yangtze). The remaining 50% of the sediment yield accumulates in the lower delta plain.

In the Bay of Bengal, the Ganges-Brahmaputra (G-B) Delta reflects many of the same geological features as the Ayeyarwady Delta including increased sediment discharge during the

summer monsoon, a confined bay area that acts as a highly efficient sediment trap, and a large offshore canyon (Liu et al., 2020). The difference, though, is that unlike the Ganges-Brahmaputra, Ayeyarwady derived sediment does not accumulate in its own offshore canyon. It is still possible that the Martaban canyon acts as a conduit for sediment to the deep sea; however, the results from the same High-Resolution CHIRP imagery that indicated sediment transport to the adjacent off-shore canyon from the G-B, suggest otherwise (Liu et al., 2020).

The high energy setting of the Gulf of Papua (GoP) resembles that of the Ayeyarwady. Active foreland basin tectonics, seasonal oceanographic currents, and massive sediment loads provide an ideal locale for clinoform growth and development. Similar to the Ayeyarwady, the GoP clinoform exhibits a well-defined topset, rapidly prograding foreset, and bottomset. Accommodation space plays a significant role in the net evolution of the clinoform and can be created or destroyed by changes in sea level and tectonic deformation (Wei et al., 2019). Subsidence in the north and peripheral uplift to the south of the GoP have influenced clinoform growth by encouraging more accommodation in the north and less in the south (Wei et al., 2019). By affecting the depth of the foundation surface, the tectonic processes greatly influence the depositional process of the Holocene clinoform, where shallower foundation surfaces become more exposed to shear stresses than the deeper foundation surfaces. Like the GoP, the depositional regime of the Ayeyarwady subaqueous delta is also affected by tectonic processes. Bulge uplift from the large thrust fault in the subaerial portion of the delta, and back-arc basin subsidence from horsetail extensional structures at the termination of the Eastern Sagaing fault has destroyed and created sediment accommodation space, respectively. Additionally, topsets in either river system experience significantly reduced accumulation rates than their respective foresets. Reduced accumulation in topset beds is likely due to less accommodation space and

increased exposure to wave energy, which causes larger bed shear stresses, resulting in SSC above the topsets being maintained and eventually depositing downslope, in the bathymetric low of the foreset (Wei et al., 2019).

Conclusions

1. Seasonal changes in tidal amplitude allow the turbid front to migrate, periodically releasing nearshore sediment to the foresets, where the turbid zone begins to lose energy (Figure 5.2). At this point, sediment cannot remain in suspension, resulting in higher accumulation rates after the sediment crosses the 40 m isobath (Figure 5.3). From the geophysical survey, no evidence was found to support the previous hypothesis by Ramaswamy et al., 2014 that the Martaban Canyon acts as a conduit for offshore sediment transport. Instead, the high-resolution seismic imagery collected as part of this research effort indicates that the Martaban Canyon head is devoid of any accumulation or progradation of modern sediment. Of course, since the entire canyon was not surveyed, it cannot be said for sure that accumulation is not occurring.
2. The two clinoforms recorded by the geophysical profiles in the 2017 survey indicate a change between proximal and distal depositional environments. The shore-attached clinoform appears to be relatively thin, composed of coarse sands and silts, and without any evidence of progradation (T3). In contrast, the seaward layers, T1 and T2, reveal steeply dipping foreset beds, and are composed of fine silts and clays. This difference in particle size and morphology suggests that during the time of deposition of the T1 & T2 layers, the clinoform was significantly further away from the river mouths, where only finer-grained sediments could be transported and deposited by the tidal and seasonally reversing monsoon currents. As the delta continued to prograde, the clinoforms proximity to the mouths increased. Shoaling and wave resuspension then displaced fine-grained sediments away from the mouths and toward the bathymetric low of the depression, leaving behind the coarse-grained sands and silts to accumulate as the T3 layer of the shore-attached clinoform (Figure 4.5). Similarly, these marine processes provide ample

energy to maintain suspension of fine-grained sediment as it is displaced to the east and accumulates on the rapidly prograding clinoform in the depression as part of the distal depocenter. In response to compression of the Burma micro plate and uplift along the forearc, the Martaban Depression is actively subsiding. This creates additional accommodation space in an area where sediment is already transported towards the bathymetric low (Figure 4.17, Figure 5.11). Thus, the depression acts as a highly efficient trap, responsible for accumulating the majority of the 83% total sediment flux from the Ayeyarwady Delta to the Northern Andaman Sea (Figure 5.5; Liu et al., 2020).

3. The seaward extent of the Indo-Burman Range has allowed for the Ayeyarwady Delta to rapidly prograde since the middle Holocene. Upon surpassing the protection of the mountain range from the incoming swell originating in the Bay of Bengal, progradation of the delta paused, resulting in a brief period of homeostasis. This period of deltaic equilibrium was first reported by Hedley et al., (2010), though a time-lapse of InSAR imagery suggest that eastwards lateral migration of the delta might be occurring (Figure 5.12; Figure 5.13). The relatively shallow thrust fault located directly off the distributary mouths suggests that there is a component of localized uplift in addition to uplift of the forearc resulting from the subduction margin (Figure 5.10). This assumption is further supported by satellite imagery that showcases cannibalization of the distributary mouths and across the InSAR deformation map that displays uplift rates of up to 2 cm a^{-1} nearest the Bogale Promontory (Figure 5.12). Highly oblique dip-slip faults in the upper crust, throughout the Martaban Depression, were first reported by Srisuryon et al., (2014) as extensional horsetail faults near the termination of a significant segment of the Sagaing fault. Their location and orientation of extension, as demonstrated in (Figure 5.10),

provides good evidence for active subsidence in the Martaban Depression, thus increasing accommodation space in the distal depocenter.

FUTURE STUDIES

Future studies in this region should include additional seismic surveys further offshore, in the Martaban Canyon, and across the Andaman Trench into the Bay of Bengal. Seismic surveys in this locale could further support the hypothesis proposed in this thesis and the paper by Liu et al., 2020 and Keuhl et al., 2019, that offshore sediment remains trapped in the Martaban Depression and does not accumulate on the banks or the floor of the Martaban Canyon at any capacity. Additionally, ADCP measurements taken in the Martaban Canyon could yield greater insight into sediment transport into/through the canyon and ultimately solve the debate as to whether sediment is transported through the canyon as a bottom current or alternatively if sediment is maintained in suspension in the upper water column. The short duration for the Bay of Bengal component of the study leaves open the need for additional studies that expand upon the preliminary data collected during the 2017 cruise. Questions remain as to how far Ayeyarwady derived river sediment extends out into the Bay of Bengal, and a follow-up cruise using similar techniques as the December 2017 cruise, could resolve these questions.

REFERENCES

- Alexander, C. R., Nittrouer, C. A., & DeMaster, D. J. (1986). High-resolution seismic stratigraphy and its sedimentological interpretation on the Amazon continental shelf. *Continental Shelf Research*, 6(1–2), 337–357. [https://doi.org/10.1016/0278-4343\(86\)90067-1](https://doi.org/10.1016/0278-4343(86)90067-1)
- Aquaculture is key for Myanmar. (2020, February 5). Retrieved from <https://thefishsite.com/articles/aquaculture-is-key-for-myanmar>
- Awasthi, N., Ray, J. S., Singh, A. K., Band, S. T., & Rai, V. K. (2014). Provenance of the Late Quaternary sediments in the Andaman Sea: Implications for monsoon variability and ocean circulation. *Geochemistry, Geophysics, Geosystems*, 15(10), 3890–3906. doi: 10.1002/2014gc005462
- Bard, E., Hamelin, B., Fairbanks, R.G., 1990. U–Th ages obtained by mass spectrometry in corals from Barbados: sea level during the past 130000 years. *Nature* 346 (6283), 456–458.
- Bertrand, G., & Rangin, C. (2003). Tectonics of the western margin of the Shan plateau (central Myanmar): implication for the India–Indochina oblique convergence since the Oligocene. *Journal of Asian Earth Sciences*, 21(10), 1139–1157. [https://doi.org/10.1016/S1367-9120\(02\)00183-9](https://doi.org/10.1016/S1367-9120(02)00183-9)
- Besset, M., Anthony, E. J., Dussouillez, P., & Goichot, M. (2017). The impact of Cyclone Nargis on the Ayeyarwady (Irrawaddy) River delta shoreline and nearshore zone (Myanmar): Towards degraded delta resilience? *Comptes Rendus - Geoscience*, 349(6–7), 238–247. <https://doi.org/10.1016/j.crte.2017.09.002>
- Bird, M., Robinson, R., Win Oo, N., Aye, M. M., Lu, X. X., Higgitt, D., ... Hoey, T. (2008). A preliminary estimate of organic carbon transport by the Ayeyarwady (Irrawaddy) and Thanlwin (Salween) Rivers of Myanmar. *Quaternary International*, 186. <https://doi.org/10.1016/j.quaint.2007.08.003>
- Brakenridge, G. R., Syvitski, J. P. M., Niebuhr, E., Overeem, I., Higgins, S. A., Kettner, A. J., & Prades, L. (2017). Design with nature: Causation and avoidance of catastrophic flooding, Myanmar. *Earth-Science Reviews*, 165, 81–109. <https://doi.org/10.1016/j.earscirev.2016.12.009>
- Carter, A., & Bandopadhyay, P. C. (2017). Chapter 14 Seismicity of the Andaman–Nicobar Islands and Andaman Sea. *Geological Society, London, Memoirs*, 47(1), 205–213. <https://doi.org/10.1144/m47.14>
- Chen, C. W., & Zebker, H. A. (2000). Network approaches to two-dimensional phase unwrapping: intractability and two new algorithms. *J. Opt. Soc. Am. A*, 17(3), 401–414. <https://doi.org/10.1364/JOSAA.17.000401>

- Chen, C. W., & Zebker, H. A. (2001). Two-dimensional phase unwrapping with use of statistical models for cost functions in nonlinear optimization. *J. Opt. Soc. Am. A*, 18(2), 338–351. <https://doi.org/10.1364/JOSAA.18.000338>
- Chen, C. W., & Zebker, H. A. (2002). Phase Unwrapping for Large SAR Interferograms: Statistical Segmentation and Generalized Network Models. *IEEE Transactions on Geoscience and Remote Sensing* 40(8): 1709-1719. *Geoscience and Remote Sensing, IEEE Transactions On*, 40, 1709–1719. <https://doi.org/10.1109/TGRS.2002.802453>
- Chen, D., Li, X., Saito, Y., Liu, P., Duan, Y., Liu, S. an, & Zhang, L. (2020). Recent evolution of the Irrawaddy (Ayeyarwady) Delta and the impacts of anthropogenic activities: A review and remote sensing survey. *Elsevier Geomorphology*.
- Cian, F., Blasco, J., & Carrera, L. (2019). Sentinel-1 for Monitoring Land Subsidence of Coastal Cities in Africa Using PSInSAR: A Methodology Based on the Integration of SNAP and StaMPS. *Geosciences*, 9(3), 124. <https://doi.org/10.3390/geosciences9030124>
- Curry, J., Emmel, F., Moore, D., & W. Raitt, R. (1982). Structure, Tectonics, and Geological History of the Northeastern Indian Ocean. In *The Ocean Basins and Margins* (Vol. 6). https://doi.org/10.1007/978-1-4615-8038-6_9
- Curry, J. (1989). The Sunda Arc: A model for oblique plate convergence. In *Netherlands Journal of Sea Research* (Vol. 24). [https://doi.org/10.1016/0077-7579\(89\)90144-0](https://doi.org/10.1016/0077-7579(89)90144-0)
- Curry, J. R. (1999). Abstract: A New Look at Present Tectonics and Opening History of the Andaman Sea . *AAPG Bulletin*, 83 (1999). doi:10.1306/e4fd4d2d-1732-11d7-8645000102c1865d
- Curry, J. R. (2005). Tectonics and history of the Andaman Sea region. *Journal of Asian Earth Sciences*, 25(1), 187-232. doi:10.1016/j.jseaes.2004.09.001
- Curry, J. (2015). Discussion: “Is spreading prolonged, episodic or incipient in the Andaman Sea? Evidence from deepwater sedimentation.” by C.K. Morley and A. Alvey (2015). In *Journal of Asian Earth Sciences* (Vol. 111). <https://doi.org/10.1016/j.jseaes.2015.08.006>
- Data Recipes. (n.d.). Retrieved from <https://www.asf.alaska.edu/asf-tutorials/data-recipes/>
- Davis, R. A., & Dalrymple, R. W. (2010). Principles of tidal sedimentology. *Principles of Tidal Sedimentology*, (May 2014), 1–621. <https://doi.org/10.1007/978-94-007-0123-6>
- DeMaster, D. J., Liu, J. P., Eidam, E., Nittrouer, C. A., & Nguyen, T. T. (2017). Determining rates of sediment accumulation on the Mekong shelf: Timescales, steady-state assumptions, and radiochemical tracers. *Continental Shelf Research*, 147(December 2016), 182–196. <https://doi.org/10.1016/j.csr.2017.06.011>

- Diehl, T., Waldhauser, F., Cochran, J. R., Kamesh Raju, K. A., Seeber, L., Schaff, D., & Engdahl, E. R. (2013). Back-arc extension in the Andaman Sea: Tectonic and magmatic processes imaged by high-precision teleseismic double-difference earthquake relocation. *Journal of Geophysical Research: Solid Earth*, 118(5), 2206–2224. <https://doi.org/10.1002/jgrb.50192>
- Dziewonski, A. M., T.-A. Chou and J. H. Woodhouse, Determination of earthquake source parameters from waveform data for studies of global and regional seismicity, *J. Geophys. Res.*, 86, 2825-2852, 1981. doi:10.1029/JB086iB04p02825
- Ekström, G., M. Nettles, and A. M. Dziewonski, The global CMT project 2004-2010: Centroid-moment tensors for 13,017 earthquakes, *Phys. Earth Planet. Inter.*, 200-201, 1-9, 2012. doi:10.1016/j.pepi.2012.04.002
- Fairbanks, R.G., 1989, A 17,000-year glacio-eustatic sea level record: Influence of glacial melting rates on the Younger Dryas event and deep-ocean circulation: *Nature*, v. 342, p. 637–642.
- Ferretti A., Massonet D., Monti Guarnieri A., Prati C., Rocca F., 2007, *InSAR Principles: Guidelines for SAR Interferometry Processing and Interpretation*, ESA TM-19
- Fritz, H.M., Blount, C.D., Thwin, S., Thu, M.K., Chan, N., 2009. Cyclone Nargis storm surge in Myanmar. *Nat. Geosci.* 2, 448–449.
- Fujiwara, T., Yamazaki, T., & Joshima, M. (2001). Bathymetry and magnetic anomalies in the Havre Trough and southern Lau Basin: from rifting to spreading in back-arc basins. *Earth and Planetary Science Letters*, 185(3), 253–264. [https://doi.org/https://doi.org/10.1016/S0012-821X\(00\)00378-2](https://doi.org/https://doi.org/10.1016/S0012-821X(00)00378-2)
- Galloway, W. E., & Hobday, D. K. (2013). *Terrigenous Clastic Depositional Systems Applications to Fossil Fuel and Groundwater Resources*. Berlin: Springer Berlin.
- Garzanti, E., Wang, J. G., Vezzoli, G., & Limonta, M. (2016). Tracing provenance and sediment fluxes in the Irrawaddy River basin (Myanmar). *Chemical Geology*, 440, 73–90. <https://doi.org/10.1016/j.chemgeo.2016.06.010>
- Gebremichael, E., Sultan, M., Becker, R., el bastawesy, M., Cherif, O., & Emil, M. (2018). Assessing Land Deformation and Sea Encroachment in the Nile Delta: A Radar Interferometric and Inundation Modeling Approach. *Journal of Geophysical Research: Solid Earth*, 123, 3208–3224. <https://doi.org/10.1002/2017jb015084>
- Giosan, L., Naing, T., Tun, M. M., Clift, P. D., Filip, F., Constantinescu, S., ... Thwin, S. (2018). On the Holocene evolution of the Ayeyarwady megadelta. *Earth Surface Dynamics*, 6(2), 451–466. <https://doi.org/10.5194/esurf-6-451-2018>

- Goodbred, S., & Saito, Y. (2011). Tide-Dominated Deltas. In *Principles of Tidal Sedimentology* (pp. 129–149). https://doi.org/10.1007/978-94-007-0123-6_7
- Grill, G., Lehner, B., Thieme, M., Geenen, B., Tickner, D., Antonelli, F., ... Zarfl, C. (2019). Mapping the world's free-flowing rivers. *Nature*, 569(7755), 215–221. <https://doi.org/10.1038/s41586-019-1111-9>
- Hajj, M. E., Baghdadi, N., Bazzi, H., & Zribi, M. (2018). Penetration Analysis of SAR Signals in the C and L Bands for Wheat, Maize, and Grasslands. *Remote Sensing*, 11(1), 31. doi: 10.3390/rs11010031
- Hedley, P. J., Bird, M. I., & Robinson, R. A. J. (2010). Evolution of the Irrawaddy delta region since 1850. *Geographical Journal*, 176(2), 138–149. <https://doi.org/10.1111/j.1475-4959.2009.00346.x>
- Higgins, S., Overeem, I., Tanaka, A., & Syvitski, J. P. M. (2013). Land subsidence at aquaculture facilities in the Yellow River delta, China. *Geophysical Research Letters*, 40(15), 3898–3902. doi: 10.1002/grl.50758
- Higgins, S., Overeem, I., Steckler, M., Syvitski, J., Seeber, L., & Akhter, S. (2014). InSAR Measurements of Compaction and Subsidence in the Ganges-Brahmaputra Delta, Bangladesh. *Journal of Geophysical Research: Earth Surface*, 119. <https://doi.org/10.1002/2014JF003117>
- Kravtsova, V. I., Mikhailov, V. N., & Kidyayeva, V. M. (2009). Hydrological regime, morphological features and natural territorial complexes of the Irrawaddy River Delta (Myanmar). *Water Resources*, 36(3), 243–260. doi: 10.1134/s0097807809030014
- Kuehl, S. A., Nittrouer, C. A., & DeMaster, D. J. (1986). Distribution of sedimentary structures in the Amazon subaqueous delta. *Continental Shelf Research*, 6(1–2), 311–336. [https://doi.org/10.1016/0278-4343\(86\)90066-X](https://doi.org/10.1016/0278-4343(86)90066-X)
- Kuehl, S. A., Alexander, C. R., Blair, N. E., Harris, C. K., Marsaglia, K. M., Ogston, A. S., ... Walsh, J. P. (2016). A source-to-sink perspective of the Waipaoa River margin. *Earth-Science Reviews*, 153, 301–334. doi:10.1016/j.earscirev.2015.10.001
- Kuehl, S. A., Allison, M. A., Goodbred, S. L., & Kudrass, H. (2011). The Ganges–Brahmaputra Delta. *River Deltas-Concepts, Models, and Examples*, (January), 413–434. <https://doi.org/10.2110/pec.05.83.0413>
- Kuehl, S. A., Williams, J., Liu, J. P., Harris, C., Aung, D. W., Tarpley, D., Aye, Y. Y. (2019). Sediment dispersal and accumulation off the Ayeyarwady delta – Tectonic and oceanographic controls. *Marine Geology*, 417, 106000. doi: 10.1016/j.margeo.2019.106000

- Liu, J. P., & Milliman, J. D. (2004). Reconsidering melt-water pulses 1A and 1B: Global impacts of rapid sea-level rise. *Journal of Ocean University of China*, 3(2), 183–190. <https://doi.org/10.1007/s11802-004-0033-8>
- Liu, J. P., Milliman, J. D., Gao, S., & Cheng, P. (2004). Holocene development of the Yellow River's subaqueous delta, North Yellow Sea. *Marine Geology*, 209(1–4), 45–67. <https://doi.org/10.1016/J.MARGEO.2004.06.009>
- Liu, J., Xue, Z., Ross, K., Wang, H., Yang, Z., Li, A., & Gao, S. (2009). Fate of Sediments Delivered to the Sea by Asian Large Rivers: Long-Distance Transport and Formation of Remote Alongshore Clinothems. *The Sedimentary Record*, 7(4), 4-9. doi:10.2110/sedred.2009.4.4
- Liu, J. P., Kuehl, S. A., Pierce, A. C., Williams, J., Blair, N. E., Harris, C., ... Aye, Y. Y. (2020). Fate of Ayeyarwady and Thanlwin Rivers Sediments in the Andaman Sea and Bay of Bengal. *Marine Geology*, 423, 106137. <https://doi.org/10.1016/J.MARGEO.2020.106137>
- McCaffrey R. 1991. Slip vectors and stretching of the Sumatran fore arc. *Geology* 19:881–84
- McCaffrey, M. S., & Buhr, S. M. (2008). Clarifying Climate Confusion: Addressing Systemic Holes, Cognitive Gaps, and Misconceptions Through Climate Literacy. *Physical Geography*, 29(6), 512–528. <https://doi.org/10.2747/0272-3646.29.6.512>
- Mccaffrey, R. (2009). The Tectonic Framework of the Sumatran Subduction Zone. *Annual Review of Earth and Planetary Sciences*, 37(1), 345-366. doi:10.1146/annurev.earth.031208.100212
- Meade, R. H. 1996. River-sediment inputs to major del-tas. In Milliman, J., and Haq, B. U., eds. *Sea level rise and coastal subsidence*. Dordrecht, Kluwer Academic, p. 63–85.
- Middleton GV (1991) A short historical review of clastic tidal sedimentology. In: Smith DG, Reinson GE (eds) *clastic tidal sedimentology*, Can. Soc. Petrol. Geol. Memoir 16. Canadian Society of Petroleum Geologists, Calgary, pp ix–xv
- Mitchum, R.M., Vail, P.R. and Thompson, S. (1977) Seismic stratigraphy and global changes in sea level, part 2: the depositional sequence as the basic unit for stratigraphic analysis. In: *Seismic Stratigraphy: Applications to Hydrocarbon Exploration* (Ed. C.E. Payton), AAPG Mem., 26,53–62. Mutterlose,
- Moeremans, R. E., & Singh, S. C. (2015). Fore-arc basin deformation in the Andaman-Nicobar segment of the Sumatra-Andaman subduction zone: Insight from high-resolution seismic reflection data. *Tectonics*, 34(8), 1736–1750. <https://doi.org/10.1002/2015TC003901>
- Moore, G. F., Curray, J. R., & Emmel, F. J. (1982). Sedimentation in the Sunda Trench and forearc region. *Geological Society, London, Special Publications*, 10(1), 245–258. <https://doi.org/10.1144/gsl.sp.1982.010.01.16>

- Morley, C. K. (2016). Cenozoic structural evolution of the Andaman Sea: Evolution from an extensional to a sheared margin. *Geological Society Special Publication*, 431(1), 39–61. <https://doi.org/10.1144/SP431.1>
- Morley, Christopher. (2017). Chapter 4 Cenozoic rifting, passive margin development and strike-slip faulting in the Andaman Sea: a discussion of established v. new tectonic models. *Geological Society, London, Memoirs*. 47. 27-50. 10.1144/M47.4.
- Morley, C. K. (2017). Syn-kinematic sedimentation at a releasing splay in the northern Minwun Ranges, Sagaing Fault zone, Myanmar: significance for fault timing and displacement. *Basin Research*, 29, 684–700. <https://doi.org/10.1111/bre.12201>
- Natawidjaja, D. H., & Triyoso, W. (2007). The Sumatran Fault Zone — From Source To Hazard. *Journal of Earthquake and Tsunami*, 01(01), 21-47. doi:10.1142/s1793431107000031
- Natawidjaja, D. H. (2018). Updating active fault maps and slip rates along the Sumatran Fault Zone, Indonesia. *IOP Conference Series: Earth and Environmental Science*, 118(1), 0–11. <https://doi.org/10.1088/1755-1315/118/1/012001>
- Panchang, R. (2008). relict faunal testimony for sea-level fluctuations off Myanmar (Burma). *Journal of Paleontological Society of India*, 53(2), 185–195.
- Patruno, Stefano, Gary J. Hampson, C. A.-L. J. (2015). Quantitative characterization of deltaic and subaqueous clinofolds. *Earth Science Reviews*, 142, 79–119.
- Patruno, S., Hampson, G. J., Jackson, C. A. L., & Dreyer, T. (2015). Clinofold geometry, geomorphology, facies character and stratigraphic architecture of a sand-rich subaqueous delta: Jurassic Sognefjord Formation, offshore Norway. *Sedimentology*, 62(1), 350–388. <https://doi.org/10.1111/sed.12153>
- Paul, J., Bürgmann, R., Gaur, V. K., Bilham, R., Larson, K. M., Ananda, M. B., ... Kumar, D. (2001). The motion and active deformation of India. *Geophysical Research Letters*, 28(4), 647–650. <https://doi.org/10.1029/2000GL011832>
- Raju, K. K., Ramprasad, T., Rao, P., Rao, B. R., & Varghese, J. (2004). New insights into the tectonic evolution of the Andaman basin, northeast Indian Ocean. *Earth and Planetary Science Letters*, 221(1-4), 145–162. doi: 10.1016/s0012-821x(04)00075-5
- Ramaswamy, V., Rao, P. S., Rao, K. H., Thwin, S., Rao, N. S., & Raiker, V. (2004). Tidal influence on suspended sediment distribution and dispersal in the northern Andaman Sea and Gulf of Martaban. *Marine Geology*, 208(1), 33–42. <https://doi.org/10.1016/j.margeo.2004.04.019>
- Ramaswamy, V., Gaye, B., Shirodkar, P. V., Rao, P. S., Chivas, A. R., Wheeler, D., & Thwin, S. (2008). Distribution and sources of organic carbon, nitrogen and their isotopic signatures in

- sediments from the Ayeyarwady (Irrawaddy) continental shelf, northern Andaman Sea. *Marine Chemistry*, 111(3–4), 137–150. <https://doi.org/10.1016/j.marchem.2008.04.006>
- Ramaswamy, V. and Rao, P. S.: The Myanmar continental shelf, in: *Continental Shelves of the World: Their Evolution During the Last Glacio-Eustatic Cycle*, edited by: Chiocci, F. L. and Chivas, A. R., Bath, UK, Geological Society of London, 231–240, 2014.
- Rangin, C., Win, M., San, L., Win, N., Mouret, C., Bertrand, G., the GIAC Scientific Party, 1999. Cenozoic pull-apart basins in central Myanmar: the trace of the path of India along the western margin of Sundaland. *Terra Abstracts* 4 (1), 59
- Rao, P., Ramaswamy, V., & Thwin, S. (2005). Sediment texture, distribution and transport on the Ayeyarwady continental shelf, Andaman Sea. *Marine Geology*, 216(4), 239-247. doi:10.1016/j.margeo.2005.02.016
- Robinson, R. A. J., Bird, M. I., Oo, N. W., Hoey, T. B., Aye, M. M., Higgitt, D. L., ... Win, S. L. (2007). The Irrawaddy River Sediment Flux to the Indian Ocean: The Original Nineteenth-Century Data Revisited. *The Journal of Geology*, 115(6), 629–640. <https://doi.org/10.1086/521607>
- Rodolfo, K. S. (1969); Bathymetry and Marine Geology of the Andaman Basin, and Tectonic Implications for Southeast Asia. *GSA Bulletin* ; 80 (7): 1203–1230. doi: [https://doi.org/10.1130/0016-7606\(1969\)80\[1203:BAMGOT\]2.0.CO;2](https://doi.org/10.1130/0016-7606(1969)80[1203:BAMGOT]2.0.CO;2)
- Rodolfo, K. S. (1975). The Irrawaddy Delta : Tertiary Setting and Modern Offshore Sedimentation. *Deltas: Models for Exploration*, (1950), 329–348. <https://doi.org/10.1111/j.1744-7348.1998.tb05192.x>
- Schmitt, R. J. P., Rubin, Z., & Kondolf, G. M. (2017). Losing ground - scenarios of land loss as consequence of shifting sediment budgets in the Mekong Delta. *Geomorphology*, 294(December 2016), 58–69. <https://doi.org/10.1016/j.geomorph.2017.04.029>
- Sloan, R. A., Elliott, J. R., Searle, M. P., & Morley, C. K. (2017). Chapter 2 Active tectonics of Myanmar and the Andaman Sea. Geological Society, London, *Memoirs*, 48(1), 19 LP – 52. Retrieved from <http://mem.lyellcollection.org/content/48/1/19.abstract>
- Sone Aung, P., Satirapod, C., & Andrei, C.-O. (2016). Sagaing Fault slip and deformation in Myanmar observed by continuous GPS measurements. *Geodesy and Geodynamics*, 7(1), 56–63. <https://doi.org/10.1016/J.GEOG.2016.03.007>
- Srisuriyon, K., & Morley, C. K. (2014). Pull-apart development at overlapping fault tips: Oblique rifting of a cenozoic continental margin, northern mergui basin, andaman sea. *Geosphere*, 10(1), 80–106. <https://doi.org/10.1130/GES00926.1>

- Stanley, D. J., & Warne, A. G. (1994). Worldwide initiation of Holocene marine deltas by deceleration of sea-level rise. *Science*, 265(5169), 228–231. <https://doi.org/10.1126/science.265.5169.228>
- Stanley D J and Warne A G 1997 Holocene sea-level change and early human utilization of deltas *GSA Today* 7 1–7
- Syvitski, J. P. M., Kettner, A. J., Overeem, I., Hutton, E. W. H., Hannon, M. T., Brakenridge, G. R., ... Nicholls, R. J. (2009). Sinking deltas due to human activities. *Nature Geoscience*, 2(10), 681–686. <https://doi.org/10.1038/ngeo629>
- User Guides - Sentinel-1 SAR - Acquisition Modes - Sentinel Online. (n.d.). Retrieved from <https://sentinel.esa.int/web/sentinel/user-guides/sentinel-1-sar/acquisition-modes>
- Van der Horst, T.: Sinking Yangon: Detection of subsidence caused by groundwater extraction using SAR interferometry and PSI time-series analysis for Sentinel-1 data, MS Thesis, Delft University of Technology and the National University of Singapore, uuid:8067b72d-94af-44b2-9cb8-5b6c14a8fcde, available at: <http://repository.tudelft.nl> (last access: 28 May 2018), 2017.
- Kravtsova, V. I., Mikhailov, V. N., & Kidyeva, V. M. (2009). Hydrological regime, morphological features and natural territorial complexes of the Irrawaddy River Delta (Myanmar). *Water Resources*, 36(3), 243–260. doi: 10.1134/s0097807809030014
- Van Wagoner, J.C., Mitchum, R. M. J. (2003). *Seismic Stratigraphy Interpretation Using Sequence Stratigraphy: Part 2: Key Definitions of Sequence Stratigraphy*. (Figure 4). <https://doi.org/10.1306/bf9ab166-0eb6-11d7-8643000102c1865d>
- Velozzi, D., Liu, P., Li, A., & Demaster, D. (2004). Sedimentary Features of the Yangtze Derived Mud Deposits in the Inner Shelf of the East China Sea. *AGU Fall Meeting Abstracts*.
- Walsh JP, Nittrouer CA (2004) Mangrove sedimentation in the Gulf of Papua, Papua New Guinea. *Mar Geol* 208:225–248
- Walsh JP, Nittrouer CA (2009) Understanding fine-grained river- sediment dispersal on continental margins. *Mar Geol* 263:34–45
- Wei, E. A., Driscoll, N. W., & Slingerland, R. L. (2019). Oceanographic currents, differential subsidence, and physiography control three-dimensional clinothem growth in the Gulf of Papua, Papua New Guinea. *Marine Geology*, 407, 164–180. <https://doi.org/10.1016/J.MARGE0.2018.10.012>
- Xue, Z., Paul Liu, J., DeMaster, D., Leithold, E. L., Wan, S., Ge, Q., ... Ta, T. K. O. (2014). Sedimentary processes on the Mekong subaqueous delta: Clay mineral and geochemical analysis. *Journal of Asian Earth Sciences*, 79, 520–528. <https://doi.org/10.1016/j.jseas.2012.07.012>

Zecchin, M., Baradello, L., Brancolini, G., Donda, F., Rizzetto, F., & Tosi, L. (2008). Sequence stratigraphy based on high-resolution seismic profiles in the late Pleistocene and Holocene deposits of the Venice area. *Marine Geology*, 253(3–4), 185–198.
<https://doi.org/10.1016/j.margeo.2008.05.010>

APPENDIX

Table 2 Kasten Core location and water depth

Core	Length (cm)	Water Depth (m)	Lat (D M.m)	Long (D M.m)
SP-KC 01	180	5	15 45.600'N	96 04.199'E
SP-KC 02	280	75	14 57.476'N	96 12.403'E
SP-KC 03	NR	-	-	-
SP-KC 04	300+	21	15 30.041'N	096 52.721'E
SP-KC 05	300+	15	16 09.918'N	97 22.420'E
SP-KC 06	300+	25	15 11.643'N	97 31.013'E
SP-KC 07	217	28	15 03.933'N	97 21.926'E
SP-KC 08	300+	?	15 01.508'N	96 18.651'E
SP-KC 09	300	125	14 52.495'N	96 15.864'E
SP-KC 10	300+	35	15 15.178'N	95 33.725'E
SP-KC 11	260	55	15 12.191'N	95 34.425'E
SP-KC 12	65	10	15 30.044'N	95 26.971'E
SP-KC 13	68	35	15 14.734'N	94 46.740'E
SP-KC 14	100	20	15 36.250'N	94 35.993'E
SP-KC 15	237	38	15 52.921'N	94 04.368'E
SP-KC 16	S	13	15 57.715'N	94 11.016'E
SP-KC 17	170	110	16 08.300'N	93 51.416'E
SP-KC 18	253	53	16 35.738'N	94 08.888'E
SP-KC 19	220	77	16 28.291'N	94 03.734'E
SP-KC 20	15	45	16 26.023'N	94 07.132'E
SP-KC 21	230	90	16 18.753'N	93 59.984'E
SP-KC 22	NR	-	-	-
SP-KC 23	90	50	15 01.288'N	94 22.287'E
SP-KC 24	300+	58	14 55.558'N	94 54.966'E
SP-KC 25	75	170	14 07.217'N	96 06.161'E
SP-KC 26	NR	-	-	-
SP-KC 27	246	20	15 23.779'N	96 02.303'E
SP-KC 28	?	17	15 39.475'N	96 27.790'E
SP-KC 29	300+	17	15 50.315'N	96 45.498'E
SP-KC 30	?	8	16 01.812'N	96 15.689'E

Table 3 Major earthquakes and their focal mechanisms in the Northern Andaman Sea since 1976

093078A

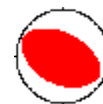
Date: 1978/ 9/30 Centroid Time: 9: 4:34.4 GMT
 Lat= 16.64 Lon= 95.94
 Depth= 10.0 Half duration= 2.9
 Centroid time minus hypocenter time: 3.2
 Moment Tensor: Expo=24 0.007 2.421 -2.427 0.997 -1.492 4.105
 Mw = 5.7 mb = 5.5 Ms = 5.7 Scalar Moment = 5.07e+24
 Fault plane: strike=17 dip=76 slip=-168
 Fault plane: strike=284 dip=78 slip=-14

**102478B ANDAMAN ISLANDS REGION**

Date: 1978/10/24 Centroid Time: 13:38:46.2 GMT
 Lat= 15.09 Lon= 96.86
 Depth= 15.0 Half duration= 1.9
 Centroid time minus hypocenter time: -2.1
 Moment Tensor: Expo=24 -0.312 -0.011 0.323 0.000 0.000 1.210
 Mw = 5.3 mb = 5.0 Ms = 5.1 Scalar Moment = 1.22e+24
 Fault plane: strike=176 dip=90 slip=180
 Fault plane: strike=266 dip=90 slip=0

**082780A SOUTH BURMA**

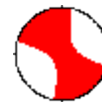
Date: 1980/ 8/27 Centroid Time: 4:30:20.9 GMT
 Lat= 15.72 Lon= 94.76
 Depth= 20.0 Half duration= 1.6
 Centroid time minus hypocenter time: 4.2
 Moment Tensor: Expo=23 7.723 -5.949 -1.774 -1.069 0.967 2.856
 Mw = 5.2 mb = 5.5 Ms = 4.8 Scalar Moment = 7.7e+23
 Fault plane: strike=114 dip=40 slip=86
 Fault plane: strike=299 dip=50 slip=93

**062986B SOUTH BURMA**

Date: 1986/ 6/29 Centroid Time: 9:55:41.4 GMT
 Lat= 15.45 Lon= 96.12
 Depth= 15.0 Half duration= 2.0
 Centroid time minus hypocenter time: 0.2
 Moment Tensor: Expo=24 -1.254 0.855 0.400 -1.425 -1.272 0.537
 Mw = 5.5 mb = 5.0 Ms = 5.1 Scalar Moment = 2.27e+24
 Fault plane: strike=242 dip=17 slip=-78
 Fault plane: strike=50 dip=74 slip=-94

**040191B SOUTH BURMA**

Date: 1991/ 4/ 1 Centroid Time: 3:53: 8.6 GMT
 Lat= 15.89 Lon= 95.53
 Depth= 58.7 Half duration= 3.7
 Centroid time minus hypocenter time: 4.1
 Moment Tensor: Expo=24 1.696 3.823 -5.519 0.570 -0.294 9.366
 Mw = 5.9 mb = 5.4 Ms = 6.1 Scalar Moment = 1.05e+25
 Fault plane: strike=13 dip=87 slip=-180
 Fault plane: strike=283 dip=90 slip=-3



061291B ANDAMAN ISLANDS REGION

Date: 1991/ 6/12 Centroid Time: 3: 5:25.4 GMT
 Lat= 14.96 Lon= 95.85
 Depth= 15.0 Half duration= 1.5
 Centroid time minus hypocenter time: 4.2
 Moment Tensor: Expo=23 -1.116 2.835 -1.719 -0.308 1.046 6.106
 Mw = 5.1 mb = 5.2 Ms = 5.2 Scalar Moment = 6.63e+23
 Fault plane: strike=99 dip=80 slip=-7
 Fault plane: strike=191 dip=84 slip=-170



081994C BURMA

Date: 1994/ 8/19 Centroid Time: 21: 2:48.1 GMT
 Lat= 17.96 Lon= 96.58
 Depth= 15.0 Half duration= 1.8
 Centroid time minus hypocenter time: 3.1
 Moment Tensor: Expo=24 -0.181 -0.893 1.074 -0.575 1.377 4.462
 Mw = 5.7 mb = 5.5 Ms = 5.6 Scalar Moment = 4.81e+24
 Fault plane: strike=83 dip=73 slip=-5
 Fault plane: strike=175 dip=85 slip=-163



091704C NEAR SOUTH COAST OF MYAN

Date: 2004/ 9/17 Centroid Time: 11:25:51.0 GMT
 Lat= 15.76 Lon= 95.83
 Depth= 12.0 Half duration= 1.7
 Centroid time minus hypocenter time: 2.8
 Moment Tensor: Expo=24 -1.420 1.730 -0.310 2.250 1.960 2.990
 Mw = 5.7 mb = 5.5 Ms = 5.8 Scalar Moment = 4.05e+24
 Fault plane: strike=95 dip=32 slip=-31
 Fault plane: strike=212 dip=74 slip=-118



200704260523A NEAR SOUTH COAST OF MYAN

Date: 2007/ 4/26 Centroid Time: 5:23:48.1 GMT
 Lat= 15.47 Lon= 96.16
 Depth= 12.0 Half duration= 0.7
 Centroid time minus hypocenter time: -1.0
 Moment Tensor: Expo=23 -1.240 1.020 0.220 0.485 -0.035 2.570
 Mw = 4.9 mb = 4.8 Ms = 0.0 Scalar Moment = 2.68e+23



Fault plane: strike=6 dip=72 slip=-167
 Fault plane: strike=272 dip=78 slip=-19

200708251703A ANDAMAN ISLANDS, INDIA R

Date: 2007/ 8/25 Centroid Time: 17: 3: 8.3 GMT
 Lat= 14.31 Lon= 94.01
 Depth= 41.1 Half duration= 1.0
 Centroid time minus hypocenter time: 0.5
 Moment Tensor: Expo=24 -0.148 0.805 -0.656 -0.308 0.349 0.211
 Mw = 5.2 mb = 5.1 Ms = 0.0 Scalar Moment = 9.01e+23
 Fault plane: strike=220 dip=59 slip=-170
 Fault plane: strike=124 dip=81 slip=-32



200809221330A NEAR SOUTH COAST OF MYAN

Date: 2008/ 9/22 Centroid Time: 13:30:37.5 GMT
 Lat= 15.46 Lon= 96.15
 Depth= 12.0 Half duration= 1.0
 Centroid time minus hypocenter time: -0.7
 Moment Tensor: Expo=24 -0.584 0.490 0.094 0.274 0.060 0.615
 Mw = 5.2 mb = 5.4 Ms = 4.9 Scalar Moment = 8.23e+23
 Fault plane: strike=33 dip=39 slip=-121
 Fault plane: strike=251 dip=57 slip=-67



200901210142A NEAR SOUTH COAST OF MYAN

Date: 2009/ 1/21 Centroid Time: 1:42:22.5 GMT
 Lat= 15.49 Lon= 96.11
 Depth= 19.3 Half duration= 0.7
 Centroid time minus hypocenter time: -2.1
 Moment Tensor: Expo=23 -1.100 1.980 -0.878 0.624 0.306 3.020
 Mw = 5.0 mb = 4.7 Ms = 0.0 Scalar Moment = 3.39e+23
 Fault plane: strike=12 dip=83 slip=176
 Fault plane: strike=103 dip=86 slip=7



200903051549A NEAR SOUTH COAST OF MYAN

Date: 2009/ 3/ 5 Centroid Time: 15:49:55.0 GMT
 Lat= 15.48 Lon= 96.09
 Depth= 12.0 Half duration= 0.8
 Centroid time minus hypocenter time: 2.2
 Moment Tensor: Expo=23 -2.940 2.600 0.345 2.060 1.060 3.730
 Mw = 5.1 mb = 5.2 Ms = 0.0 Scalar Moment = 4.8e+23
 Fault plane: strike=33 dip=34 slip=-120
 Fault plane: strike=247 dip=61 slip=-72



201703131419A MYANMAR

Date: 2017/ 3/13 Centroid Time: 14:19: 8.1 GMT
 Lat= 17.23 Lon= 96.09
 Depth= 12.0 Half duration= 1.0
 Centroid time minus hypocenter time: 1.4
 Moment Tensor: Expo=23 -1.080 2.300 -1.220 0.737 0.665 7.400
 Mw = 5.2 mb = 0.0 Ms = 5.1 Scalar Moment = 7.66e+23
 Fault plane: strike=97 dip=85 slip=4
 Fault plane: strike=7 dip=86 slip=175



201807042034A ANDAMAN ISLANDS, INDIA R

Date: 2018/ 7/ 4 Centroid Time: 20:34:53.8 GMT
 Lat= 14.47 Lon= 96.40
 Depth= 12.0 Half duration= 0.8
 Centroid time minus hypocenter time: 2.0
 Moment Tensor: Expo=23 -3.700 3.090 0.612 2.390 0.325 2.480
 Mw = 5.1 mb = 0.0 Ms = 5.1 Scalar Moment = 4.84e+23
 Fault plane: strike=42 dip=33 slip=-116
 Fault plane: strike=252 dip=61 slip=-74

